OCS Study
MMS 2001-093

Velocity and Transport Characteristics of the Louisiana-Texas Coastal Current during 1994

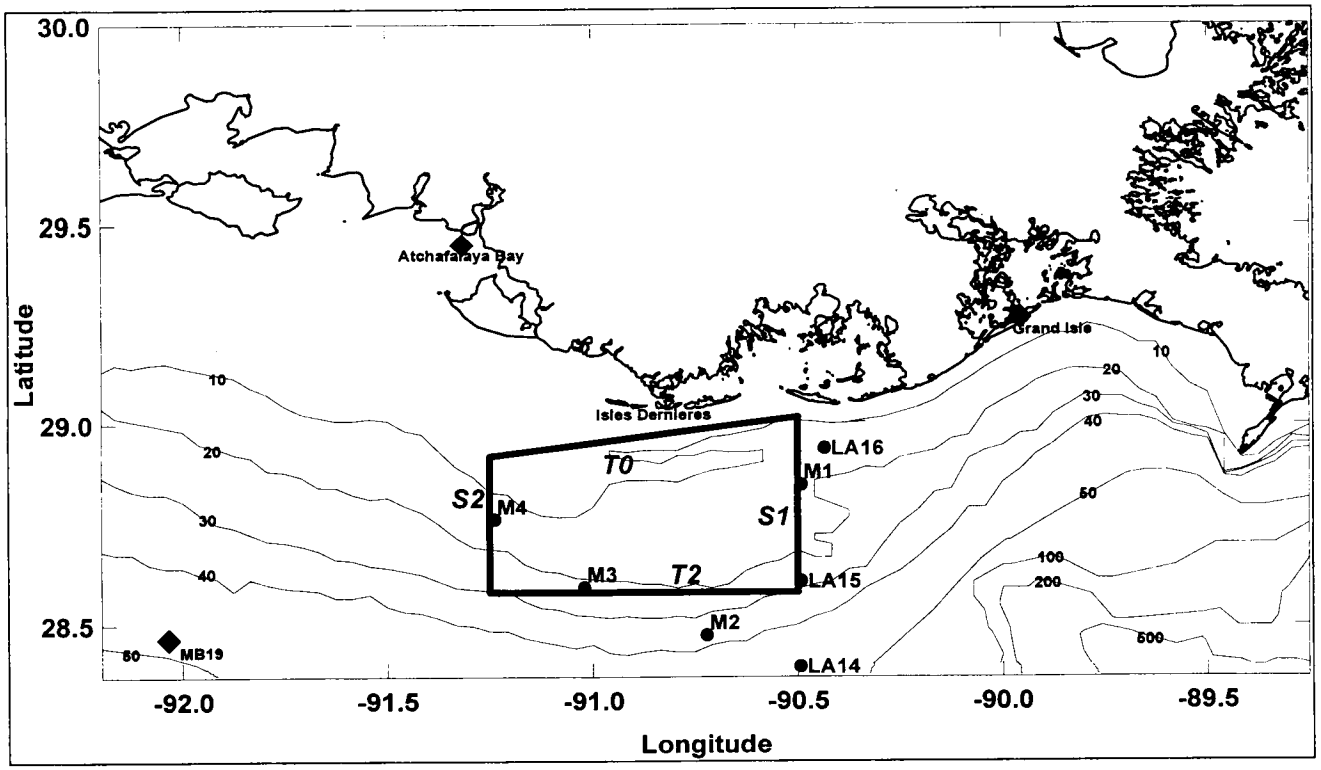

MMS U.S. Department of the Interior
Minerals Management Service
Gulf of Mexico OCS Region

OCS Study
MMS 2001-093

Velocity and Transport Characteristics of the Louisiana-Texas Coastal Current during 1994

Authors

Stephen P. Murray
Ewa Jarosz
Edward T. Weeks III

Prepared under MMS Contract
14-35-001-30724
by
Coastal Studies Institute
Howe-Russell Geoscience Complex
Louisiana State University
Baton Rouge, Louisiana 70801

Published by

U.S. Department of the Interior
Minerals Management Service
Gulf of Mexico OCS Region

New Orleans
November 2001

DISCLAIMER

This report was prepared under contract between the Minerals Management Service (MMS) and Coastal Studies Institute, Louisiana State University. This report has been technically reviewed by the MMS and approved for publication. Approval does not signify that the contents necessarily reflect the views or policies of the Service, nor does mention of trade names or commercial products constitute endorsement or recommendation for use. It is, however, exempt from review and compliance with MMS editorial standards.

REPORT AVAILABILITY

Extra copies of this report may be obtained from the Public Information Office (MS 5034) at the following address:

U.S. Department of the Interior
Minerals Management Service
Gulf of Mexico OCS Region
Public Information Office (MS 5034)
1201 Elmwood Park Boulevard
New Orleans, Louisiana 70123-2394

Telephone Number: (504) 736-2519 or
1-800-200 GULF

CITATION

Suggested citation:

Murray, S.P., E. Jarosz and E.T. Weeks, III. 2001. Velocity and Transport Characteristics of the Louisiana-Texas Coastal Current during 1994. OCS Study MMS 2001-093. U.S. Dept. of the Interior, Minerals Management Service, Gulf of Mexico Region, New Orleans, LA, 89 pp.

TABLE OF CONTENTS

LIST OF FIGURES

LIST OF TABLES

INTRODUCTION

Observations from the five cruises conducted by the Mississippi River Plume Hydrography study portion of the Louisiana-Texas Physical Oceanography Program (LATEX B) (Murray et al. 1997) have provided an unprecedented visualization of the coastal plume that emanates from the combined discharge of the Atchafalaya and Mississippi Rivers into the Gulf of Mexico in central Louisiana. Conductivity-temperature-depth (CTD) casts, underway acoustic Doppler current profilers (ADCP), and thermosalinography on these cruises documented the significant temporal and spatial variability along the length of the Mississippi-Atchafalaya coastal plume (MACP). In addition, the ADCP data, in particular, showed a distinct coherent velocity structure associated with the MACP. Thus, we also use the term Louisiana -Texas Coastal Current (LTCC) to identify the alongshore velocity intensification that extends from these river mouths along the coast westward and downcoast into south Texas. We will also use the conventional terminology downcoast and upcoast. Downcoast refers to the direction of propagation of a coastal Kelvin wave that must travel with the coast to its right in the northern hemisphere (Csanady, 1982). Downcoast movement is thus westward on the Louisiana inner shelf, and southwestward and southward on the Texas coast. Upcoast movement correspondingly is northward, northeastward, and eastward moving from south Texas into Louisiana.

In addition to documenting the spatial and short-term variability exhibited by the LTCC, Murray et al. (1997) demonstrated a strong but asymmetrical seasonal cycle in the transport of the LTCC consisting of a nine-month-long downcoast (winter) regime and a three-month-long upcoast (summer) regime. While seriously aliased by shifting wind patterns and long cruise length scales, the LATEX B data show that from about mid-August (through the fall, winter, and spring) to mid-May dominant easterly wind components drive a coastal current downcoast to the west and south. This current transports about 96 x 10^3 m^3/s of coastal plume waters of which 29% (28 x 10^3 m^3/s) is fresh water. In a normal year, based on Mississippi River discharge and regional winds, the summer flow (e.g. July 1994) in the reversed coastal current reaches 48 x10^3 m^3/s, of which 22% is fresh water.

Dynamical analysis (Murray et al., 1997) demonstrates that the downcoast current regime is controlled by local wind forcing and that buoyancy forcing appears inconsequential. The summer upcoast flow regime off Louisiana and east Texas is clearly not controlled by wind, and the partial coherence analysis suggests that large-scale, alongcoast pressure gradients are probably an important driving mechanism.

While extremely enlightening, these results on the transport of the LTCC are, however, subject to a large error band caused by the spatial and temporal aliasing inherent in underway cruise data. Thus, the aim of the present study as a follow-on and enhancement of the LATEX B study is to conduct high resolution studies of the LTCC and MACP to further quantify the transport and its temporal variability.

The program has two elements, each addressing specific questions arising from the LATEX B analysis. The first is a repeat section study in which the same research ship used in LATEX B analysis transited a control "box" 3 times in about 3 days, each transit taking 20 to 25 hours. The box captured day-to-day variability in the velocity and hydrographic structure across the LTCC just east of the Atchafalaya River mouth. Underway ADCP and a novel underway profiling CTD were used to assess the robustness of our previous single pass estimates of transport and hydrographic structure. Additionally, current meter moorings were deployed on 3 sides of the box that allowed coherence studies over distance of tens of kilometers and time scales of 40 to 50 days.

The second and largest element of the program is a mooring current meter array on a line roughly across the LTCC just east of Cameron, Louisiana. The objective was to obtain a long-term time series of transport in the LTCC from in situ current meter observations. Great difficulty was encountered in this objective because of instrument malfunctions and numerous disruptions to the moorings from oil field activity. Nonetheless, data were sufficient for significant new results to emerge.

PART I

A REPEAT SECTION STUDY WITH CONTIGUOUS CURRENT METER MOORINGS

A. Introduction

The Mississippi River is the major source of fresh water, sediment, nutrients, and pollutants for the northern shelf of the Gulf of Mexico. It drains over one third of the continental watershed of the United States and has an annual average discharge rate of about 19,000 m^3/s (Wiseman et al., 1997). The outflow usually peaks in spring and is at a minimum in late summer. The river enters the Gulf of Mexico through the Mississippi River birdfoot delta and the Atchafalaya River, which is a distributary of the Mississippi River diverted from the main channel at Old River north of Baton Rouge. The thirty percent of the total discharge is delivered to the Louisiana shelf by the Atchafalaya River. The remaining seventy percent flows through the Mississippi River birdfoot delta. However, estimates suggest that only about fifty percent of the fresh water discharged by the birdfoot delta is carried to the western Louisiana shelf (Dinnel and Wiseman, 1986).

Because this large input of fresh water acts to create a buoyant surface layer, one may expect that regional wind forcing would be a great importance. Winds over this part of the Gulf of Mexico show seasonal fluctuations (Gutierrez de Velasco and Winant, 1996). During fall, winter and spring the winds are generally easterly. The dominant synoptic-scale disturbances in this part of the year are cold fronts, propagating mainly from northwest to southeast and bringing strong winds from the northern quadrant. Characteristic time scales of these disturbances in winter are 3 to 10 days (DiMago et al., 1976). The summer months are characterized by weak southerly and southeasterly winds associated with the dominance of the Bermuda high-pressure system (Crout et al., 1984). During this season, a sea-breeze system exists, and squalls, tropical storms and hurricanes aperiodically may impact the region (Wiseman et al., 1997).

A portion of the Mississippi River outflow, which flows westward, joins with the Atchafalaya River discharge, mixes with the shelf waters and ultimately forms a coastal current (Wiseman and Kelly, 1994; Murray et al., 1997). This coastal flow has been called various names in the literature: for instance, it was referred to as the Louisiana Coastal Current by Wiseman and Kelly (1994) and the Texas current by Vastano et al. (1995). The latest studies (Murray et al., 1997) show that despite strong spatial and temporal variability this current can be generally traced west of the Mississippi River delta along the entire Louisiana and Texas coasts. Therefore, it seems reasonable to refer to it as the Louisiana-Texas Coastal Current (LTCC).

During much of the year the Louisiana-Texas Coastal Current flows westward along the shore from Louisiana to Texas. Such a simple scenario may suggest that the flow is in general agreement with geostrophic theory and is driven mainly by the pressure gradient. The theory states that the river outflow is deflected to the right upon entering

the sea in the northern hemisphere (the Gulf of Mexico) producing a buoyant coastal current trapped against the coastline. Such behavior of the flow has been observed, for instance, in the Delaware coastal current (Münchow and Garvine, 1993) and also has been successfully modeled numerically (Chao, 1988).

Observations and analyses do not, however, support such a simple behavior of the Louisiana-Texas Coastal Current. Smith (1975, 1978) reports seasonal variability of the current on the central Texas shelf with a strong south-southwesterly flow in winter and weak north-northeasterly or south-southwesterly flow in summer. He also implies that many features of the nearshore current pattern can be explained as a response to surface wind stress. Crout et al. (1984) describe such variability of the current on the western Louisiana inner shelf. They conclude that the summer current is generally disorganized and probably driven by non-local forcing. In contrast to the summer flow, the winter alongshore current is better organized and is well correlated with alongshore wind stress. Cochrane and Kelly (1986) report that the alongshore wind stress is the major driving force of the coastal current on the Louisiana-Texas shelf in a region west of 92.5W. During much of the year, the current flows downcoast (in the sense of Kelvin wave phase propagation), and it is highly correlated with the downcoast wind stress component. In late summer there is reversal of the flow direction and the upcoast flow regime (in the opposite sense of Kelvin wave phase propagation) prevails. This flow is coherent with the upcoast wind stress component. Li et al. (1997) also report such a bimodal annual pattern of the nearshore circulation on the northern shelf of the Gulf of Mexico and its dependence on the alongshore wind stress.

Murray et al. (1997) confirm the downcoast and upcoast flow regimes of the Louisiana-Texas coastal current. They verify that during the fall-winter-spring downcoast regime, current fluctuations on the Louisiana-Texas shelf are controlled largely by the alongshore wind stress and secondarily off central Texas by the alongshore surface slope. During the summer upcoast flow regime, the current fluctuations in southern Texas are significantly associated with the alongshore surface slope and wind stress components. However, variability of the current in central Texas and central Louisiana is highly coherent with the sea level gradients. Murray et al.'s (1997) scaling analysis of the alongshore momentum balance also shows that the wind stress, basal stress and the barotropic pressure gradient are dominant forcing mechanisms for the downcoast flow. For the upcoast regime, the importance of wind stress decreases, and the barotropic pressure gradient and Coriolis forces are dominant terms of the alongshore momentum balance.

In addition to the seasonal fluctuations of the coastal current, there are two energetic higher frequency motions on the Louisiana-Texas shelf: near inertial and tidal, which are occasionally important. The near inertial oscillations are difficult to determine because of the proximity of the local inertial period to the diurnal tidal period. Despite these difficulties, Daddio et al. (1978) and Chen et al. (1996) describe the presence of such oscillations with amplitudes as large as 40 cm/s on this shelf. They also report that these oscillations are generated by shifting winds that are usually associated with the passage of atmospheric fronts. Recent studies (LATEX A report, 1997) confirm that the

near inertial oscillations are generated by wind in non-summer months on the shelf. However, they also imply that in summer months the large amplitude oscillations are thermally induced.

Tidal currents are rather small and diurnal on the Louisiana-Texas shelf. According to data from the Texas-Louisiana Shelf Circulation and Transport Study (LATEX A report, 1997; DiMarco and Reid, 1998), the K_1 tidal component ranges from 3% to 75% of the total tidal variance and is, therefore, the largest tidal current component on the shelf. O_1, which ranges from 6 to 48% of the total variance, is the second largest tidal component. Among semidiurnal components, M_2 is the dominant one. Together they account for 76% of the total near-surface tidal energy. These tidal currents generally rotate clockwise and their semi-major and semi-minor axes do not exceed 6 cm/s, except in a region south of Atchafalaya Bay where the semi-major axis is 9.58 cm/s for M_2, 8.49 and 8.22 cm/s for O_1 and K_1, respectively.

Our understanding of the motions of various frequencies on the Louisiana-Texas shelf has improved greatly with recent studies. However, knowledge of the behavior of these motions in different locations and seasons remains decidedly lacking. This report focuses on the description of summer flow regime on the portion of the Louisiana-Texas shelf located south of Isle Dernieres, just east of the injection of the Atchafalaya River discharge into the eastward flowing Louisiana-Texas coastal current. This description will be based on a data set from the Louisiana Coastal Current Summer Flow Regime project (LOCCOSUM) that was designed to provide a more detailed characterization of the variability of currents and hydrography in the summer season. Thus, the objectives of this study are: (1) to describe day-to-day changes in horizontal velocity components and hydrography (salinity) along four sections across and along the coastal current; (2) to estimate the average tidal currents in this region; (3) to determine whether weak to moderate summer winds can induce near inertial oscillations in the upper layer of the water column; and (4) to describe the variability of the low frequency flow and determine what mechanisms drive the low frequency current on this portion of the Louisiana-Texas shelf.

B. The Study Area and Data Sources

The area examined in this study is located on the inner shelf of Louisiana south of Isles Derniere between 90° 27'W and 91° 15'W longitude and 28 ° 30'N and 29 ° 1.2'N latitude (Figure I-1). This region of the shelf is rather shallow with a depth range from about 6.5 m near the coast to above 40 m in its southern part. The shape of the coastline and isobaths is quite complicated in the region and its vicinity. They do not run simply from east to west but bulge seaward as a result of subsidence and reworking of abandoned Mississippi River deltas. Generally, they trend west-northwest to east-southeast in the western part and northeast to southwest in the eastern part. A change in the isobath direction appears approximately in the middle of the study area.

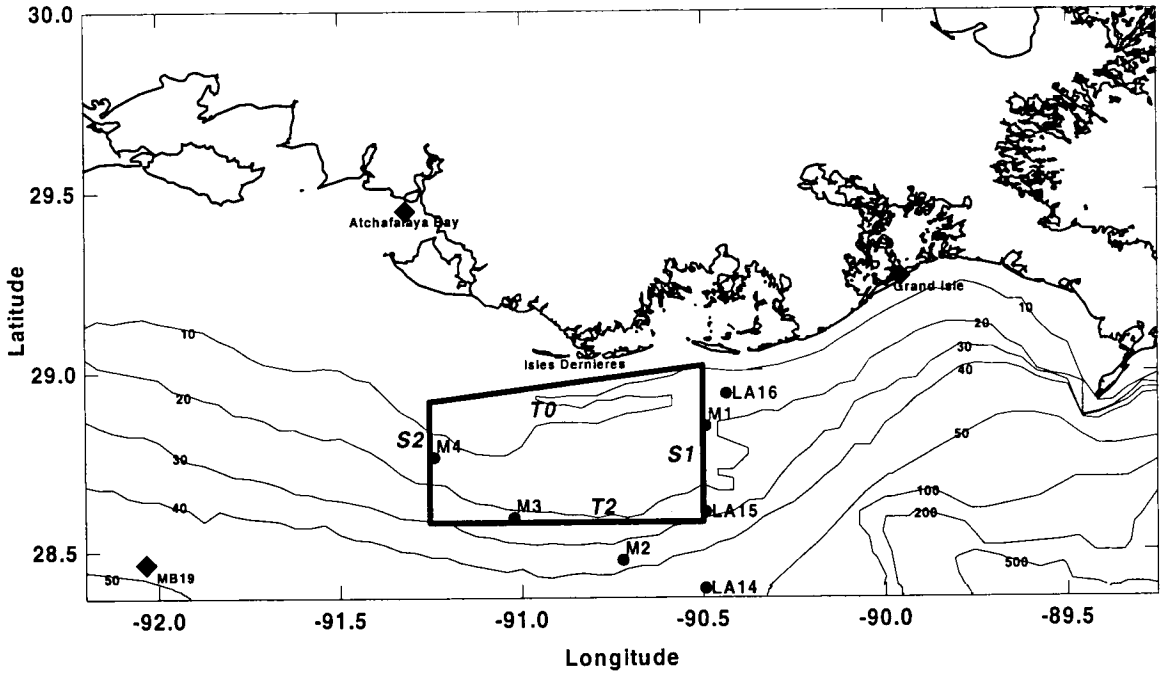

Figure I-1. Map of the study area (depth contours are in meters; M1-M4 are the current meter moorings deployed for this study; LA14-LA16 are moorings from the LATEX A project; S1, S2, T0, and T2 are the ship transit lines; MB19 identifies a m eteorological buoy from the LATEX A project; locations of a CMAN meteorological and water level stations at Grand Isle and a water level gauge at Atchafalaya Bay are indicated by diamonds).

Hydrography and circulation of this particular part of the shelf are highly impacted by fresh water, which is introduced to the system by the Mississippi and Atchafalaya Rivers. During the summer of 1994 both rivers had relatively low outflows. Except for the very beginning of June their combined discharge measured at Tarbert Landing did not exceed 12,000 m^3/s and had a minimum on August 22 (Figure I-2).

In addition to buoyancy forcing represented here by the river outflow, wind is also an important mechanism that influences both hydrography and circulation in this region. A three month-wind record (June, July, August) from a meteorological buoy (MB19, see Figure I-1 for location) shows that the winds during the summer of 1994 were typical with speeds lying generally between 3 and 6 m/s (Figure I-3) and blowing mainly from southwestern, southern and southeastern directions (Figure I-4).

LOCCOSUM data originate from two sources: a four-day cruise to collect current, salinity and temperature data, and four moorings deployed around the periphery of the study area. The cruise was conducted from June 30 to July 03 1994, and this part of the project was named "repeat section study" (RSS). The ship track of the R/V Pelican along with annotated sections of RSS is shown in Figure I-1. The sections marked S1, T2, S2, and T0 were profiled underway with two instruments: a 1200kHz acoustic doppler current profiler (ADCP) and a conductivity temperature density profiler (CTD).

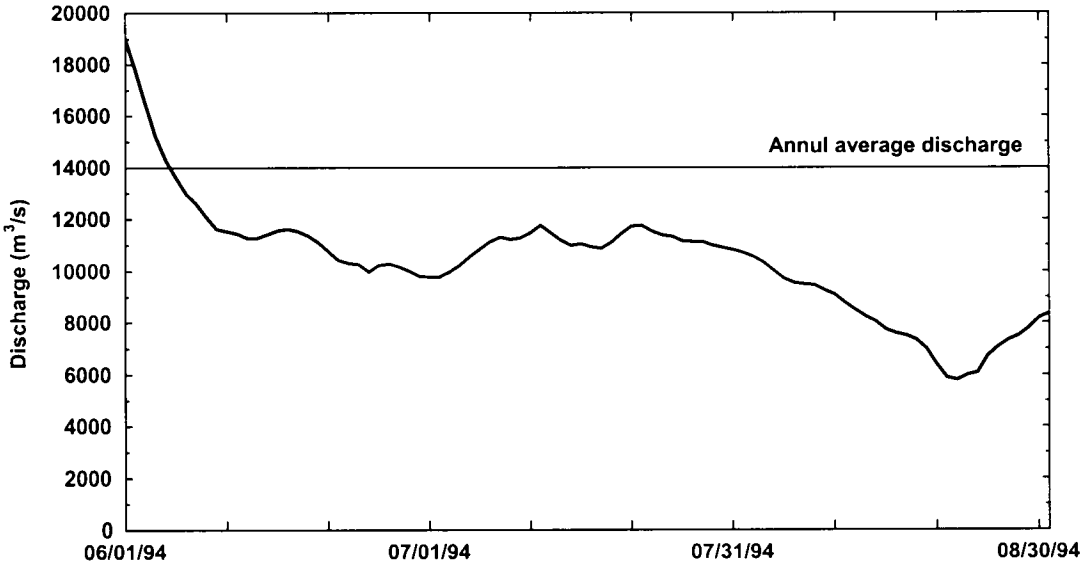

Figure I-2. Daily Mississippi River discharge at Tarbert Landing in summer 1994. The thin horizontal line indicates the annul averaged discharge of 14,000 m^3/s.

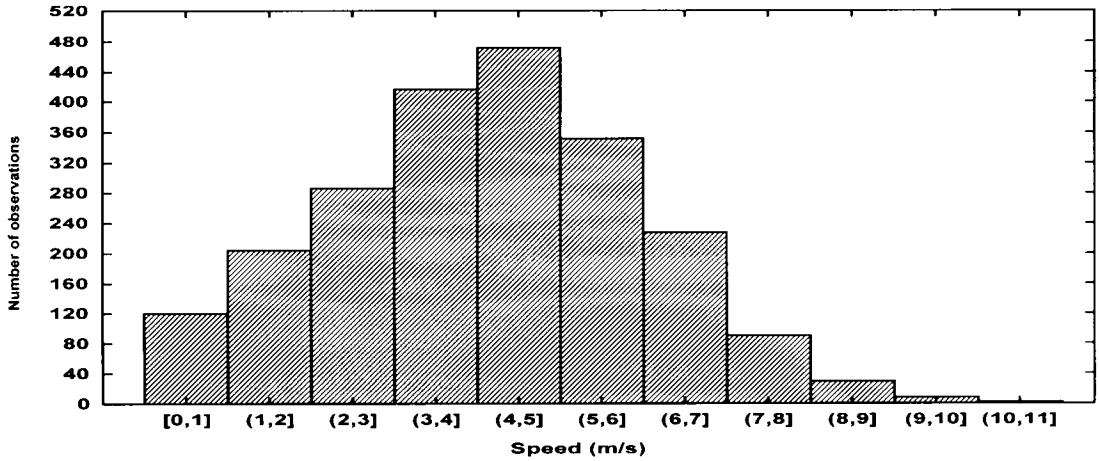

Figure I-3. Histogram of wind speed (1 m/s intervals) vs. number of observations, 06/01-08/31/1994.

The shallowness of the study area allowed using the ADCP instrument in the bottom-tracking mode. Horizontal velocity components obtained from the ADCP had a one-meter vertical bin resolution and a two-minute sampling interval. After applying correction coefficients and removing ambiguous readings, the velocity data were obtained for a depth range from 3.5 m to 15.5 m in 1-meter increments. However, if the total depth (H) was less than 15.5 m the depth range was lower, and it extended from 3.5 m to about 0.8H meters with the same vertical increment. The CTD instrument mounted in a side-scan sonar housing profiled at a one-second sampling interval allowing the excellent horizontal and vertical resolution of salinity, temperature and density data.

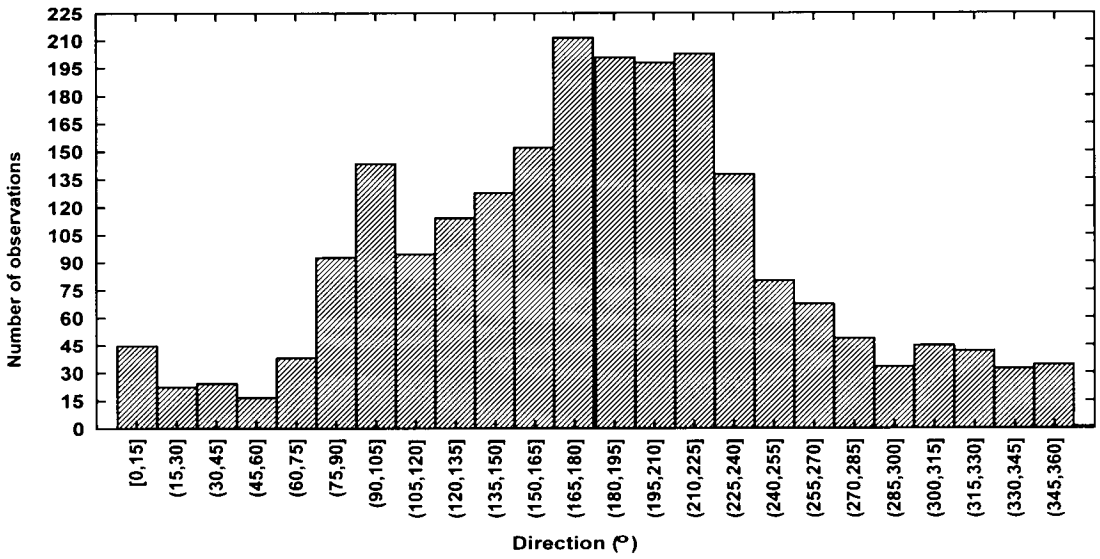

Figure I-4. Histogram of wind direction (15° intervals) vs. number of observations, 06/01-08/31/1994.

The circuit around the box was repeated three times with each pass starting at the northeastern corner of the S1 section, which was located at 29° 0.96'N and λ=90° 30'W. The first pass took 25.17 hours to be completed. The second and the third passes took 20.43 and 20.67 hours, respectively.

On the third and fourth days of the cruise four moorings were deployed (M1, M2, M3, M4) at locations shown in Figure I-1. Each mooring had the same instrument configuration and consisted of two Endeco current meters and a SeaCat. The current meters were deployed at depths of 5.46 m and 10 m. The SeaCat was placed 6.86 m below the sea surface. The current meters collected speed and direction of currents with a five-minute time interval. The SeaCat measurements of temperature and salinity were recorded with a ten-minute time interval. Except for the lower current meter at M3, all other instruments worked properly and nearly two-months of continuous data were obtained for further analyses.

In addition to the measurements of this project, current meter data (LA16, LA15, LA14) and wind data (MB19) collected for the Texas-Louisiana Shelf Circulation and Transport Study (LATEX A project) were also analyzed (see Figure I-1 for locations). The LA16 and LA14 meters were located 9 m below the sea surface. The LA15 meter was located at 10 meters. The meteorological buoy (MB19) contained an anemometer, which was placed 3.6 m above the sea level and measured wind speeds and directions. Additionally, wind data from the CMAN station at Grand Isle, water levels from gauges at Atchafalaya Bay near Eugene Island and at Grand Isle and discharge of the Atchafalaya River at Simmesport were also used in the analyses.

C. Results of Data Analyses

1. Repeat Section Study

1.1. Meteorological Conditions

Winds measured at station MB19 and Grand Isle (located about 220 km apart) before and during the repeat section study (RSS) are shown in Figure I-5. The cruise was preceded by a week of moderate southwesterly winds, which should set up an eastward current in the study area. According to MB19, Pass I started (17:30GMT, June 30 1994)

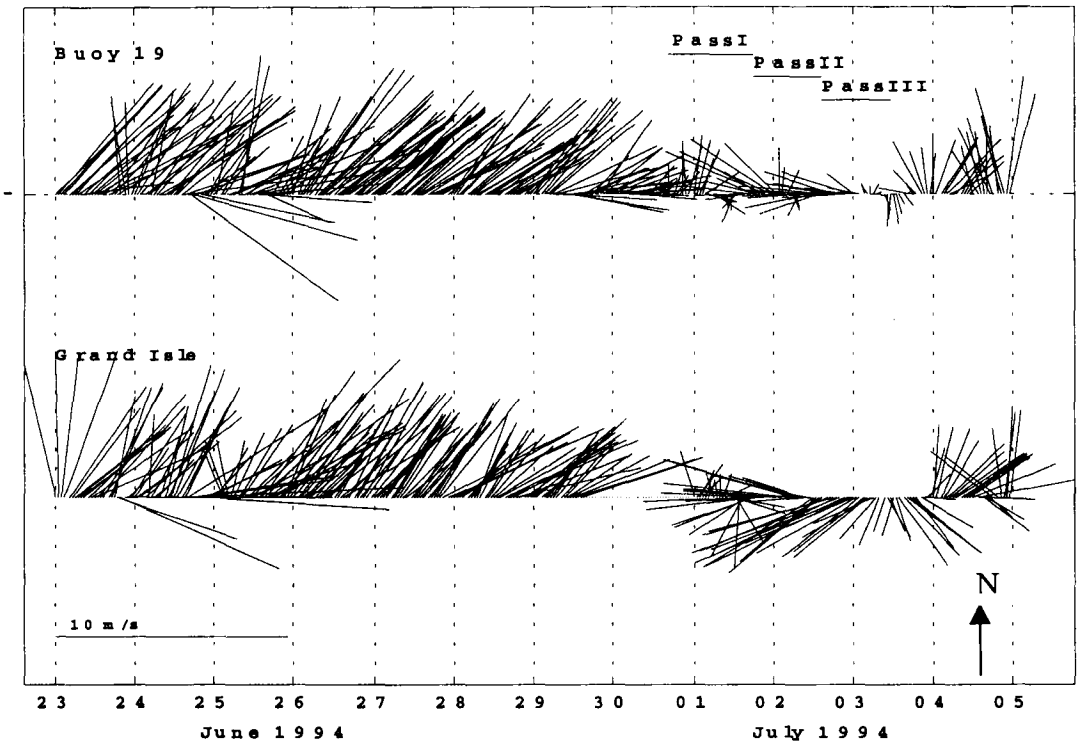

Figure I-5. The time series of the wind velocities measured at MB19 and Grand Isle, 06/23-07/04/1994 (the day number marks the beginning of the day).

with very light southerly winds, which accelerated to 3 m/s and then blew steadily from the south for 6 hours. During the remaining part of the cruise they were generally weak to moderate (0.5-5 m/s) and rotated clockwise, except for the winds measured on July 2 1994, which were easterly for most of the day.

1.2. Hydrography

During the entire RSS, a well-developed stratification with three distinct salinity layers was observed all around the box. Examples of this salinity structure are shown in Figure I-6. The upper part of the water column was occupied by low salinity waters (~22

psu). This freshwater layer was underlain by a well-defined halocline, which was usually 4 m thick and located from 6 to 10 m below the sea surface, except for T0. Below the base of the halocline layer there was a relatively homogeneous deep layer filled with Gulf waters (34-36 psu). Thickness of these layers varied from one place to another. The weak and moderate winds present during the cruise were not able to break down this stratification, and the three-layer salinity pattern was maintained along all sections through Pass II and Pass III.

Superimposed on this general three-layer structure were some notable deviations in the salinity distribution. During Pass I on line S1, we observed a lens of low salinity waters detached from the shoreline and the halocline sloped markedly up to the coast, both classic signals of upwelling conditions. The measurements from the next two passes (Figure I-7) showed a shoreward movement of this lens, for example, the 20 psu isohaline moved shoreward about 30 km from Pass I to Pass III. Such behavior of the lens and downward movement of the halocline at the inshore end of this section may suggest the relaxation of the upwelling episode along S1. The wind records from MB19 and Grand Isle prior to the RSS cruise indicate that the winds were indeed upwelling favorable. During the cruise, the winds weakened and blew from various directions. Therefore, the measurements probably recorded the end of the upwelling event when the system began returning to equilibrium.

The end of this upwelling episode was not observed along the S2 cross-section located about 74 km west of S1. That may have resulted from the different configuration of the isobaths and coastline in this region. The winds, which caused the upwelling along S1, apparently were not able to set up such conditions at S2 because they were approximately perpendicular to the coast and the isobaths, rather than more parallel as favored by upwelling theory.

Another interesting feature in the salinity distribution was observed along the shallowest inshore section of the RSS, T0. In its upper few meters, very fresh water with salinity of 14 psu was observed during all three passes. This distinct lens of the light waters was 2-3 m thick and had an alongshore length scale of 10 to 20 km. It was generally located in the western part of the section and may have represented the eastward flowing Atchafalaya River discharge and/or the outflow from channels and bays situated northward of T0.

In contrast to the salinity distribution, vertical temperature structure did not show much variability. All sections contained warm waters, in which temperature varied from 30°C in the very upper part of the water column to 21°C in the deepest parts of the study area. Density distribution followed closely the vertical salinity structure at all sections as expected in coastal waters highly influenced by large fresh water input.

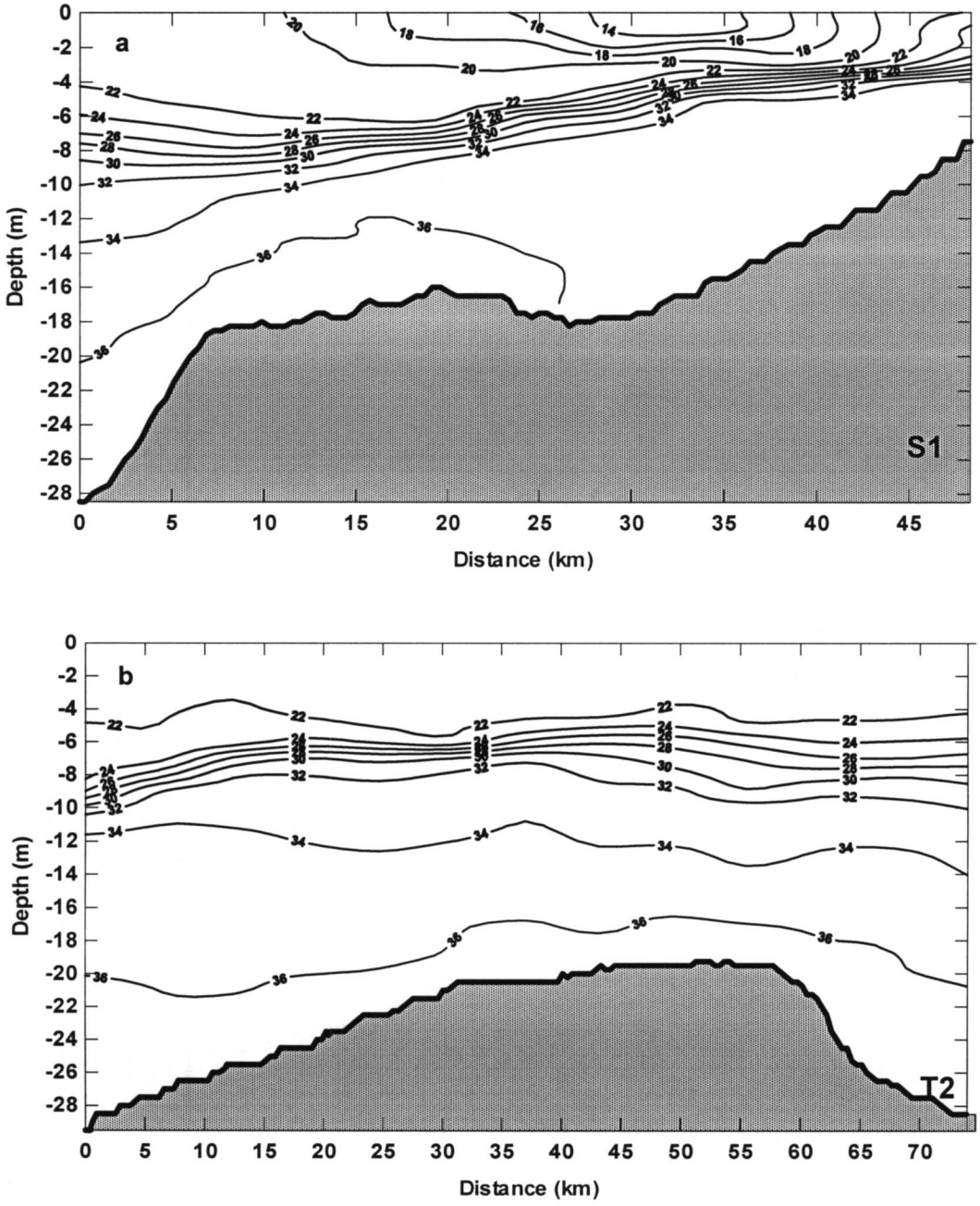

Figure I-6. Vertical distribution of salinity (psu) along (a) S1, (b) T2, (c) S2, and (d) T0 sections during Pass I.

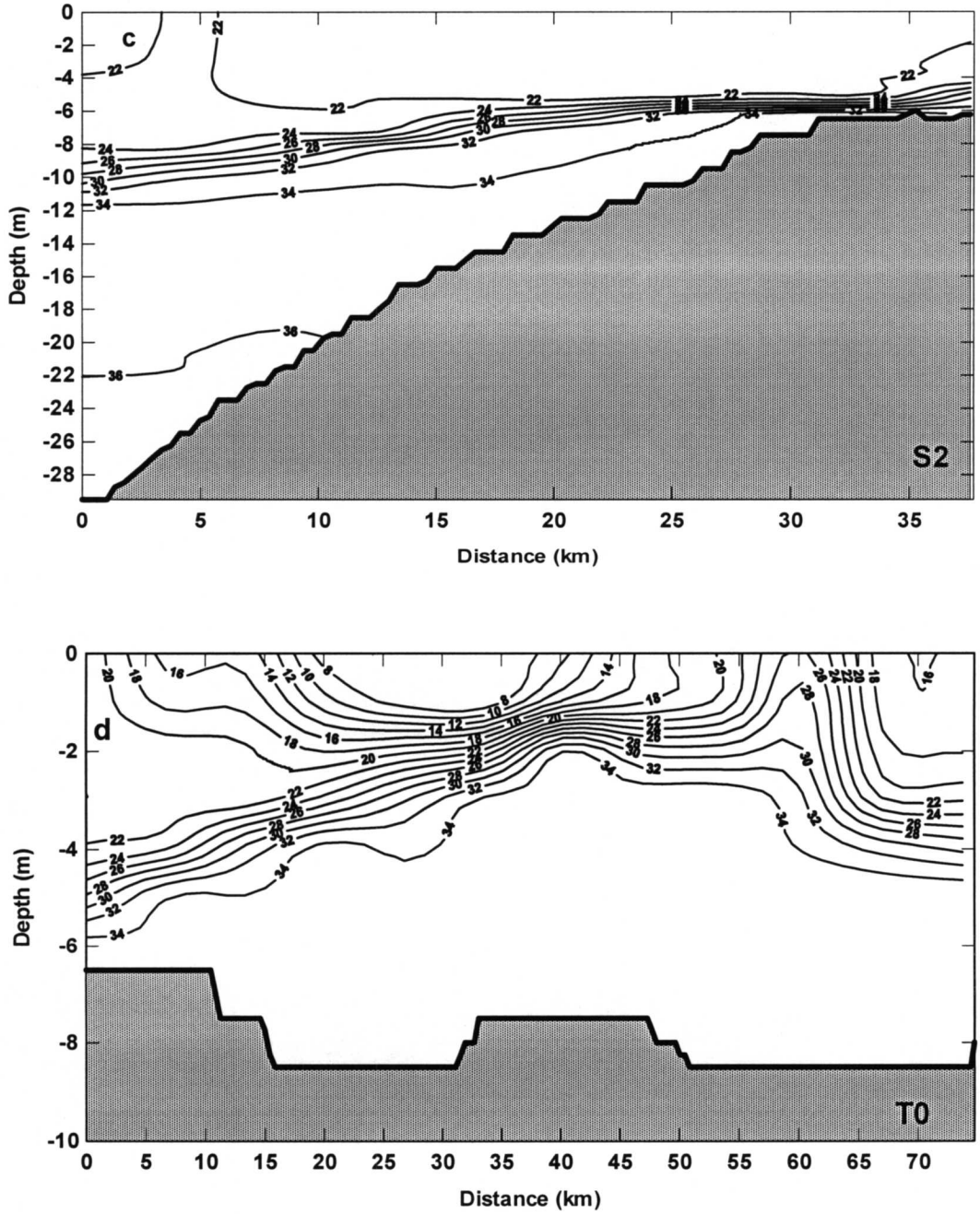

Figure I-6. Vertical distribution of salinity (psu) along (a) S1, (b) T2, (c) S2, and (d) T0 sections during Pass I (continued).

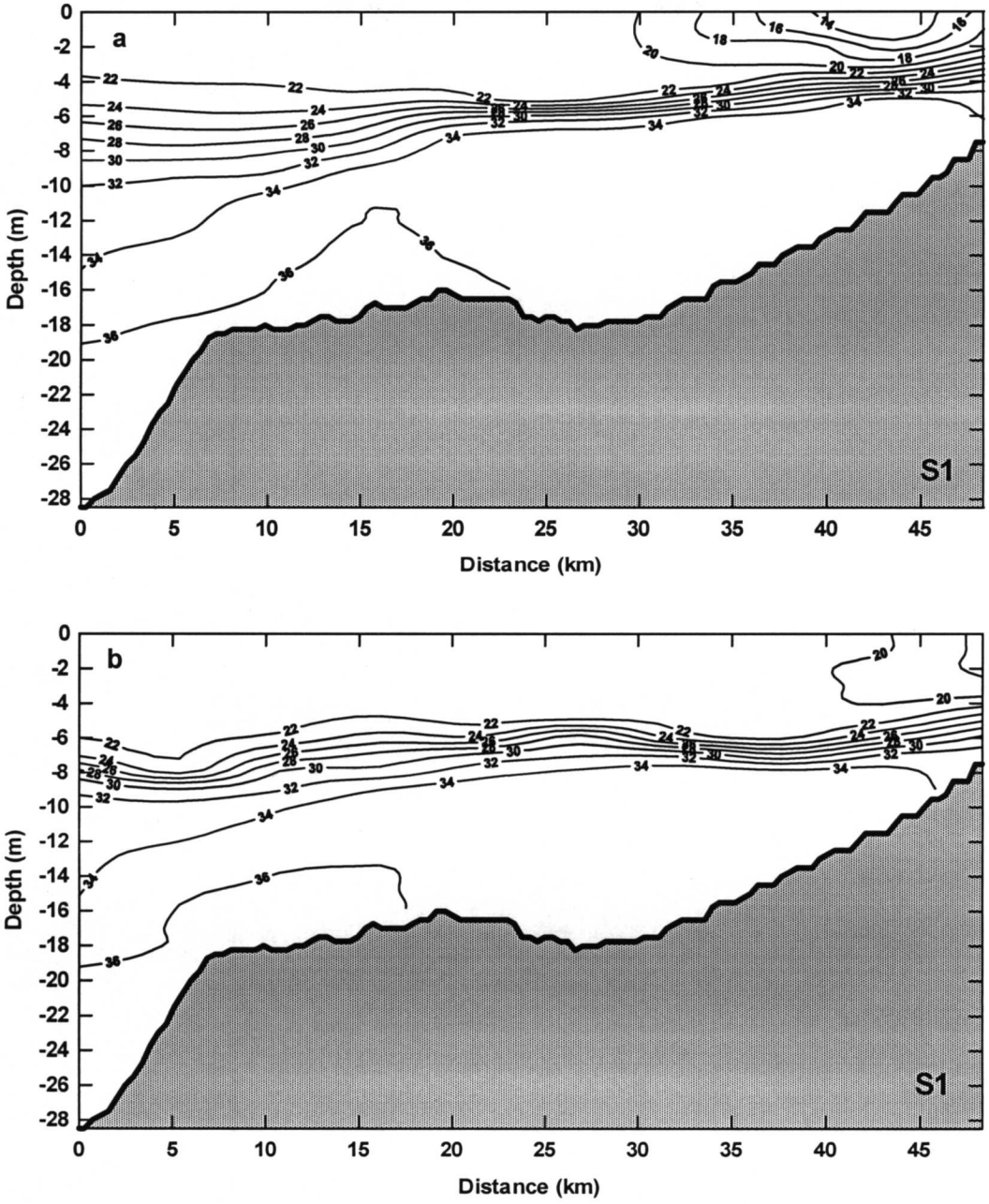

Figure I-7. Vertical distribution of salinity (psu) along S1 during (a) Pass II and (b) Pass III.

1.3. Vertical Distribution of the Horizontal Current Velocity Components

Vertical distributions of horizontal current components around the box showed that the alongshore component of the flow at each section was usually more energetic than the cross-shore component through all three passes. Day-to-day changes in the current field were more distinct in the shallowest parts of the study area (total depth less than 10 m) where the flow was generally driven by the wind and responded quickly to any variations in wind speed and direction. Offshore of this shallow region, in general, we observed a well-developed upcoast flow (in the opposite sense of Kelvin wave phase propagation) in the upper part of the water column throughout the entire RSS.

Examples of the observed changes in the alongshore component through Pass I to Pass III along two cross-sections (S1 and S2) normal to the coast are shown in Figure I-8 (a-c). During the first pass, the strong upcoast flow was observed at both sections (Figure I-8a). These upcoast currents were characterized by a subsurface maximum, which was more energetic at S1. Such a subsurface intensification of the flow may result from a cross-shore baroclinic pressure gradient. Observed sloping density contours imply that such a cross-shore baroclinic pressure gradient was present during Pass I. The difference in the subsurface speeds of the flow at S1 and S2 may again originate from a difference in the cross-shore baroclinic pressure gradient, which depends on the cross-shore density gradient. The density gradient at S1 was larger than that measured at S2. Therefore, if the intensification is baroclinic in origin, the speeds should be higher at S1. At S2, a surface intensification of the flow was also observed and its origin is difficult to explain. It may have come from the cross-shore barotropic pressure gradient or it may have been wind driven.

Subsequent to Pass I, the upcoast flow generally decelerated and a deeper countercurrent emerged during the next two passes (Figure I-8b and I-8c). However, both deceleration and countercurrent were more distinct along the S1 section. Such deterioration of the upcoast flow was also present along the southernmost section, T2 (not shown). This upcoast flow, which was observed throughout the entire RSS, was probably set up by the southwesterly winds blowing prior to the cruise and may have represented a well-developed phase of the LTCC in its summer flow regime.

The weak narrow downcoast current flowing below the energetic upcoast current was first observed only at S1 (Pass I). During the second pass, this countercurrent became stronger and broader (Figure I-8b). Figure I-8c shows that a weak downcoast flow was even present at S2 when the section was sampled for the third time. The countercurrent, especially that at S1, may originate from the upwelling episode observed along this section since such a current is a persistent feature observed in upwelling regions (Smith, 1968). According to Yoshida's two-layer model (1967), a uniform wind field implies a condition of no net alongshore transport requiring a compensating countercurrent under the surface layer.

As has been stated previously, the signature of the end of the upwelling episode was observed along the S1 line in both salinity and alongshore flow structure. The cross-shore flow field was also consistent with a circulation pattern observed in upwelling

regions. During Pass I, the vertical structure of the cross-shore velocity component still showed very well developed upwelling circulation (0-20 km) with an onshore flow in the lower part and an offshore flow in the upper part of the water column (Figure I-9).

1.4. Volume Transport

The sections sampled during the repeat section study were designed to enclose a volume; therefore, it was of interest to determine the volume flux for each section and to investigate the volume divergence for the box. Unfortunately, the horizontal velocity components were available only to a depth of 15.5 m. Therefore, the volume transport was determined by integrating the velocity speed normal to each section from the sea surface down to 15.5 m if the total depth was higher or to the total depth in the shallow part of the study area. Two assumptions were required in order to estimate the net box transport. The first stated that there was no exchange of volume through the sea surface that bounded the box from the top (evaporation minus precipitation is zero). Another said that there was also no volume exchange through the bottom of the box. The latter was made because of the lack of the vertical velocity data and might be false. Results are listed in Table 1.

Table I-1

Section volume fluxes and net box flux in m^3/s, section area in m^2.

Section	Pass I	Pass II	Pass III	Area
S1	120,830	27,545	-10,583	717,000
T2	-56,381	-25,361	-29,214	1184,000
S2	121,611	84,338	48,835	459,000
T0	-49,894	-11,714	2,539	564,000
Box	-5,706	43,146	27,665	

The positive and negative flux of S1 and S2 are considered to be eastward and westward, respectively. T2 has positive northward and negative southward transport. The coordinate system was rotated 7.7° counterclockwise from the north in order to estimate the velocity component perpendicular to T0, and positive and negative values of the flux are directed toward 7° and 187.7°, respectively. The box net transport is estimated by assuming that the waters flowing into the box have positive volume flux and the waters flowing out of the box have the negative volume flux.

The results show that all section volume fluxes decreased from Pass I to Pass II. The most significant decrease appeared for the S1 and T0 sections and resulted from drastic changes in the current flow field. During the third pass, the transport even had an opposite sign as a result of further modifications of the current flow in these two sections. The smallest section, if area is considered, S2, had the largest and most unidirectional volume flux that was eastward during all three passes. However, this eastward transport decreased on account of decelerating eastward flow from one pass to another. Similar to S2, the flux of T2 was unidirectional (southward), which diminished from Pass I to Pass

a

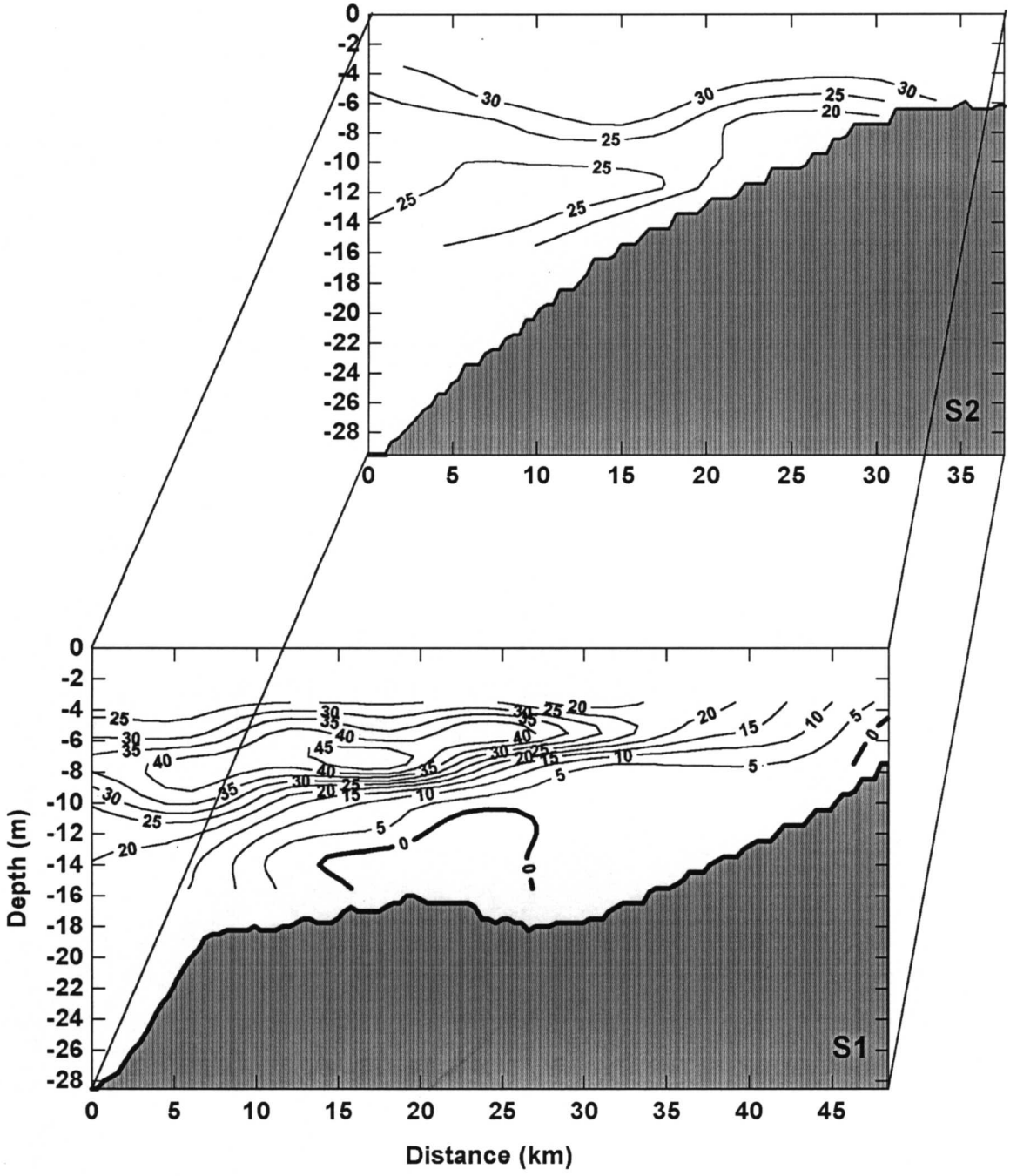

Figure I-8. Vertical distribution of the alongshore velocity current component (cm/s) along S1 and S2 during (a) Pass I, (b) Pass II, and (c) Pass III (positive values are upcoast; negative values are downcoast).

b

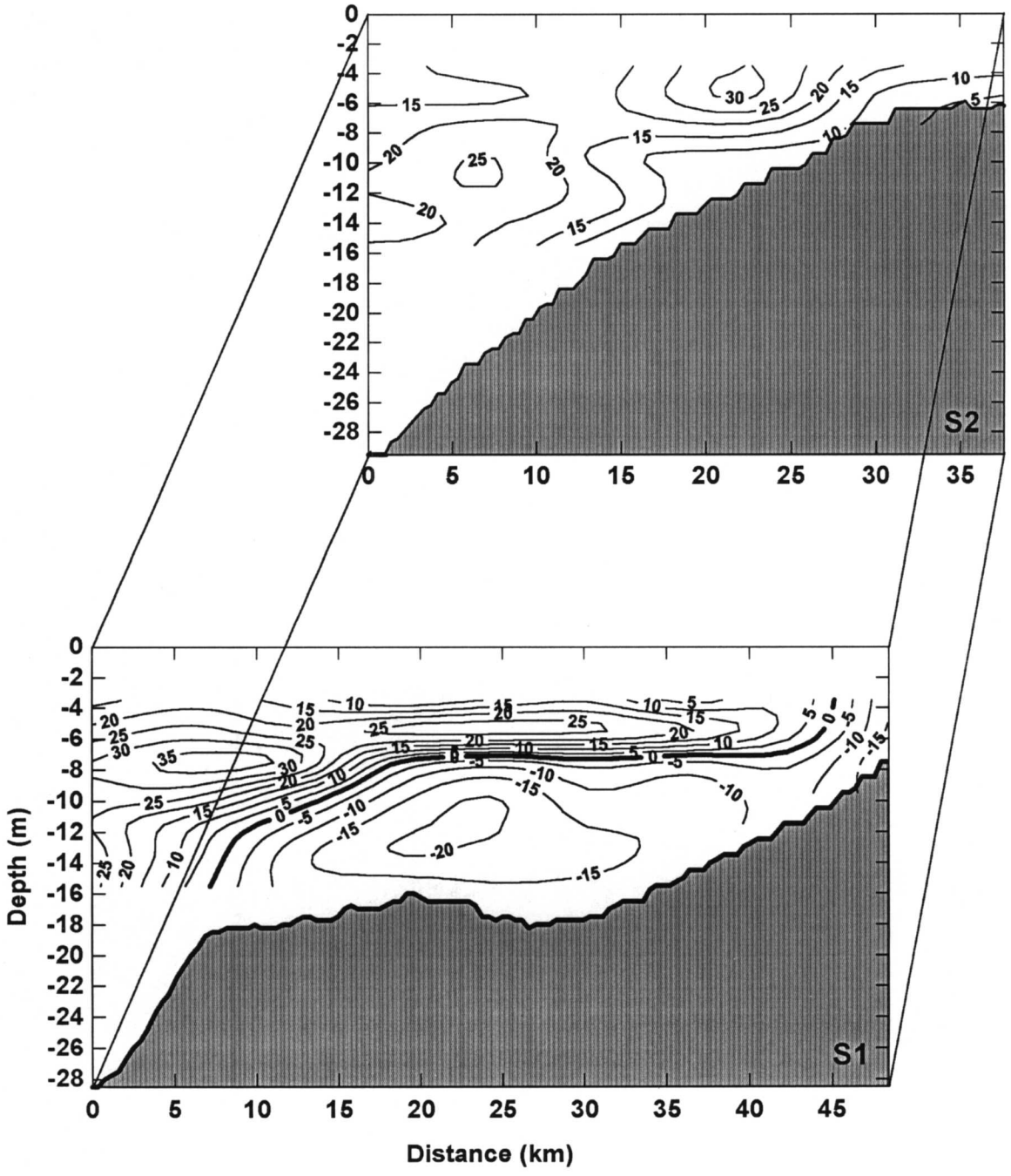

Figure I-8. Vertical distribution of the alongshore velocity current component (cm/s) along S1 and S2 during (a) Pass I, (b) Pass II, and (c) Pass III (positive values are upcoast; negative values are downcoast) (continued).

c

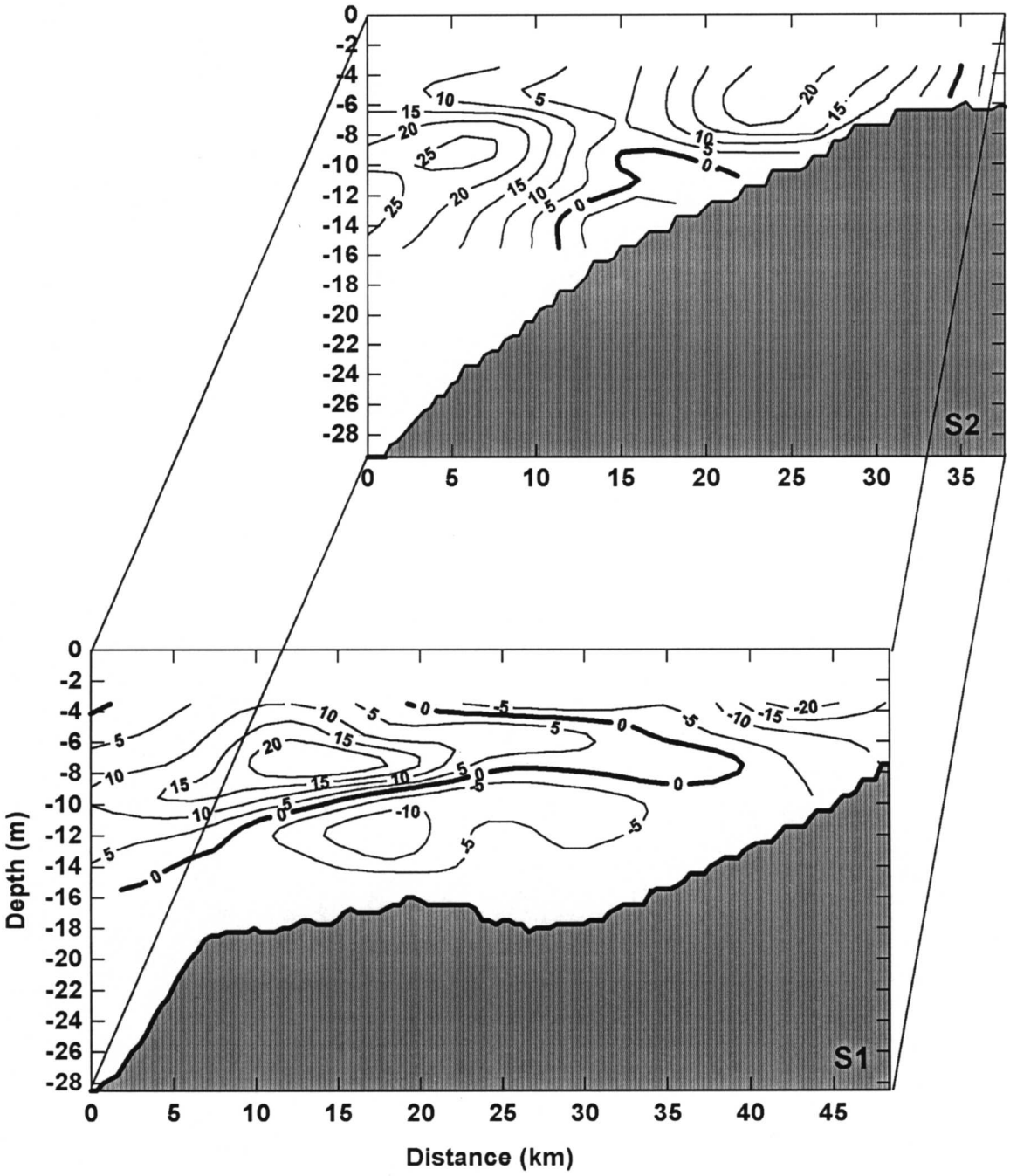

Figure I-8. Vertical distribution of the alongshore velocity current component (cm/s) along S1 and S2 during (a) Pass I, (b) Pass II, and (c) Pass III (positive values are upcoast; negative values are downcoast) (continued).

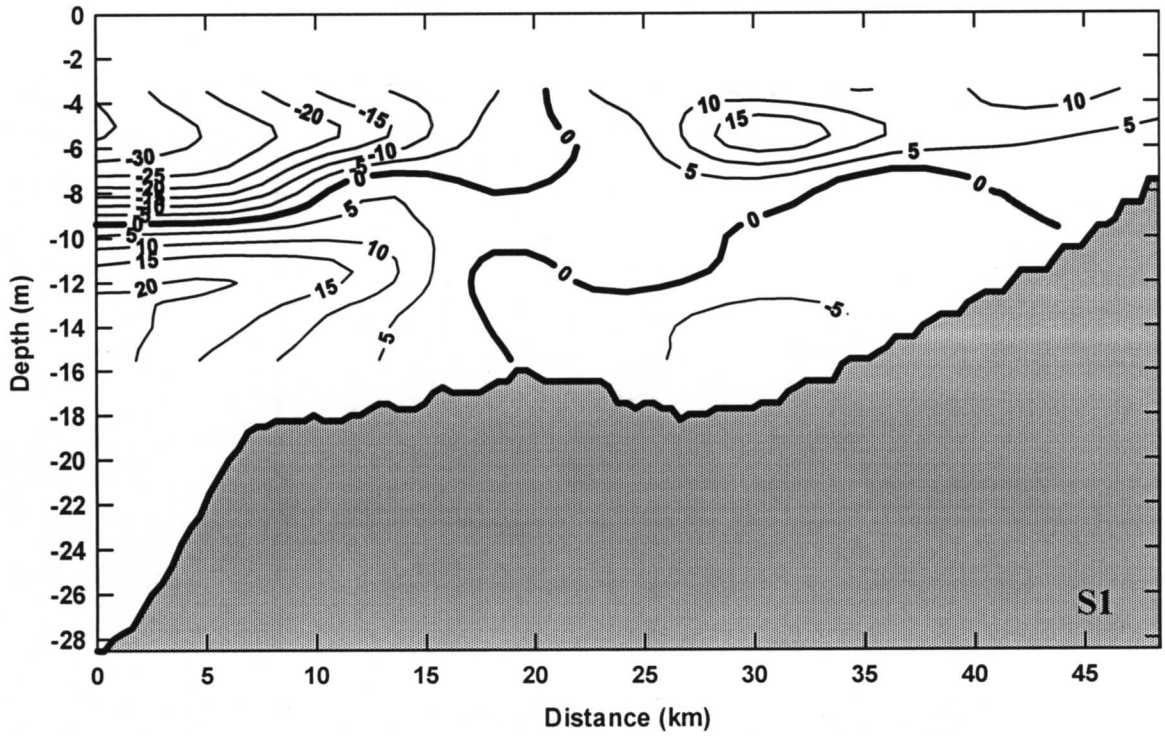

Figure I-9. Vertical distribution of the cross-shore velocity current component (cm/s) along S1 during Pass I (positive values are onshore; negative values are offshore).

II and then increased for the last pass. However, this increase (about 4000 m^3/s) might be considered insignificant because of the ADCP data resolution (~2 cm/s).

The results also show that the net box flux is not equal to zero for all passes. Since an error of the volume flux estimations resulting from instrument accuracy is 7240 m^3/s, the net flux of the first pass might be considered approximately zero. The next two are significantly higher, and it might suggest that there was exchange of the volume through the lower boundary of the box. Such negative vertical flux may have occurred since the end of the upwelling episode was observed during the RSS, at least in the eastern part of the study area. Lack of information about vertical velocity distribution prevents determining whether such downward flow of waters through the lower boundary of the box really existed. However, the available data allow at least estimating the average vertical velocity that is required to compensate the box net transport. Its value calculated by division of the net flux by the area of the box bottom is $O(10^{-3})$ cm/s. Vertical velocity may be also approximated by division of the displacement of the 32 psu isohaline by time of the first or second pass. The obtained results give the same amplitude order of the vertical velocity as that estimated from the net box transport. These estimates seem to be reasonable and may explain why the net box fluxes of the last two passes are not equal to zero. Finally, periodic motion, which was not removed from the raw data, may be responsible for different than zero net box flux.

2. Tidal Motion

Since little is known about tidal forcing in the study area, time series obtained from seven current meters deployed for this project were examined to evaluate average tidal currents. It should be noted that the currents estimated in this chapter represent the average tidal currents during the period July 3 through August 29 1994, and they are not corrected for the nodal variation of the moon's declination.

Based on the Rayleigh criterion, three diurnal tidal periods (O_1, K_1 and Q_1) and three semi-diurnal tidal periods (S_2, M_2 and N_2) were analyzed (Pugh, 1987). The phase and amplitude were estimated from 3- to 40-hour band pass filtered data of the horizontal velocity components. The names, symbols and periods of all analyzed tidal constituents are given in Table I-2.

Table I-2

Tidal constituents.

Symbol	Name	Period (solar hours)
	Semi-diurnal constituents	
M_2	principal lunar	12.42
N_2	larger lunar elliptic	12.66
S_2	principal solar	12.00
	Diurnal constituents	
K_1	luni-solar diurnal	23.93
O_1	principal lunar diurnal	25.82
Q_1	large lunar elliptic	26.87

The tidal constituents were determined using least squares harmonic analysis (Dronkers, 1964) that treats the observed tides as the sum of a finite number of harmonics. The method seeks to fit the following model to the data

$$u(t) = A_0 + \sum_{k=1}^{M} [A_k \cos(\omega_k t) + B_k \sin(\omega_k t)] \qquad (I-1)$$

where A_o, A_k and B_k are coefficients to be found, t is the time and the ω_k are known frequencies representing a tidal constituent. u denotes a horizontal velocity component. This model, when least squares error constraint is imposed, gives for each velocity component a system of 2M+1 linear equations that can be easily solved.

Table I-3 summarizes the results of the harmonic analysis performed for seven meters from four mooring places M1, M2, M3 and M4 (see Figure I-1 for locations). The table contains information about semi-major and semi-minor axes, direction of the semi-major (positive anticlockwise from the east) and rotation sense. These parameters were

constructed from the phase (referenced to 22:00 UTC, July 3, 1994) and amplitudes of the east-west (u) and north-south (v) components of each tidal current constituent (Mooers, 1973; Pugh, 1987).

The results show that the M_2 tide dominates among semi-diurnal constituents. Values of the major and minor axes are in fairly good agreement with the results obtained for current meters of the LATEX A project (LATEX A report, 1997; DiMarco and Reid, 1998). At the easternmost mooring (M1) values do not exceed 2 and 0.5 cm/s for the major and minor axes, respectively. Farther to the west, the M_2 tidal currents increase with the maximum at the mooring M4. That westward increase of the length of the major axis was also observed in data from the LATEX A program (LATEX A report, 1997; DiMarco and Reid, 1998). The S_2 and N_2 tidal currents are weaker than those described above. Similar to the M_2 current, their maximum major axis was found for the lower meter of the M4 location. The direction of the major axis and sense of rotation generally vary from one place to another.

According to the data, the largest tidal currents on this portion of the shelf are diurnal and the largest constituents are K_1 and O_1. They all rotate clockwise. However, their major and minor axes are significantly different from those evaluated from the data of LATEX A project (LATEX A report, 1997; DiMarco and Reid, 1998). The first possible reason for this discrepancy may be the shorter time span of the records that were used in the analysis. The longer the data record, the better are the estimates of the deterministic tidal currents, and the less other tidal frequencies contribute to the final results (Chen et al., 1996). Another reason, closely associated with the previous one, is the presence of strong near inertial oscillations. The latitude of the moorings on the shelf defines the range of inertial period of 24.81 hours at the northernmost mooring and 25.11 hours at the southernmost mooring. This range of inertial periods is slightly different from the periods of the diurnal tides. Therefore, if near inertial oscillations are present in the data, they may contaminate the estimates of the diurnal constituents obtained from harmonic analysis.

To show that both short record and near inertial oscillations may cause discrepancies, the data were divided into 15-day overlapping segments. The first subset began on July 3, 1994 and lasted to July 17, 1994. The second segment contained data from July 4, 1994 to July 18, 1994 and so on. Forty-two subsets were obtained for determining amplitudes of the tidal currents. Results of the analyses at all current meters show identical behavior of the diurnal amplitudes to those for the upper current meter at mooring M2 (Figure I-10). Figure I-11 presents the 3-40 hour band pass of the horizontal velocity components for the same instrument. The conclusion that may be drawn by comparing these two figures is that whenever the amplitudes of both horizontal velocity components are large and included in the subsets, the estimates of the diurnal amplitudes are extremely high.

Finally, in order to obtain a more adequate approximation of the barotropic tidal current on this part of the shelf, a different approach was applied to the data. The velocity components measured by the upper and lower current meters at moorings M1, M2 and

Table I-3

Semi-major axis, semi-minor axis, semi-major axis direction and sense of rotation (CW =clockwise, CCW=anticlockwise) of tidal currents for M_2, S_2, N_2, K_1, O_1 and Q_1.

Mooring Number	Depth of an Instrument (m)	Semi-major Axis (cm/s)	Semi-minor Axis (cm/s)	Major Axis Angle (°)	Rotation Sense
		M_2			
M1	5.46	1.13	0.04	-47.24	CCW
	10	1.77	0.31	76.05	CCW
M2	5.46	2.39	1.07	-17.41	CW
	10	2.83	1.10	-58.93	CW
M3	5.46	2.32	0.79	26.34	CCW
M4	5.46	3.69	0.71	27.86	CW
	10	5.53	1.22	34.26	CW
		S_2			
M1	5.46	0.32	0.08	14.52	CCW
	10	0.62	0.02	-4.42	CW
M2	5.46	0.85	0.23	-54.02	CW
	10	1.52	0.55	7.60	CW
M3	5.46	0.41	0.24	6.00	CW
M4	5.46	1.02	0.11	-8.20	CCW
	10	2.23	1.42	27.38	CW
		N_2			
M1	5.46	1.12	0.61	-13.32	CW
	10	0.82	0.07	-12.46	CW
M2	5.46	1.51	1.18	-57.86	CW
	10	1.33	0.27	48.51	CW
M3	5.46	1.23	0.47	60.41	CW
M4	5.46	1.28	0.10	-36.91	CCW
	10	3.36	0.07	39.53	CCW
		K_1			
M1	5.46	3.91	1.54	-16.54	CW
	10	3.75	1.07	16.13	CW
M2	5.46	11.93	9.99	55.41	CW
	10	8.28	5.35	20.02	CW
M3	5.46	6.32	4.59	68.85	CW
M4	5.46	3.28	1.50	-53.86	CW
	10	7.99	2.62	-3.18	CW

Table I-3

Semi-major axis, semi-minor axis, semi-major axis direction and sense of rotation (CW =clockwise, CCW=anticlockwise) of tidal currents for M_2, S_2, N_2, K_1, O_1 and Q_1 (continued).

O_1					
M1	5.46	4.58	2.03	5.46	CW
	10	6.87	5.2	21.36	CW
M2	5.46	7.82	5.11	62.33	CW
	10	6.40	4.86	23.37	CW
M3	5.46	4.36	2.57	82.09	CW
M4	5.46	2.96	1.58	35.26	CW
	10	4.12	0.19	2.51	CW
Q_1					
M1	5.46	2.45	1.88	2.35	CW
	10	3.49	2.02	0.00	CW
M2	5.46	1.96	0.83	22.28	CW
	10	1.01	0.12	-9.92	CW
M3	5.46	4.22	3.76	44.54	CW
M4	5.46	1.03	0.08	-7.90	CW
	10	3.03	0.75	-33.83	CW

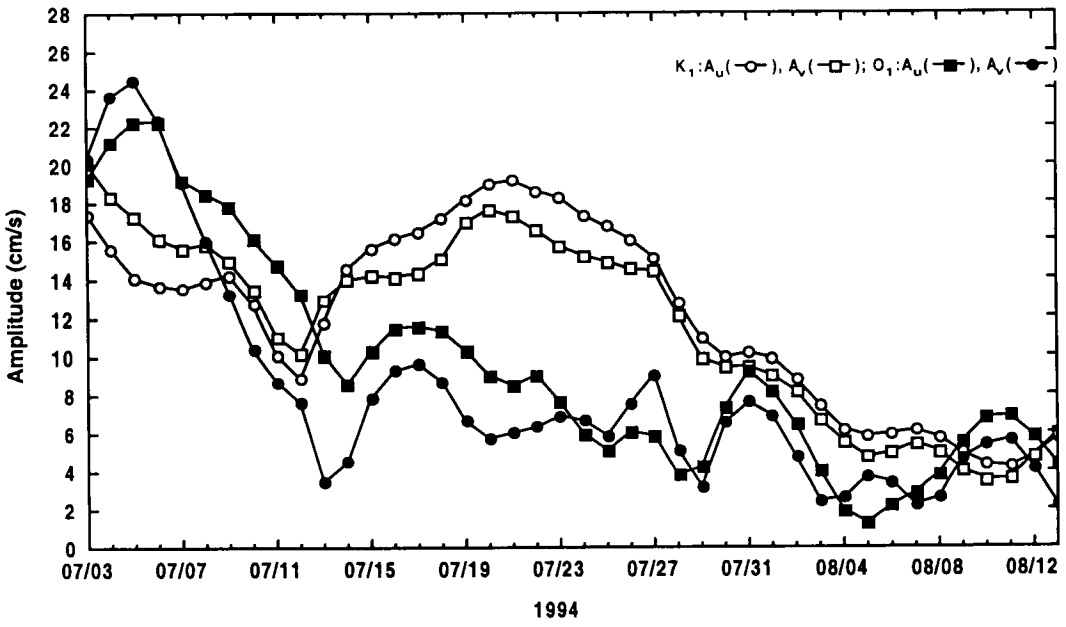

Figure I-10. Amplitudes of the K_1 and O_1 tidal currents obtained from the 15-day overlapping subsets for the upper current meter at mooring M2 (time displayed on the horizontal axis should be considered as the first day of each subset).

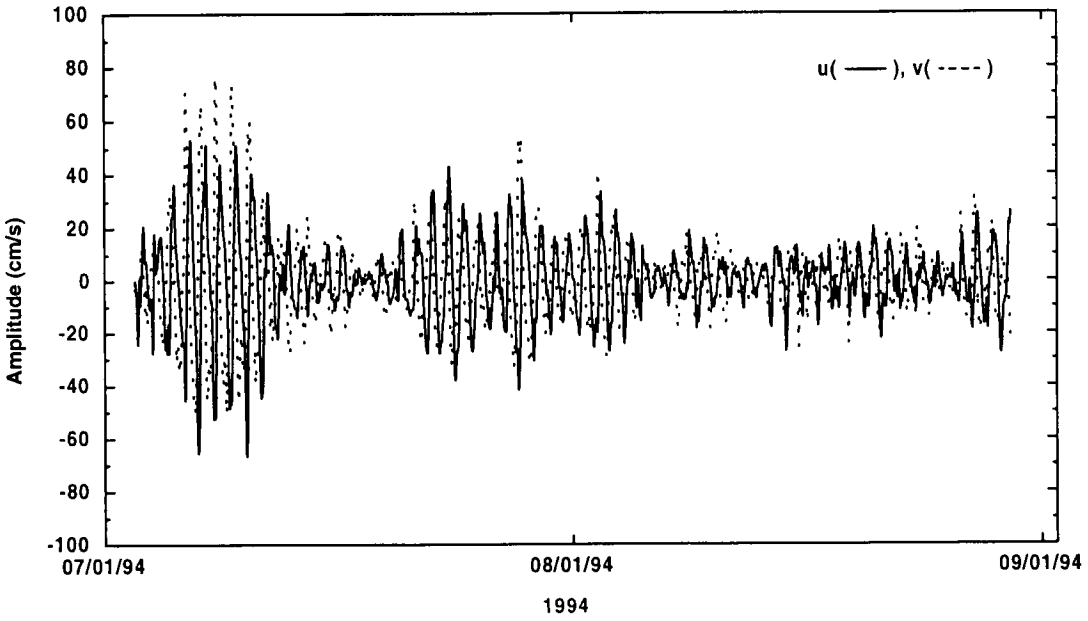

Figure I-11. The 3-40 hour band pass east-west (u) and north-south (v) velocity components of currents at the upper meter of mooring M2.

M4 were averaged, and then the average data were subjected to harmonic analysis (S.P. Murray and W.J. Wiseman Jr., personal communication, 1997). M3 mooring was excluded from the calculations because of the lack of data from the lower meter. Table I-4 summarizes the results. The estimation error of the principal axis size (Godin, 1972) varies from one location to another: it is 0.49 cm/s for mooring M1 and 0.66 cm/s and 0.65 cm/s for M2 and M4, respectively. Values of the semi-diurnal tidal major and minor axes are generally comparable to those determined earlier for each instrument separately. The M_2 tidal currents dominate among the semi-diurnal constituents, and they become stronger in the western portion of the study area as observed earlier. The M_2, S_2 and N_2 currents rotate clockwise, except for the M_2 and S_2 constituents at mooring M2 that have a counterclockwise rotation.

The K_1 and O_1 currents are again the largest in the diurnal frequency band. The extremely high values of their axis lengths have decreased significantly, and now they are similar to those found from the data of the LATEX A project (LATEX A report, 1997; DiMarco and Reid,1098). The O_1 currents dominate at moorings M1 and M2. The major and minor axes are 5.12 cm/s and 3.07 cm/s for M1 and 5.56 cm/s and 3.47 cm/s for M2. The K_1 current is the largest at the M4 mooring. Its major and minor axes are 5.31 cm/s and 1.84 cm/s, respectively. The sense of rotation of the diurnal currents is clockwise, except for the O_1 constituent at the M4 mooring location that rotates counterclockwise.

To find the net tidal forcing present in the study area during the LOCCOSUM project, the average tidal currents previously estimated for each constituent separately

were combined and a root mean squared (RMS) amplitude was estimated for the east-west and north-south components at the M1, M2, and M4 mooring sites. Results again confirmed that the tidal currents in the study area were weak. Values of the east-west RMS amplitudes varied a little from one location to another, and they were 3.95 cm/s at M1, 4.03 cm/s at M2, and 2.55 at M4. The north-south RMS amplitude was equal to 2.4 cm/s at M1, 2.5 cm/s and 3.86 cm/s at the M2 and M4 mooring sites, respectively.

Table I-4

Semi-major axis, semi-minor axis, semi-major axis direction and sense of rotation (CW=clockwise, CCW=anticlockwise) of tidal currents for M_2, S_2, N_2, K_1, O_1 and Q_1.

Mooring Number	Semi-major Axis (cm/s)	Semi-minor Axis (cm/s)	Major Axis Angle (°)	Rotation Sense
M_2				
M1	1.23	0.35	61.85	CCW
M2	2.09	0.73	-23.84	CW
M4	3.60	0.62	32.71	CW
S_2				
M1	0.4	0.06	-24.75	CCW
M2	1.02	0.31	-14.02	CW
M4	1.06	0.36	-39.43	CW
N_2				
M1	0.88	0.31	-19.88	CW
M2	1.27	0.78	-21.43	CW
M4	2.15	0.01	43.37	CW
K_1				
M1	3.42	0.82	-1.55	CW
M2	3.05	1.41	-11.71	CW
M4	5.31	1.84	7.74	CW
O_1				
M1	5.12	3.07	-70.23	CW
M2	5.56	3.47	-5.18	CW
M4	2.48	0.18	-17.99	CCW
Q_1				
M1	2.78	1.82	-2.87	CW
M2	0.91	0.11	28.62	CW
M4	1.90	0.29	-29.05	CW

3. Near Inertial Motion

3.1. Complex Demodulation of Observed Currents

The existence of another high frequency motion mode, near inertial oscillations, on the Louisiana-Texas shelf is well known and has been investigated by several researchers (Daddio et al., 1978; Chen et al., 1996). Unlike the tidal currents that are

predictable, the near inertial oscillations are non-deterministic signals. Despite their randomness, they are usually strong enough to be isolated from the tidal motion and background noise, especially when the inertial period is significantly different from the major tidal constituent periods and long data records of the current velocity components are available.

The inertial periods at the mooring sites of the study area are listed in Table I-5. They range from 24.81 hours to 25.11 hours. As has been mentioned in the previous chapter, these periods are slightly different from the periods of the diurnal tides (K_1 and O_1) that generate the strongest tidal currents on the shelf. This closeness of the periods may complicate analysis and separation of these different motions in the study area. However, knowing that the barotropic diurnal tidal currents are rather small and the near inertial oscillations are usually characterized by large amplitudes (Daddio et al., 1978; Chen et al., 1996), these oscillations still can be isolated from the tidal flow.

During the fifty eight-day observation interval, several days of large amplitude oscillatory motion were recorded by current meters. The east-west (u) and north-south (v) velocity components of the upper and lower meters at four mooring sites (see Figure I-1 for locations) are displayed in Figures I-12(a-d) and I-13(a-d), respectively. To exclude tidal influence, at least partially, the earlier estimated average barotropic tidal currents were subtracted from the raw velocity measurements. Then the residual components were band passed (20-28 hours) in order to decrease the impact of the higher or lower frequency motions on the amplitudes of the near inertial oscillations.

Table I-5

Inertial periods of the mooring sites on the Louisiana-Texas shelf south of Isles Dernieres.

Mooring Number	Inertial Period (hours)
M1	24.81
M2	25.11
M3	25.01
M4	24.89

According to the data of the current velocity components from the upper meters (Figure I-12), the most pronounced event was present approximately from July 5 to July 12, 1994. The near inertial oscillations appeared almost simultaneously in three of four upper meters (M1, M2 and M3) of the LOCCOSUM project. Another major episode occurred generally on July 20 and lasted until August 4, 1994 and was recorded at the same upper instruments. However, the precise beginning and end of this event differed from one mooring location to another. There were two other episodes after August 4, 1994 but the probable near inertial oscillations of the smaller amplitude were generally observed at very different times only at M1 and M2 moorings. The last event occurred at the end of the deployment starting approximately at the same time at M2, M3 and M4 and was only partly recorded. The oscillations reported by the lower instruments (Figure I-13) display different behavior at different sites. Based on salinity measurements and the

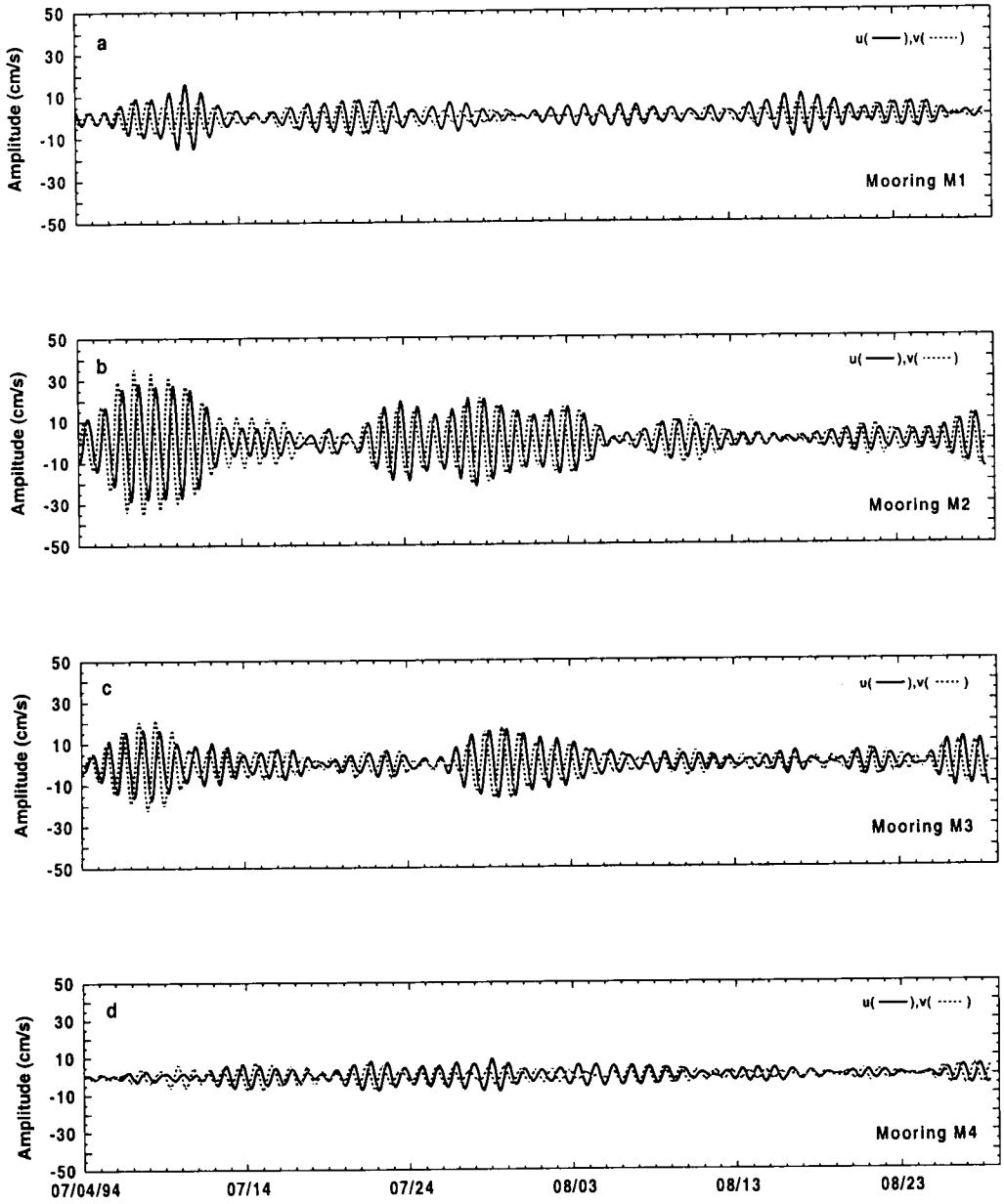

Figure I-12. Time series of the east-west (u) and north-south (v) components of the 20-28 h band pass residual currents from upper meters at (a) M1, (b) M2, (c) M3, and (d) M4 mooring sites.

repeat section study data, these meters were situated just below the halocline and may be considered as representative of the lower layer. In the case of a two-layer system the near inertial oscillations in the lower layer are not generated by the downward flux of the inertial energy from the upper layer, but they appear as a result of long internal near inertial waves propagating offshore. In such a case, these upper and lower layer oscillations are out of phase (Millot and Crepon, 1981). Our data suggest that this may be a reasonable explanation for observations the M1 and M2 moorings. Figure I-14 shows

that during the first episode the east-west component of the upper and lower meters at M2 are clearly out of phase (about 180°). Identical behavior was observed for the north-south components at M2 and both components at the M1 site for the first and second events. Additionally, amplitudes are smaller in the lower meters.

The results from the M4 mooring located on the western end of the study area are totally different from M1 and M2. The amplitudes of both velocity components observed at the lower meter are generally higher than those in the upper layer. Lack of amplitudes in the upper layer suggests that there was no inertial motion at this location. The larger amplitudes of the current components in the lower layer are difficult to explain. They might have been increased by internal tides or by propagating offshore long internal waves generated by the inertial oscillations observed in the eastern part of the study area.

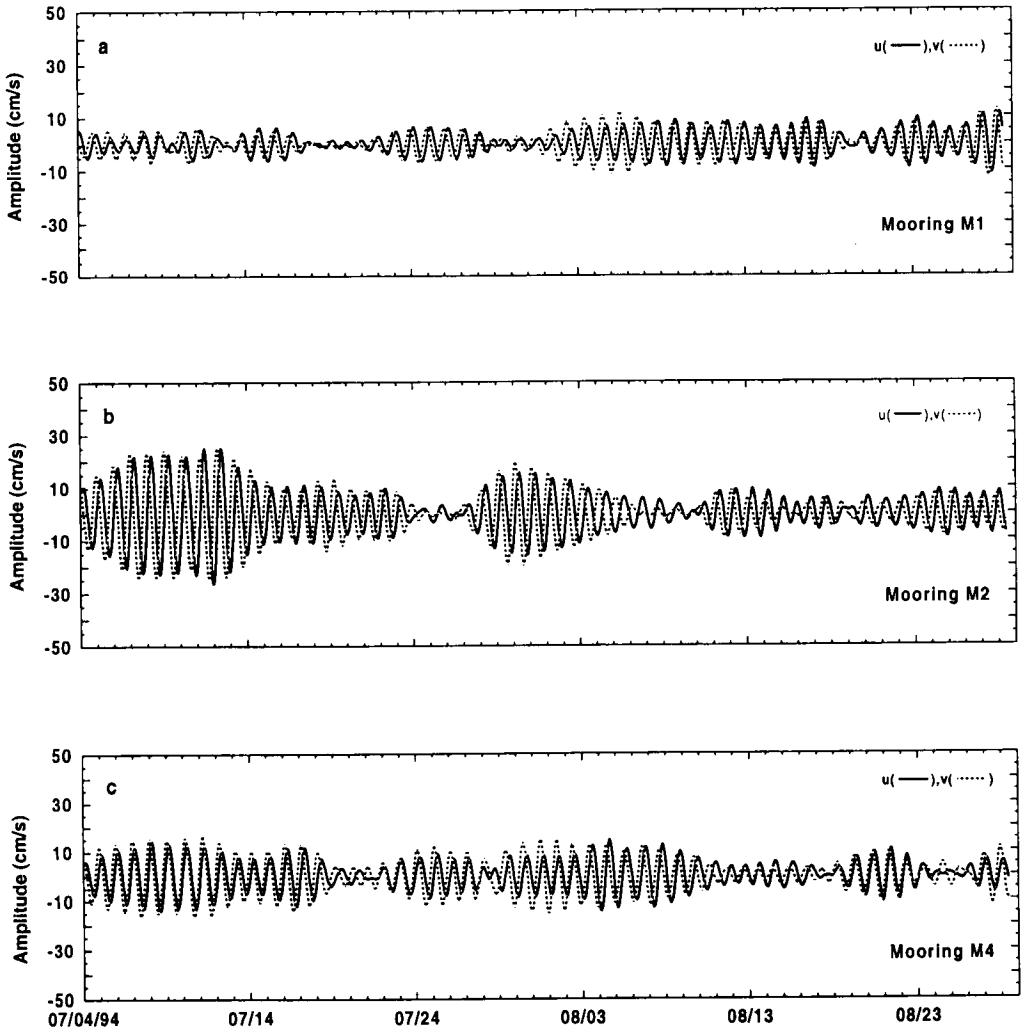

Figure I-13. Time series of the east-west (u) and north-south (v) components of the 20-28 h band pass residual currents from lower meters at (a) M1, (b) M2, and (c) M4 mooring sites.

To verify the existence of the near inertial oscillations at three moorings (M1, M2 and M3) complex demodulation was performed (Bloomfield, 1976). The complex demodulation may be regarded as a local version of harmonic analysis. It transforms a signal at frequency ω, which may be concealed by large contributions from other frequencies, to a demodulated signal having much reduced frequency. Similar to harmonic analysis, it describes the signal in terms of its magnitude and phase. It is local in the sense that these parameters are determined only by the data in the neighborhood of a particular time, t, rather than for the entire record. In this study, the time t is chosen to be equal to two inertial periods. Therefore, the magnitude and phase are computed as a function of only those currents observed over the time $t \pm 1$ inertial period and are independent of all other observed currents velocities.

Results obtained from the method described above are shown in Figure I-15(a-b). The demodulated signals from the upper meters at moorings M2 and M3 clearly show significant magnitudes associated with the first two episodes described earlier (Figure I-15a). Furthermore, these peaks are generally accompanied by a nearly constant phase as expected for inertial oscillations (Figure I-15b). Small magnitude episodes observed at all instruments after August 4, 1994 are very close to the amplitudes of the tidal currents and are probably tidal in origin. Since the inertial and tidal periods are so close, tidal currents unfortunately also are preserved in the demodulated signals with little change in magnitude (Daddio et al., 1977).

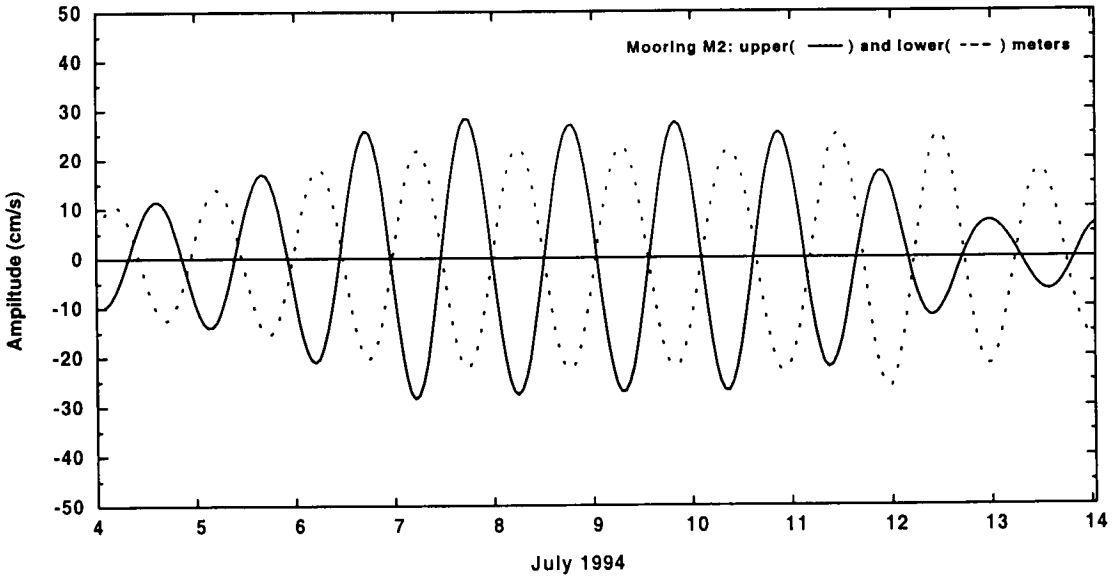

Figure I-14. Time series of the east-west (u) component of the 20-28 h band pass residual currents from the upper and lower meters at M2 mooring site.

The magnitudes (not shown) of the demodulated currents for the lower meter at M2 are 24 cm/s for the first event and 17 cm/s for the second event. The phase varies very slowly and generally might be considered constant. The magnitude (not shown) of the signal at the lower instrument at the M1 site does not exceed 6 cm/s for either episode

and might be generated by the tidal currents. However, the constant phase associated with these periods of time may suggest that they are inertial in origin.

In summary, the time series analyses and complex demodulation results confirm that near inertial oscillations were present on the inner shelf. The two largest and most clearly resolved oscillations were observed in early July and between July 20 and August 4, 1994. The magnitude of these oscillations decreased with depth (for example, the upper and lower meters at M2 site) and onshore (the upper meters at M2, M3 and M1 moorings). Such a downward and onshore decrease of the oscillation amplitudes was also reported by Chen et al. (1996). Finally, the oscillations in both layers were clearly out of phase. Such behavior suggests that the lower layer oscillations were generated by long near inertial internal waves, which are generated in the transient phase of the geostrophic adjustment at the shore in a two layer system and propagate offshore after the near inertial oscillations have been initiated at the surface layer (Millot and Crepon, 1981).

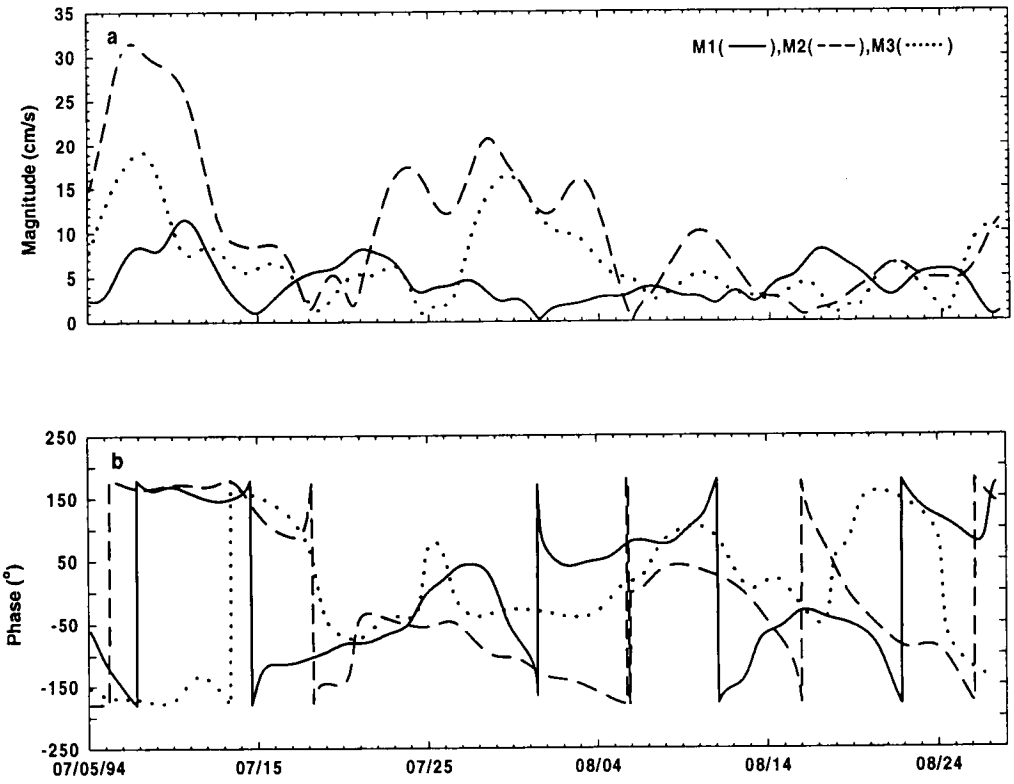

Figure I-15. Magnitudes (a) and phases (b) of the demodulated currents recorded by upper meters at M1, M2 and M3 mooring sites.

3.2. Relation of Near Inertial Oscillations to Wind Forcing

Inspection of time series and spectrum of the wind measured at Buoy 19 and Grand Isle and surface intensification of the near inertial oscillations may imply that the recorded near inertial motion in the upper layer is generated by wind. According to the

wind measurements from the buoy, the first episode was associated with the wind speed increase (from 2 m/s to 7 m/s) recorded on July 4, 1994. The same data showed that the second event was initiated by clockwise rotating wind and later maintained by winds shifting from southwesterly to northeasterly.

To test the hypothesis that the observed near inertial oscillations in the upper layer were generated by wind, a model developed by Pollard and Millard (1970) was utilized. This model assumes that the currents in a homogeneous mixed layer are generated by wind stress, which is instantaneously and uniformly distributed through this layer. The model currents are computed using the vertically averaged, linearized equations of motion:

$$\frac{\partial u}{\partial t} - fv = \frac{\tau_x}{\rho h} - cu \qquad (I-2)$$

$$\frac{\partial v}{\partial t} + fu = \frac{\tau_y}{\rho h} - cv \qquad (I-3)$$

where $\vec{\tau} = (\tau_x, \tau_y)$ is the wind stress, ρ is the water density, h is the mixed layer depth, f is a Coriolis parameter, u and v are the east-west and north-south velocity components of the model currents, and c^{-1} is the *e*-folding decay time that models the dispersion effect by introducing a decay factor of the form exp(-ct). The wind stresses are computed from

$$\vec{\tau} = c_D \rho_a \left|\vec{v}\right| \vec{v} \qquad (I-4)$$

where $\vec{v}$ is the hourly wind velocity; the density of the air is taken as $\rho_a = 1.22 * 10^{-3}$ g/cm^3, and $c_D = 1.2 * 10^{-3}$. There is a wide range of values for c_D and for summer winds observed along the Louisiana-Texas coast, this value of c_D seems to be appropriate as suggested by Hsu (1988), and it was also used for modeling of the inertial oscillations by Kundu (1976b). Assuming zero initial conditions (I-2) and (I-3) equations are integrated forward in time using a backward scheme for decay terms, a trapezoid scheme for the oscillatory terms and a time step of one hour, yielding time series for the east-west and north-south components.

When the wind from Buoy 19 was used as input with the decay time of 1.6 days the results were in fairly good agreement with the currents observed in the upper layer at the M2 and M3 mooring sites. The model also gave a good simulation of the currents observed at the M1 site in early July, when the wind from Grand Isle was used. Figure I-16(a-b) shows the modeled and observed velocity components for the M2 location. It can be seen clearly that the wind was able to initiate the near inertial oscillations found in the upper layer. The time of appearance of the modeled inertial currents is well correlated with the time when these currents were actually present. However, there is an apparent phase difference between modeled and observed currents. This time lag is, first of all, introduced by the numerical scheme used for the oscillatory terms and is equal to 4.2 hours for the inertial period of the M2 site and the one-hour time step. It may also result from the fact that the input wind, which was used in the model, was not measured at the same location or in the close vicinity of the mooring (the distance between the mooring

and buoy is about 120 km). There is also the third possibility that long near inertial internal waves may have contributed to the phase difference. The amplitudes generated by wind are also comparable with those of the observed oscillations, except for a discrepancy that was found after July 29, 1994. That may result from the last two reasons that are used to explain the phase difference.

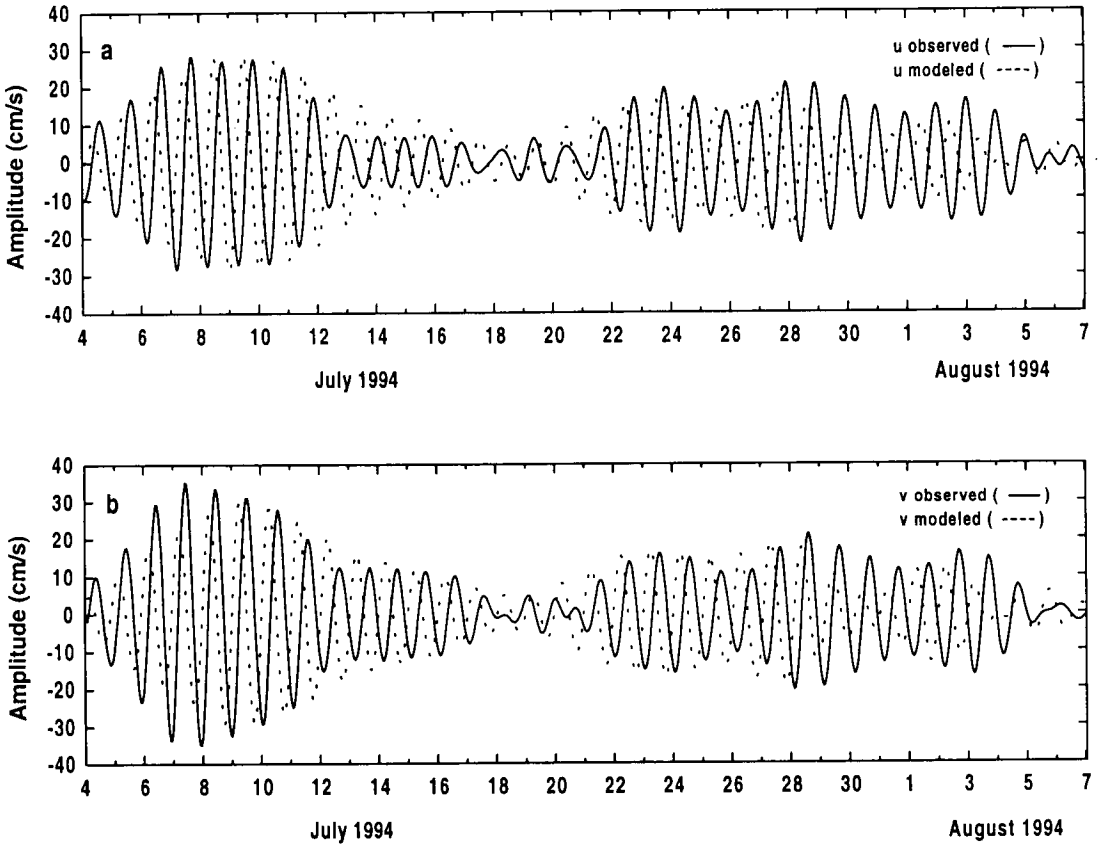

Figure I-16. East-west (a) and north-south (b) velocity components of the modeled and observed inertial oscillations at M2 location (east and north are positive; west and south are negative).

4. Low Frequency Motion

4.1. Monthly Flow Field from Current Meters

It has been shown that the low frequency flow on the seasonal time scale on the Louisiana-Texas inner shelf has two different flow regimes: upcoast flow usually from June to August and downcoast flow during the rest of the year. According to the monthly average of the LATEX A current measurements, the upcoast flow regime was observed only in June and July 1994 and then in August 1994, a weak downcoast flow began (Murray et al., 1997). The low frequency currents obtained from the current meter data from this project seem to confirm their different behavior in July and August 1994.

The monthly average of the low frequency current east-west (u) and north-south (v) components are given in Table I-6 and displayed in Figure I-17(a-b). Additionally, the table and figures include information about the mean flow computed for the LATEX A instruments (see Figure I-1 for locations). In addition to the monthly average, the table contains standard deviations and root mean square errors for each component determined separately from the hourly data for the July and August subsets. The error of the monthly average was calculated as (Kundu and Allen, 1976):

$$\varepsilon = \sigma(T/2L)^{-1/2} \qquad (I-5)$$

where ε is the error of the mean estimates, σ the standard deviation of the signal, T the length of the time series, and L is the integral scale defined as half of the area under the autocorrelation function.

Table I-6

Mean, standard deviation and root mean square error for M1, M2, M3, M4, LA 14, LA15, and LA16 mooring sites.

Mooring Number	Instrument Depth (m)	u_{mean} (cm/s)	σ_u (cm/s)	ε_u (cm/s)	v_{mean} (cm/s)	σ_v (cm/s)	ε_v (cm/s)
July 3 – July 31 1994							
M1	5.46	5.29	9.8	4.07	2.15	5.93	1.12
	10	0.04	5.49	2.39	-1.79	3.44	0.68
M2	5.46	2.33	13.25	5.14	-0.44	9.16	2.69
	10	3.83	9.97	4.87	-0.82	8.34	3.24
M3	5.46	22.57	11.36	5.61	-0.61	6.42	1.98
M4	5.46	16.73	9.17	2.12	-9.34	7.52	1.54
	10	6.79	11.08	4.42	-4.03	5.24	1.61
LA14	9	5.05	8.24	4.07	-0.39	5.80	1.49
LA15	10	14.08	9.29	2.64	2.33	8.09	2.48
LA16	9	-3.90	4.68	0.89	-1.96	2.77	0.50
August 1 – August 29 1994							
M1	5.46	-2.59	9.21	3.64	-0.84	4.67	0.87
	10	-2.96	10.81	4.02	-4.27	6.03	1.81
M2	5.46	-3.84	11.57	6.41	4.11	11.00	3.52
	10	-3.52	12.03	6.13	-0.82	6.17	2.07
M3	5.46	-3.19	15.03	6.54	0.73	9.93	4.95
M4	5.46	-3.34	10.63	4.77	-0.98	6.41	1.95
	10	-3.43	12.93	4.99	-1.91	7.13	1.15
LA14	9	-0.82	9.43	4.63	-1.31	9.67	3.19
LA15	10	-1.39	10.66	3.75	-0.48	7.25	1.95
LA16	9	-4.51	8.74	2.79	-1.78	3.91	1.27

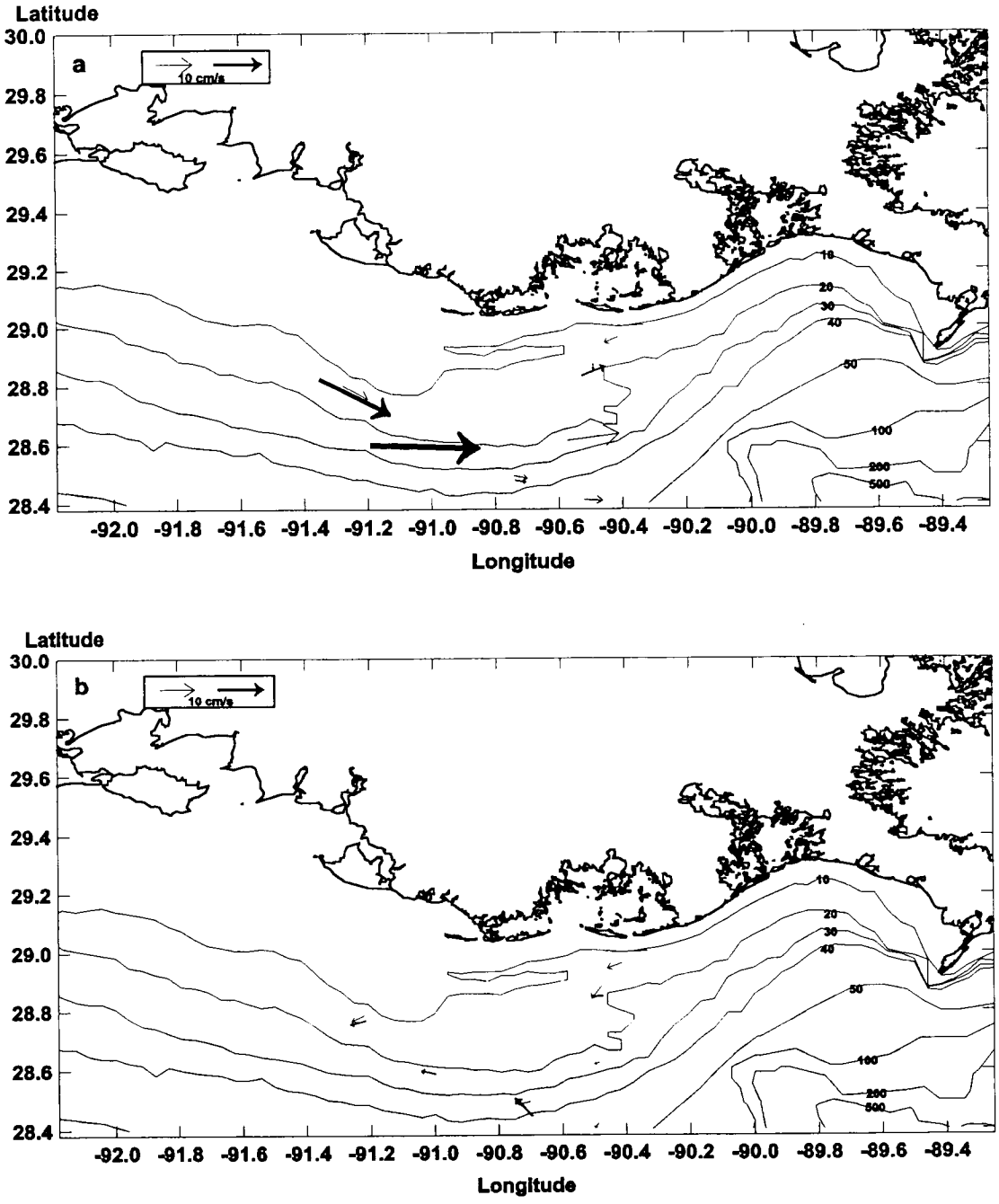

Figure I-17. Monthly average current vectors during (a) July 1994; (b) August 1994 (thick arrows – upper meters, thin arrows – lower meters).

The July averages of the east-west components show eastward flow for all upper and lower level instruments, except at the LA16 site (Figure I-17a). The mean flow speeds generally decrease with depth, except at M2; however, neither mean is statistically different from 0 at M2 mooring. Therefore, it is rather difficult to say whether such a decrease of the mean flow speeds is present or not. The u_{mean} of the lower level

instrument at M1 is also much lower than its error and is not statistically meaningful. All moorings with a well-defined eastward flow are also characterized by much smaller means of the north-south components. Table I-6 shows that only half of the estimates of the mean of the north-south component are statistically significant.

The monthly averages of the east-west component for the August data set are totally different. All instruments have rather weak westward flow. Contrary to the July means, August means are smaller than the errors and should be rather considered non-significant, except for that at mooring LA16. The means of the north-south component are southward, except for that of the upper meter at M2, and most are also statistically insignificant. In summary, the August flow field (Figure I-17b) seems to be less organized than that observed for the July subset.

A common property for both subsets is large standard deviations. They are generally much greater than the estimated monthly averages, with an exception at the locations where the strong eastward flow is dominant. Such large deviations indicate the presence of a strong fluctuation field during July and August 1994. The standard deviations generally decrease with depth for the first subset and in the onshore direction for both subsets. Another interesting feature, which emerges from this analysis, is the decorrelation time of the components. The root mean square error depends on this time. Examination of the error values show that they are always larger for the east-west component than those of the north-south component. Therefore, it may be deduced that the decorrelation time of the u component is larger than that of the v component. It ranges from 2 to 3 days and from 5 to 10 days for the north-south and east-west component, respectively, if calculated for the entire data record.

In summary, the July estimates show rather a good example of the summer upcoast flow that seemed to be confined by the 30-meter isobath. Farther offshore the eastward flow was still present, however, the currents were much weaker. This horizontal decrease of the flow speed suggests the existence of a different low frequency motion farther out on the shelf. In August, the mean flow was not well defined and probably represented a transition period between the upcoast and downcoast regimes of the Louisiana-Texas coastal current.

4.2. Spatial Correlations

To determine how the currents in the study area are spatially related, the cross-correlation coefficients of the east-west (u) and north-south (v) components as a function of the distance of separation were calculated for current meters at depths of 9 and 10 m. For the purpose of this analysis, it was assumed that the low frequency currents for instruments measured one meter apart in the vertical, were similar. Two different spatial correlation scales were determined: cross-shelf and along-shelf. Both scales were computed from the 40-hour band pass data for a period of time between July 3 and August 29, 1994.

The cross-shelf spatial scale of the east-west and north-south components was obtained for the meters at LA16, M1, LA15 and LA14 mooring sites. The standard error of the correlation coefficients was 0.3 for the east-west current component and 0.2 for the north-south component. The results are displayed in Table I-7 and Figure I-18. The table contains the 0 lag and maximum correlation coefficients for each pair of the instruments and the time lag when this maximum occurred. The results of this analysis show that all correlation coefficients are much larger than the error, but it can also be seen that they are rather small and do not exceed 0.6. The cross-shelf correlation scales approximated by the 0-lag coefficients for both components decrease with increasing separations of the mooring sites. The correlation of the north-south component, however, seems to decline faster than that of the east-west component (Figure I-18). Thus, the cross-shelf correlation scale of the east-west component is longer than that of the north-south component.

The along-shelf correlation scale of the velocity components was estimated using current records from M1, M2, M4, LA14, LA15 and LA16 mooring sites for the same period of time as the previously computed cross-shelf spatial scale. Unfortunately, the number of current mooring pairs is even smaller than that used for the cross-shelf spatial correlation scale, so the results are less reliable (Table I-8, Figure I-19). However, they give some insight on what the along-shelf scale might be. It can be seen that the along-shelf correlation of the east-west component is the highest for the separations less than 30 km and it stays fairly large even for large mooring separations. This may suggest that the scale of the east-west component is much higher in the along-shelf direction than that of the cross-shore one. The same scale of the north-south component is negative and small for all mooring pairs and distances. Such behavior may imply that similar to the cross-shelf spatial scale, the along-shelf scale of this component is very small and probably does not exceed a few kilometers.

Table I-7

Correlation coefficients of the east-west (u) and north-south (v) velocity components as a function of cross-shelf separation.

Mooring Sites	Distance (km)	0 Lag u Correlation	Maximum Lag		0 Lag v Correlation	Maximum Lag	
			U Correlation	Hours		v Correlation	Hours
M1 LA16	11.5	0.48	0.59	-18	0.56	0.56	0
M1 LA15	26.6	0.50	0.56	15	0.26	0.32	12
M1 LA14	50.0	0.20	0.46	140	-0.05	-0.28	170
LA16 LA15	37.1	0.13	0.43	94	0.20	-0.33	157
LA16 LA14	60.5	0.18	0.33	98	0.16	-0.28	200
LA14 LA15	23.5	0.42	0.53	-85	0.34	0.34	0

Table I-8

Correlation coefficients of the east-west (u) and north-south (v) velocity components as a function of along-shelf separation.

Mooring Sites	Distance (km)	0 Lag u Correlation	Maximum Lag		0 Lag v Correlation	Maximum Lag	
			u Correlation	Hours		v Correlation	Hours
M4 LA16	82.0	0.26	0.44	37	-0.15	-0.38	-28
M4 M1	74.0	0.35	0.51	62	-0.27	-0.46	25
M2 LA14	24.0	0.76	0.76	0	-0.14	0.20	140
M2 LA15	27.0	0.64	0.64	0	-0.09	0.30	190

Table I-9

Magnitude of complex correlation coefficients of the upper layer low frequency currents.

Mooring Sites	Total Depth (m)	Mooring Separation (km)	Magnitude
M4:M3	14.9:23.0	28.0	0.94
M4:M2	14.9:36.0	60.0	0.28
M4:M1	14.9:19.0	74.0	0.56
M3:M2	23.0:36.0	32.0	0.34
M3:M1	23.0:19.0	60.0	0.53
M2:M1	36.0:19.0	47.0	0.22

The July monthly averages of the currents show that the strong para-isobathic flow in the upper layer is generally shoreward of the 30-meter isobath. To determined whether this visual observation is valid or not the complex coefficient (Kundu, 1976a) was computed for the upper meter records at M1, M2, M3 and M4 mooring sites. This quantity is a complex number whose magnitude (<1) gives the overall measure of correlation between two current records. The coefficient was calculated for the July subset of the data only. Table I-9 shows the results from this analysis.

The magnitudes of the complex correlation coefficients are consistent with the previously stated hypothesis about probable presence of the different flow regimes separated by the 30-meter isobath over the inshore part of the study area and farther out on the shelf in July 1994. All mooring pairs (M1, M3, and M4) deployed at depth less then 30 meters are characterized by large magnitudes. It is also valid even for the large separation of the mooring sites. However, if the current record from the M2 location, where the total depth is 36 m, is included in the analysis, the value of the correlation coefficient decreases significantly regardless of the distance between the current meters.

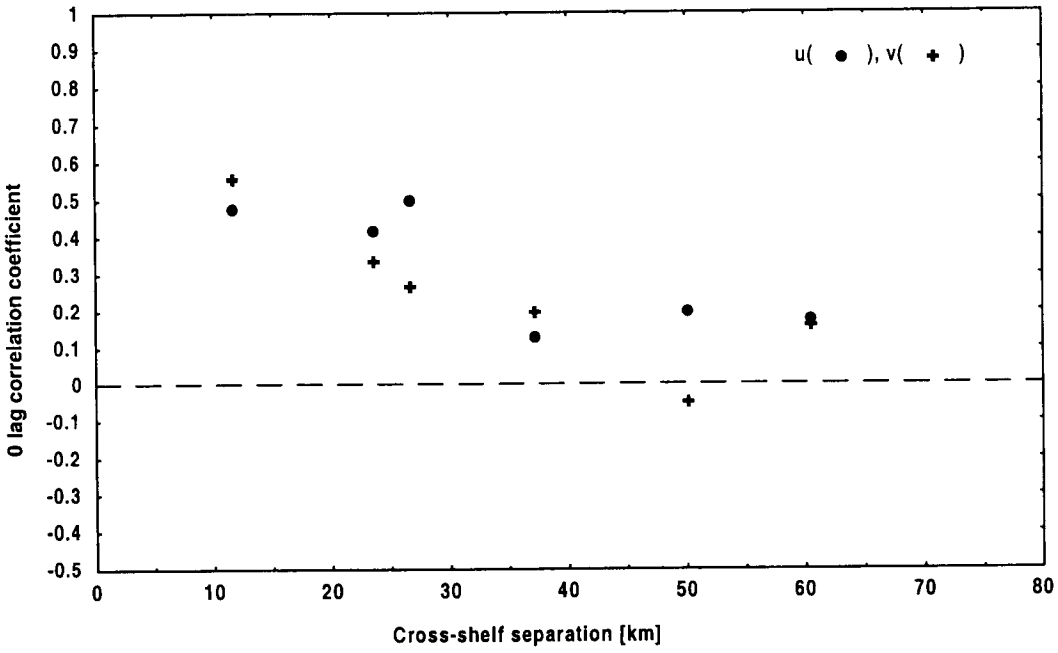

Figure I-18. Correlation coefficients of east-west (u) and north-south (v) current velocity components as a function of cross-shelf mooring separation.

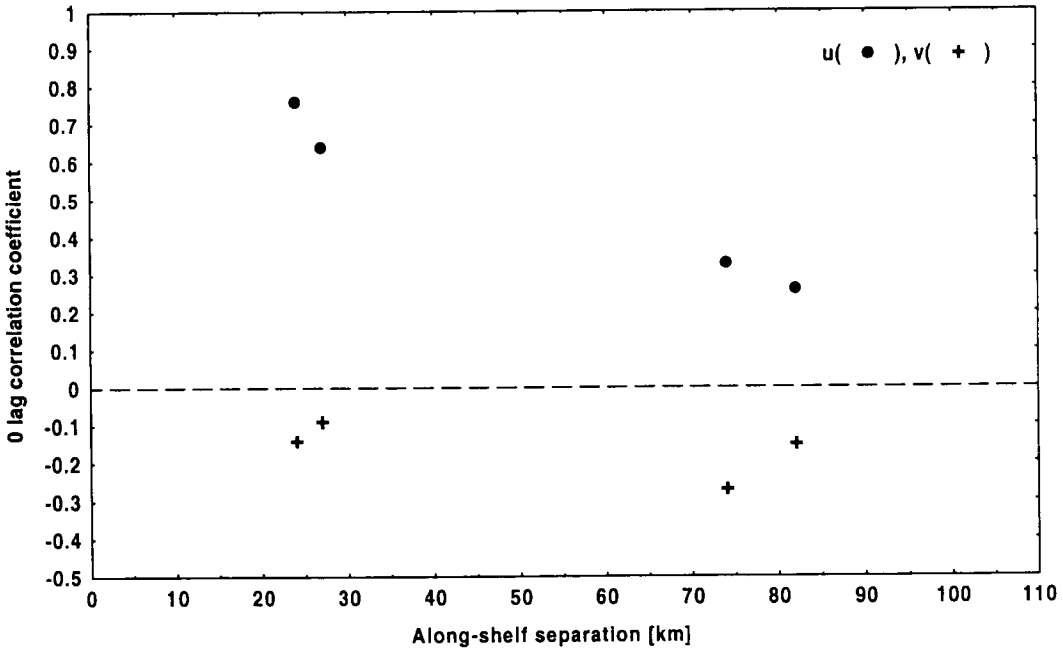

Figure I-19. Correlation coefficients of east-west (u) and north-south (v) current velocity components as a function of along-shelf mooring separation.

4.3. Spectral Analysis of the Low Frequency Flow

The energy spectra of both current components at all moorings did not show any significant peaks in the low frequency band. The energy generally increased with decreasing frequencies. A representative example of the averaged spectrum is displayed in Figure I-20. The raw spectra of the east-west (u) and north-south (v) components were computed for the upper meter at the M3 mooring for the entire available record. Then they were averaged over eight frequencies yielding to 16 degrees of freedom. The only significant peaks present in the spectrum of both components are associated with the inertial-diurnal and semi-diurnal bands. At subtidal frequencies (≤ 0.6 cpd) the energy increases almost linearly with decreasing frequency. Another feature, which is also common for all moorings, is that the energy computed for the east-west component is always higher than that of the north-south component for the low frequency band.

Assuming a linear relation between current components, the coherence squared was estimated. For 16 degrees of freedom, the coherence greater than 0.35 was significant at the 95% confidence level.

Results obtained for the east-west current component showed that the currents recorded in the upper layer at M1, M3, and M4 were coherent (coherence squared >0.5) for the frequencies less than 0.3 cpd. Surprisingly, the coherence squared was totally insignificant between M4-M2, M3-M2 and M1-M2 mooring pairs (coherence squared<0.35). Despite the proximity of the M2, M3, and M4 mooring sites, the east-west component did not show any coherence in any frequency band between these station pairs.

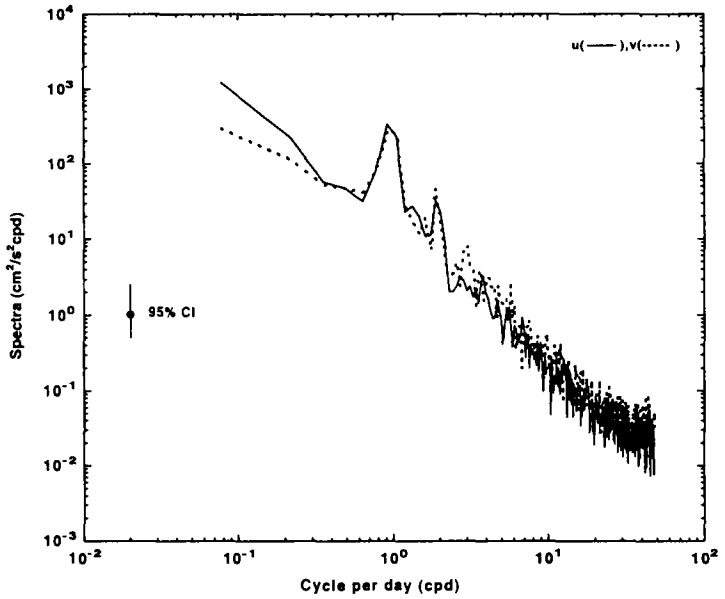

Figure I-20. Spectra of the east-west (u) and north-south (v) velocity current component for the upper meter at M4 mooring site.

The coherence squared of the upper layer north-south component showed that there was no significant dependence between the majority of mooring pairs at any frequency band, except for the M4-M2 and M3-M2 pairs. However, in both cases, the currents measured at one mooring could explain less than 50% of the variance of those at the second mooring for the very narrow frequency band centered at 0.5 cpd.

The coherence squared of the north-south component computed for the lower meters was not significant for any pair. The same quantity of the east-west components was significant for all pairs, but not for the entire low frequency band. The currents at M4 and M1 mooring sites were coherent at frequencies <0.3 cpd with the maximum coherence (0.67) at 0.2 cpd. The coherence squared between M1 and M2 was only significant for very low frequency (<0.22) and does not exceed 0.5. The last possible pair M4-M2 exhibited coherence at frequencies less than 0.5 cpd band and, on average, the coherence squared was equal to 0.45.

In the vertical, the best values of the coherence squared (>0.6) of the east-west component were found at the M4 mooring where the currents were highly coherent at all low frequencies (<0.58 cpd). At M2, the same component recorded at the upper and lower meters was coherent for the frequencies less than 0.3 cpd, but the coherence squared did not exceed 0.6. Similar results were obtained for the M1 mooring site where the currents were correlated for the same band. The values of the coherence squared for the north-south component were poorer than those of the east-west velocity component. At the M1 location, the upper currents could explain only about 50% of the variance of the lower currents at very low frequencies (<0.18 cpd). Similar results were observed at the M4 site; however, the frequency band was broader (0.1-0.3 cpd). At the M2 mooring, there was no correlation between the upper and lower current components throughout the entire low frequency band.

In summary, the coherence squared analysis gave similar results to those presented earlier in this chapter (spatial correlations). The east-west components consistently exhibited higher coherence than the north-south velocity components. The coherence squared of the north-south component was generally insignificant for the majority of the mooring pair combinations. The coherence of the east-west component was usually greater for the moorings with a short separation distance or when the moorings were located in waters with a total depth of less than 30 m.

4.4. Possible Driving Forces of Low Frequency Currents – Multiple and Partial Coherence

To determine which driving mechanisms control currents in the study area, multiple and partial coherences were estimated for both velocity components. Similar to the analysis described by Murray et al. (1997), the simple linear model with four inputs and one output was designed. The inputs were the possible driving forces and the output was one of the velocity components. The following forcing functions were chosen: (a) east-west pseudo wind stress; (b) north-south pseudo wind stress; (c) along-shelf barotropic pressure gradient approximated by water level differences; and, (d) buoyancy

forcing proxied by river discharge as in Münchow and Garvine (1993). The pseudo wind stress defined as

$$\vec{\tau}_p = |\vec{v}|\vec{v} \qquad (I-6)$$

where $\vec{v}$ is the wind velocity vector is directly proportional to wind stress (compare with equation I-4) and has the advantage of being independent of the choice of the drag coefficient. For the following statistical analyses, results are independent of whichever parameterization is used. The pseudo wind stresses were computed from the wind velocity components measured at Buoy 19. The water level differences were found for gauges at Grand Isle and Atchafalaya Bay near Eugene Island. The buoyancy forcing was represented by Atchfalaya River discharge.

Figure I-21 displays results obtained for the east-west components of the upper meters at all LOCCSUM mooring locations. The multiple coherence is statistically significant for all considered cases. It means that the four forcing variables together were important driving mechanisms of the east-west current component observed in July and August 1994. Percentage of the component variance explained by these driving forces depends on the frequency and mooring location, but it is at least 50% at M1, 45% at M2, 45% and 60% at M3 and M4, respectively.

Looking at the partial coherences, the east-west pseudo wind stress (Figure I-21a) was a dominant forcing mechanism for the currents at the M1 mooring (frequencies <0.25 cpd). Surprisingly, at M2, this wind stress components was unimportant for the entire low frequency band, and the buoyancy forcing seemed to be significant at the frequency band centered around 0.22 cpd (Figure I-21b). At M3 (Figure I-21c) and M4 (Figure I-21d), the east-west wind stress dominated for the frequencies less than 0.4 cpd. The north-south wind stress influenced current fluctuations in a narrow frequency band centered around 0.22 cpd in both locations. Finally, at M4, the alongshore pressure gradient and buoyancy forcing became important and statistically significant for the different frequencies (pressure gradient <0.4 cpd; buoyancy forcing <0.25 cpd).

Results (not shown) of the multiple coherence analysis of the east-west component for the lower instruments at the M1, M2 and M4 mooring sites gave similar results. For all these cases, the multiple coherence was statistically significant. However, how much variance of the component was explained by four inputs depended on the location. The highest values of multiple coherence were found at the M2 and M4 sites where, on average, the driving mechanisms accounted for at least 70% of the current variance. Such high values were only present at very low frequencies at M1. The rest of the band was characterized by the multiple coherence less than 0.6. From an investigation of the partial coherences, the north-south wind stress seemed to be dominant at M1 for the frequencies less than 0.25 cpd. Surprisingly, at the M2 mooring, buoyancy forcing played an important role as a forcing mechanism in the frequency range from 0.01 to 0.4 cpd. At the M4 site, the east-west wind stress appeared to be statistically important for the very low frequencies (<0.15 cpd).

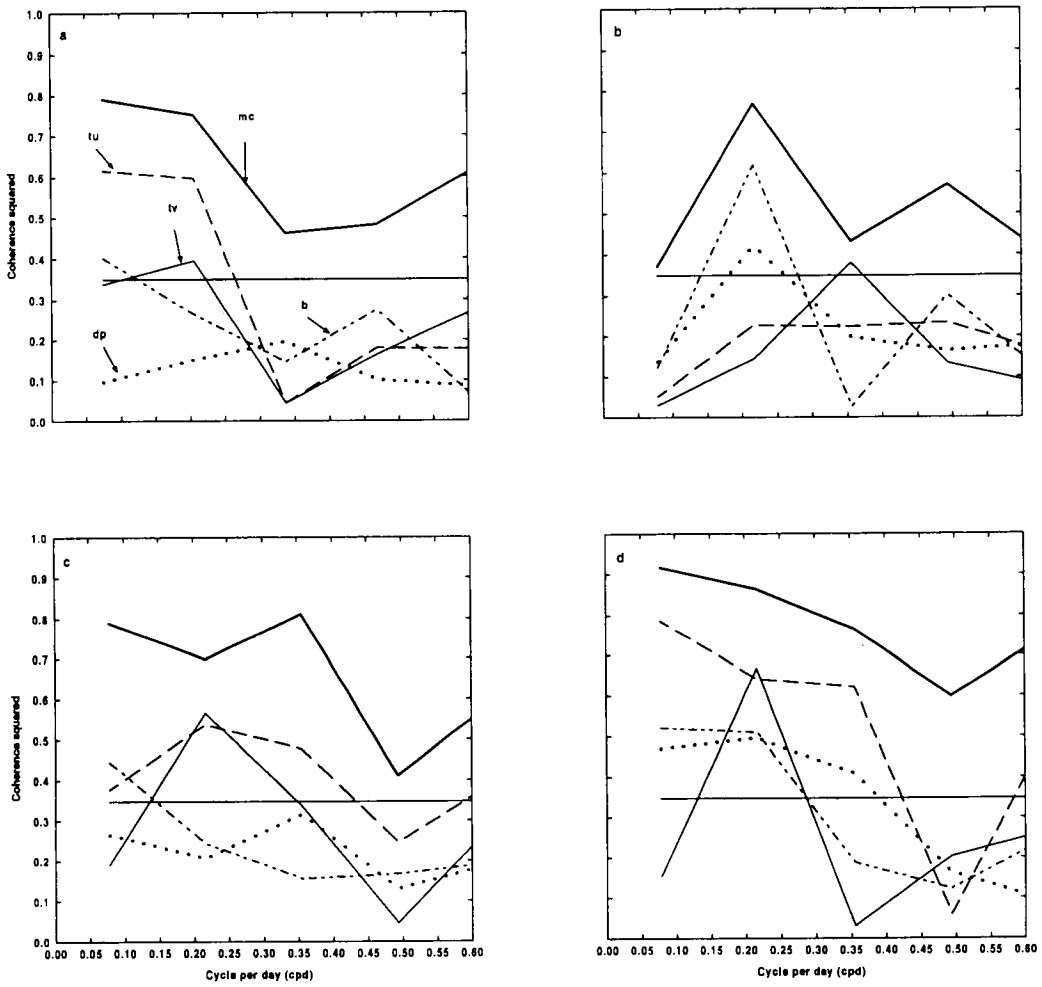

Figure I-21. Multiple coherence (mc) and partial coherences between the east-west velocity component of the upper meters with the east-west pseudo wind stress (tu), north-south pseudo wind stress (tv), along-shelf pressure gradient (dp) and buoyancy forcing (b) at (a) M1, (b) M2, (c) M3, and (d) M4 mooring locations (the lower straight solid line is the 95% significance level).

Multiple and partial coherences of the upper meter north-south current velocity components computed for all LOCCSUM locations are shown in Figure I-22. The multiple coherence was only statistically significant for the entire low frequency band at the M2 and M4 mooring sites. The driving forces could explain at least 60% of the component fluctuations at these locations. At M1 and M3, the multiple coherence dropped below the 95% confidence level for some frequencies (Figure I-22a,c). This means that the four forces were unimportant driving mechanisms of the north-south current

components in July and August 1994 for these frequencies at M1 and M3. Looking at the forces separately, the east-west wind stress seemed dominant at all mooring sites, but its influence varied with the location and frequency band. The most visible impact was observed at the M2 and M4.

For the lower meters, the highest values of multiple coherence (not shown) of the north-south current component were observed at the M1 and M4 mooring sites. At least 55% of the total variance of the current fluctuations was explained by the forcing variables at the first mooring where the dominant forcing seemed to be the east-west wind stress. At the M4 site, at least 60% of the current variance was accounted for by the forces. The partial coherences showed that different mechanisms were important at different frequencies, but the highest values are found for the north-south wind stress in the frequency band 0.2-0.4 cpd. At M2, the multiple coherence was statistically significant for all frequencies, except for a small range from 0.34 to 0.38 cpd. Both wind stresses components, especially the north-south one, separately seemed to have some influence on the current fluctuations at 0.22 cpd.

In summary, the multiple coherence analysis shows that four model variables together were important driving mechanisms for the low frequency flow in the study area in July and August 1994. The percentage of the total variance explained by them depends on flow component, frequency band considered and mooring location. The multiple coherence of the east-west component is statistically significant for all frequencies at all mooring locations. On average, at least 60% of the current fluctuations is accounted for by the driving forces for the majority of the analyzed cases. The partial coherences show that the east-west component is generally highly coherent with the pseudo wind stresses, especially with the east-west stress at the moorings located in waters with a total depth of less than 30 m. However, the influence of this force is different for different locations and frequencies. Surprisingly, farther offshore (M2 site), the east-west component is well correlated with the buoyancy forcing for some frequencies. For the north-south component, four driving mechanisms explain between 50 to 80% of the total variance for the frequencies less than 0.3 cpd. The principle forcing mechanisms for this component are also the wind stresses. However, the significance of these forces depends again on the frequency and location considered.

D. Summary and Conclusions

The purpose of this report was to describe the summer flow regime observed on the portion of the Louisiana-Texas shelf located south of Isle Dernieres, just east of the injection of the Atchafalaya River waters into the eastward flowing Louisiana-Texas coastal current. A description of this regime was based on a data set from the LOCCOSUM project, which was particularly designed to examine variability of the current field and hydrography. The data obtained from CTD and ADCP instruments were used to describe daily changes in salinity and the flow field along four sections. Next, high frequency motions, e.g. barotropic tidal currents and near inertial oscillations, were

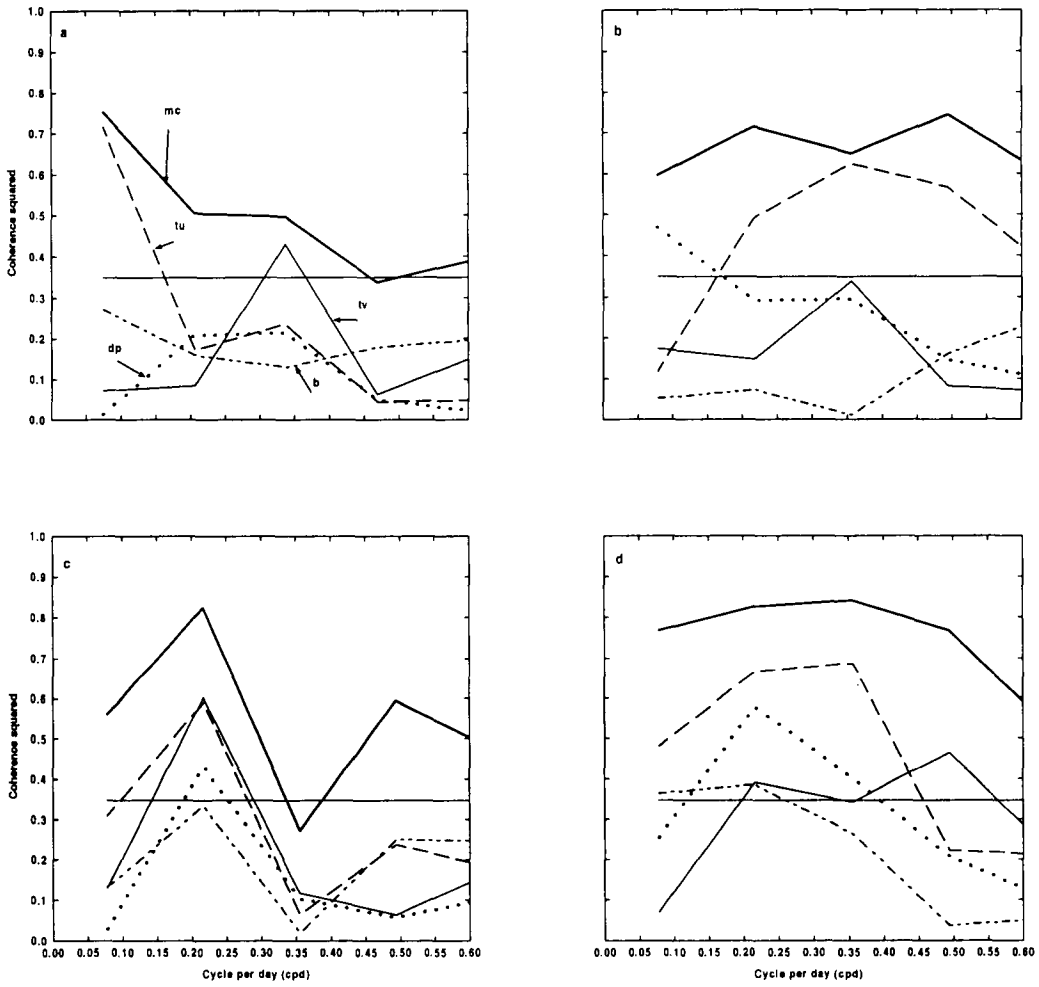

Figure I-22. Multiple coherence (mc) and partial coherences between the north-south velocity component of the upper meters with the east-west pseudo wind stress (tu), north-south pseudo wind stress (tv), along-shelf pressure gradient (dp) and buoyancy forcing (b) at (a) M1, (b) M2, (c) M3, and (d) M4 mooring locations (the lower straight solid line is the 95%significance level).

examined in the study area. Finally, the low frequency circulation and its possible driving forces were described.

Day to day changes in the hydrography (salinity) and the flow field in the study area were examined around a box, which was sampled three times. Each pass took roughly a day. This study shows that salinity distribution was characterized by a three-layer structure: (1) the upper layer filled with low salinity waters (~22 psu); (2) the halocline layer; (3) the lower layer with high salinity waters (~34 psu). This structure was observed along all sections and this pattern was maintained through all three passes. A few modifications of this basic salinity distribution, e.g. downward movement of the

halocline and onshore movement of the low salinity water lens (~20 psu) along the S1 section, were associated with the end of an upwelling episode observed along this line.

The flow field exhibited more changes than the salinity distribution from one pass to another. These modifications were more distinct in the shallowest part of the study area (total depth less than 10 m) where the flow was generally driven by wind and responded quickly to any variations in wind speed and direction. Offshore of this shallow region, in general, the upcoast flow, which decelerated with time, was present in the upper part of the water column. This flow was probably set up by southwesterly winds blowing prior to the cruise and may have represented a well-developed phase of the Louisiana-Texas coastal current in its summer flow regime. The southwesterly winds ceased just before the repeat section study (RSS) began, and the modifications of the upcoast flow observed during the RSS seemed to be associated with the changing wind field and salinity (density) structure (e.g. relaxation after the upwelling episode). Aliasing, originating from the presence of high frequency motion, such as near inertial and tidal oscillations, may have been also responsible for these apparent changes. However, current records from LA14 and LA15 mooring locations did not show any near inertial motion before and during the RSS in the study area, at least in its eastern part, and tidal analysis show that the barotropic tidal currents are small over this part of the shelf. Therefore, the observed modifications of the flow were associated with the wind and salinity changes.

In order to examine current fluctuations at longer tidal scales in the same region, four moorings were deployed along three sides of the box. Data from these moorings indicate that the average barotropic tidal currents are small in the study area. Among eight computed constituents (M_2, N_2, S_2, K_1, O_1 and Q_1), the diurnal tidal currents (K_1 and O_1) are dominant. These diurnal tidal currents generally rotate clockwise. Values of their major and minor axes vary from one place to another. The K_1 and O_1 major axes do not exceed 5.6 cm/s for all mooring locations. The minor axis values of the K_1 and O_1 constituents are even smaller than those of their major axes, and the difference between them is approximately 2 cm/s at all examined mooring sites. The net tidal forcing, which originates from the eight estimated constituents, is also small and similar at all moorings: RMS values of both (east-west and north-south) tidal velocity components are smaller than 4.5 cm/s.

Another high frequency motion, near inertial oscillations, was observed at three of four mooring places (M1, M2 and M3). Since the moorings were located fairly close to each other, the lack of these oscillations at M4 suggests that the spatial correlation scale of this motion might be small. Results from the model proposed by Pollard and Millard (1970) are consistent with the oscillations observed in the upper layer being initiated by moderate winds present over the shelf in July and August 1994. Comparison of the east-west and north-south components of the near inertial currents showed that both components measured by the meters in the upper and lower layers were clearly out of phase (~180°). Such behavior suggested that the near inertial oscillations in the lower layer were created by long internal near inertial waves. These waves are generated at the shore in a two-layer system, which was present in July and August 1994 in the study area, and propagate offshore after the near inertial oscillations have been initiated in the upper

layer (Millot and Crepon, 1981). Magnitudes of the observed oscillations decreased with depth and in the onshore direction. The maximum magnitudes were found at the southernmost upper meter (M2 mooring), and they were approximately 30 cm/s and 20 cm/s for the first and second episodes, respectively.

The low frequency flow recorded at four mooring sites exhibited several interesting features. The behavior of this flow was different in July and August 1994. In July, the upcoast flow dominated, and in August, the low frequency currents were less organized and probably represented a transient period between the upcoast and downcoast flow regimes of the Louisiana-Texas coastal current. The spatial correlation scale of this flow depended on the current component and was anisotropic. This scale seemed to be larger for the alongshore direction than that for the cross-shore direction, and it was much longer for the alongshore current component than that of the cross-shore current component. The small number of the moorings did not allow estimating the exact length of the spatial correlation scales; however, the character of the alongshore flow seemed to change significantly at the 30-meter isobath in the cross-shore direction over this part of the shelf. Finally, fluctuations of this flow were fairly well explained by four forcing mechanisms: alongshore and cross-shore wind stresses, alongshore pressure gradient, and buoyancy forcing, among which the alongshore wind stress was a dominant driving force. Its impact on the currents decreased, as expected, with increasing depth. Murray et al. (1997) report that in summer, the primary forcing of the Louisiana-Texas coastal current on the Louisiana shelf is the alongshore pressure gradient. This conclusion was based on data from the summer of 1992. In this year, the LTCC flowed upcoast in June, July and August. In 1994, such a flow was observed in July. Lack of data from June 1994 and the different flow pattern in August 1994 probably account for different results.

A three-day repeat section study and sixty days of current meter records have provided more detailed look at the summer hydrography and current characteristics. However, several questions still need to be answered. For example, what causes the counter current observed during the RSS on this portion of the shelf, and whether this current is a permanent or transient feature. Despite the earlier studies, it is still not clear what forcing mechanisms drive the coastal current in the summer season, and how far this current extends in both vertical and horizontal directions. Therefore, further studies and data are required to improve our knowledge about this current since this low frequency flow is a major agent responsible for distribution of pollutants, nutrients, and sediment in the region.

PART II

TRANSPORT OF THE LTCC

A. Introduction

Initial estimates of transport in the Louisiana-Texas coastal current (LTCC) were made in the LATEX B study (Murray et al., 1997) by averaging underway ADCP-derived transport data from shore-normal lines. Given the available data, this approach yielded a broad temporal and spatial average extending over five to eight days and hundreds of kilometers.

The approach here was to remove spatial and temporal aliasing on the transport values by constructing and maintaining a transport-resolving array of current meters across the LTCC at a suitable location. Figure II-1 is a location map of the Louisiana-Texas shelf showing the locations off Cameron, Louisiana, of (a) the transport resolving array; (b) pressure and water level gauges; and, (c) anemometer locations used in the analysis of the transport data. The Cameron location for the transport array was selected based on two considerations: (a) first, to be far enough downstream of the Atchafalaya River mouth to escape its influence and the influence of the large Tiger and Trinity shoals on the flow field; and (b) for any mooring in the water column on the inner Louisiana shelf to survive oil industry traffic and fishing pressure, it must be located near an existing oil field structure to deter trawling and general boat traffic. Availability of nearby platforms or stand pipes thus also played a key role in the mooring location. Despite our caution and coordination with oil structure owners, we lost several moorings and pressure gauges during the study when structures were removed with our mooring lines and gauges attached.

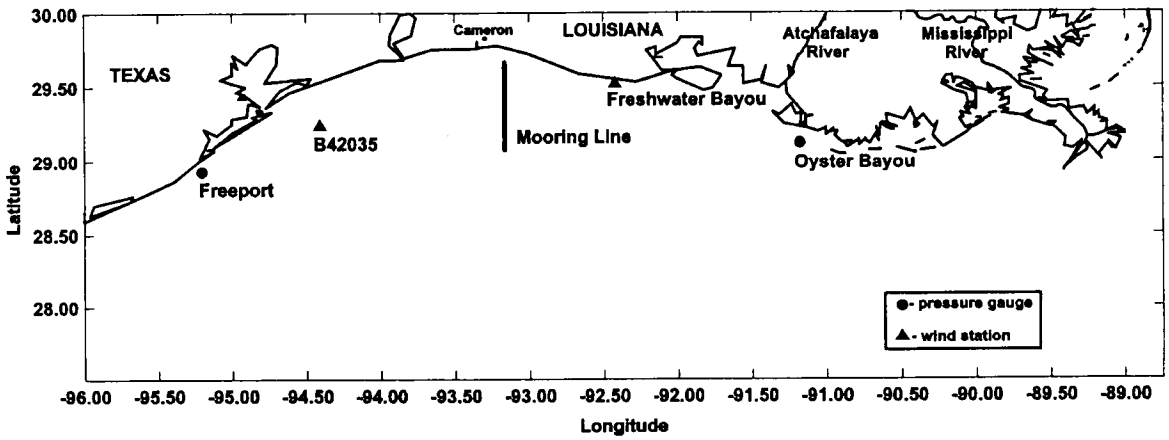

Figure II-1. Regional map containing study transect (mooring line) of LTCC south of Cameron, LA. Data from our shallow pressure gauges at Oyster Bayou and Freeport, and wind data from our station at Freshwater Bayou and the US buoy off Galveston (B42035) are used in analysis.

Figure II-2 shows the location of seven moorings on the cross-shore monitoring line labeled A through G from offshore to onshore. This line is seven km east of the sampling line S5 (along 93° 15' W) that was repeated on all five coastal plume cruises of the LATEX B program (Murray et al., 1997). Table II-1 gives the location and water depth at each mooring along with instrument depth and serial number of the current meters, all Endeco 174 impeller models. Note the mooring line extends in a cross-shore direction over 65 km, from about the 22-m isobath inshore to the 10-m isobath over a fairly uniformly sloping bottom.

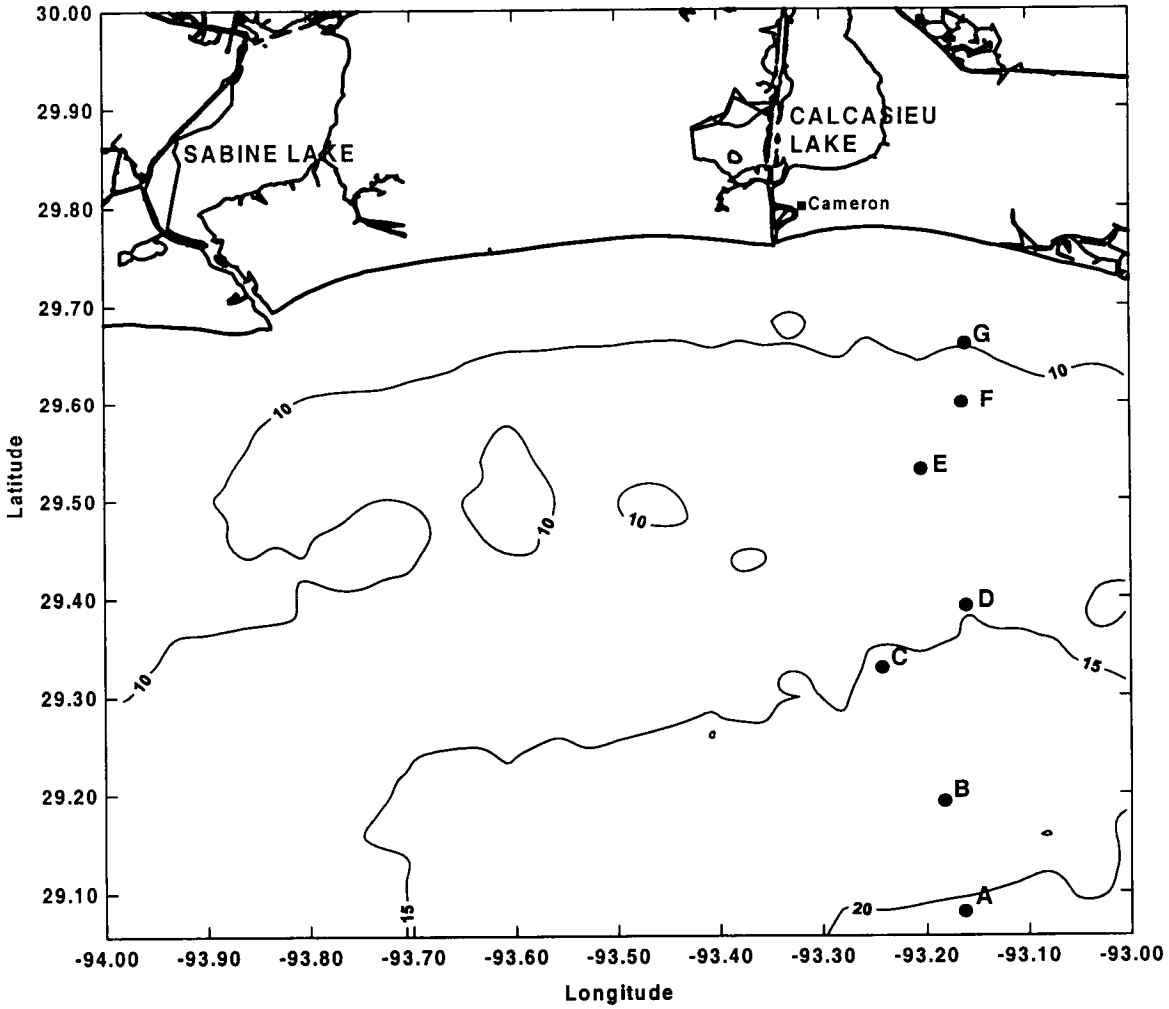

Figure II-2. Detailed map of bathymetry along mooring line (depths in meters). Survival demands mooring lines be located near oil well structures to deter trawler damage.

The mooring design is shown in Figure II-3 (see also Table II-1 for details). The shallowest mooring G carried only one current meter, while moorings F, E, D, and B carried two; the mid-section mooring C and outermost mooring A carried three. Additionally, four SeaCats recording salinity and temperature were deployed across the array, one each at the five-to-six-meter level on moorings A, F, and D, and one deep SeaCat at the 12-m level on mooring D. The SeaCats were intended to determine the

Table II-1

Mooring names, location, total depth, and instrument configurations.

Mooring	Mooring Name	Longitude	Latitude	Total Depth [m]	Instrument	Instrument Depth [m]
A	Annabella	93.16277W	29.08033N	23.1	SeaCat	5.8
A	Annabella	93.16277W	29.08033N	23.1	Current meter	7.8
A	Annabella	93.16277W	29.08033N	23.1	Current meter	13.3
B	Brigitte	93.18233W	29.19233N	19.5	Current meter	5.5
B	Brigitte	93.18233W	29.19233N	19.5	Current meter	10.0
C	Cathy	93.24219W	29.3289N	17.7	Current meter	6.4
C	Cathy	93.24219W	29.3289N	17.7	Current meter	11.0
C	Cathy	93.24219W	29.3289N	17.7	Current meter	15.0
D	Debra	93.243W	29.39167N	15.0	SeaCat	4.5
D	Debra	93.243W	29.39167N	15.0	Current meter	5.5
D	Debra	93.243W	29.39167N	15.0	SeaCat	12.5
E	Eudora	93.20417W	29.53033N	13.1	Current meter	5.7
E	Eudora	93.20417W	29.53033N	13.1	Current meter	10.0
F	Fiona	93.16433W	29.59967N	12.0	SeaCat	5.0
F	Fiona	93.16433W	29.59967N	12.0	Current meter	6.5
F	Fiona	93.16433W	29.59967N	12.0	Current meter	10.0
G	Greta	93.16084W	29.66033N	10.0	Current meter	5.5

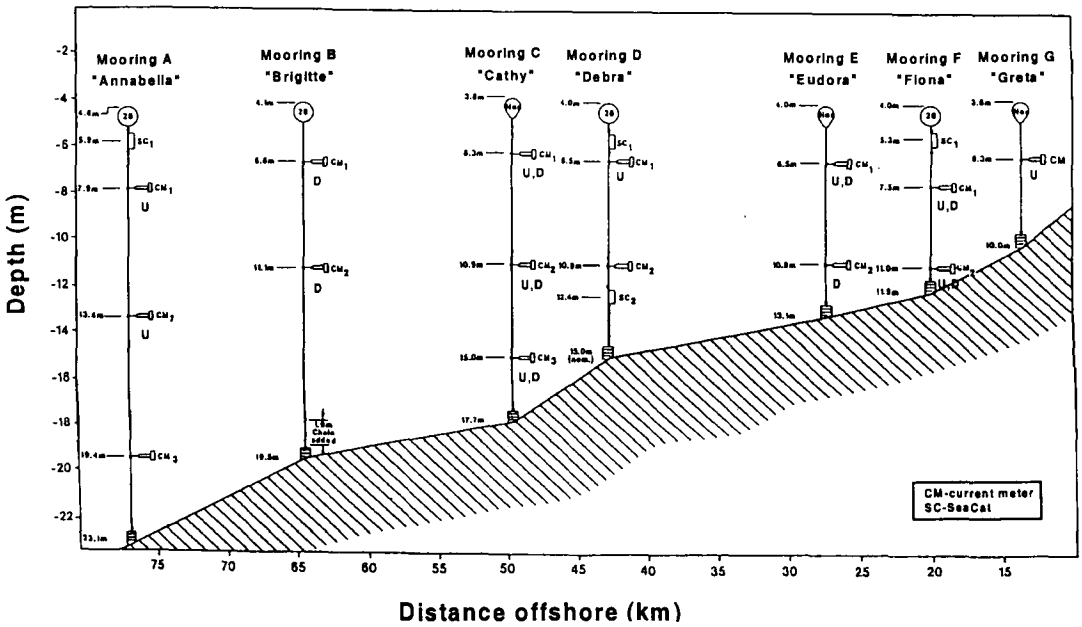

Figure II-3. Details of instrumentation along the mooring line (D indicates instruments whose data were analyzed for the downcoast regime and U indicates instruments whose data were analyzed for the upcoast regime).

reduced salinity characteristic of coastal plume waters through the duration of the development.

A data inventory is presented in Figure II-4 for the 15 current meters and the 4 SeaCats. Logistical difficulty from equipment malfunctions and severe weather limited the data return in 1995. Mooring operations were resumed using improved equipment in May 1996, with greatly improved data returns. Figure II-4 shows that the period of good data coverage extended from the beginning of May 1996 to the end of January 1997. This conveniently allowed for the study of the two distinct flow regimes: the upcoast summer flow regime of 1996 and the downcoast winter flow regime of 1996-97. The labels U and D adjacent to each current meter in Figure II-3 indicate which instruments were used in the summer and winter regime studies, respectively.

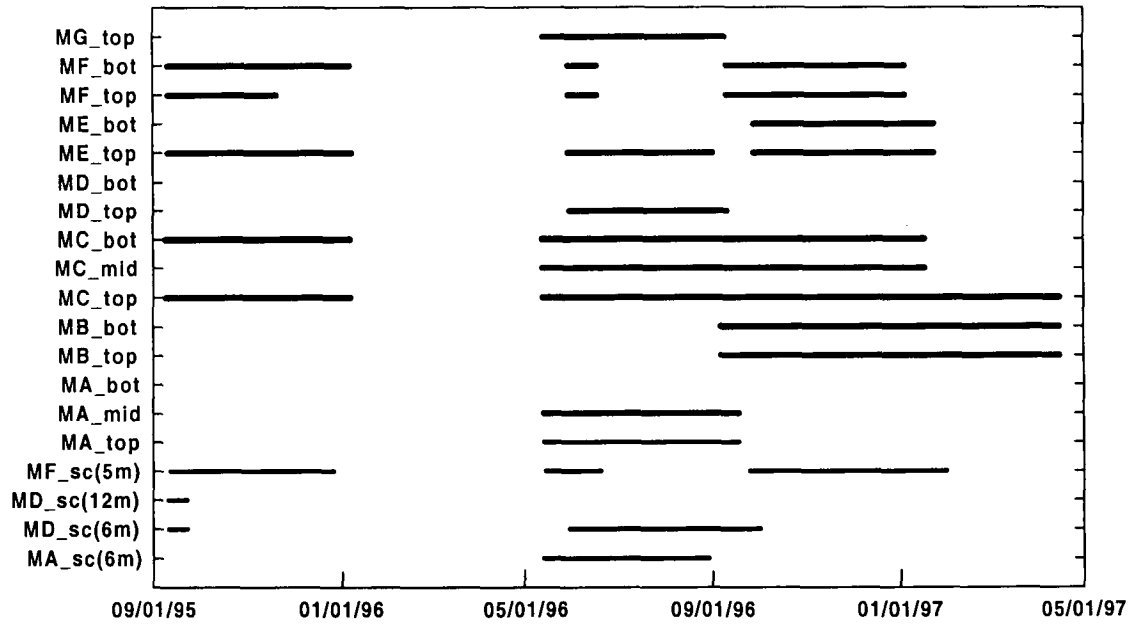

Figure II-4. Data log of current meters and SeaCat sensors (where, for instance, MA means mooring A, top (mid/bot) means a top (middle/bottom) current meter instrument, and sc(5m) means a SeaCat instrument at depth 5 meters).

B. Characteristics of Data

The data fundamental to this study are the velocity vectors obtained from the moored current meters. The Endeco 174 was set for nominal 10 minute samples. The standard stored data is hourly vector averages, which are displayed in Figure II-5 as an example for the period November 10-30, 1996, from the three levels of mooring C. Moderate to strong events are commonly coherent through the water column as in November 22 and November 27. A strong westward current pulse as expected for this time of year occurs November 15-17. Diurnal oscillations, either tidal or inertial, are evident throughout the record (e.g., November 24-25). The temporal variability over a

several hour time scale as a result of tidal, inertial and atmospheric forcing can be clearly significant.

The example of summer regime current data in Figure II-6 (July 10-30, 1996) shows similar strong daily variability. Eastward events can be seen July 13-15 and July 20-24. This visual inspection of the hourly unfiltered data suggests that the eastward summer regime is present but highly intermittent in nature. Thus, we will use 40-hour low pass data to remove the ubiquitous tidal and inertial oscillations from our transport computations.

In Figures II-7 and II-8 we show the corresponding wind records from the Galveston Buoy 42035 (only for the summer period) and the anemometer at Freshwater Bayou. These two stations are separated by a distance of about 200 km. The Freshwater Bayou station is 78 km and the Galveston Buoy is 119 km away from a mid-point of the Cameron transect.

The November winds (Figure II-7) during the downcoast flow regime are generally strong with speeds frequently 10 m/s or more and variable in their direction. The first part of the record (11-17 of November) shows a period of persistent easterly winds with speeds up to 12-13 m/s. Beginning on the 20 of November, the winds are characterized by speeds between 3 and 12 m/s and a clockwise rotation. Note that there is high visual coherence between the currents at mooring C (Figure II-5) and the winds observed in November.

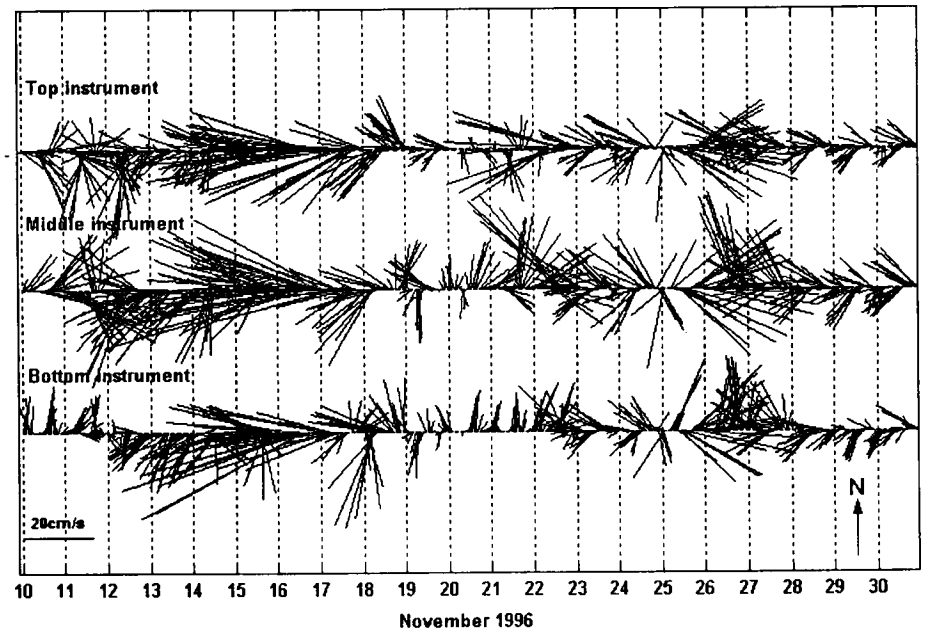

Figur II-5. Example of hourly current vectors from the meters on three levels of mooring C during winter downcoast flow from November 10-30, 1996.

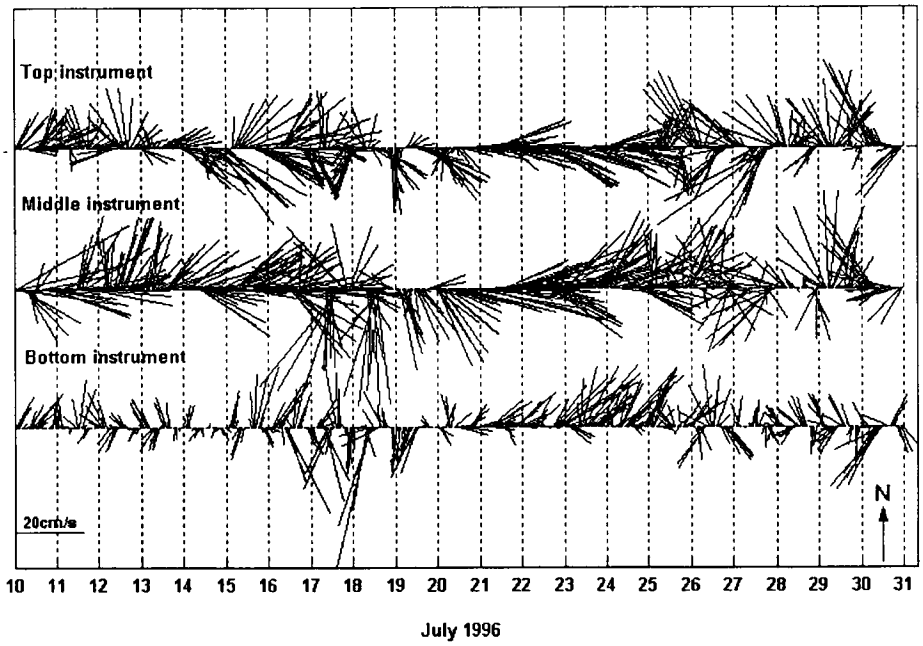

Figure II-6. Example of hourly current vectors from the meters on three levels of mooring C during summer upcoast flow from July 10-30, 1996.

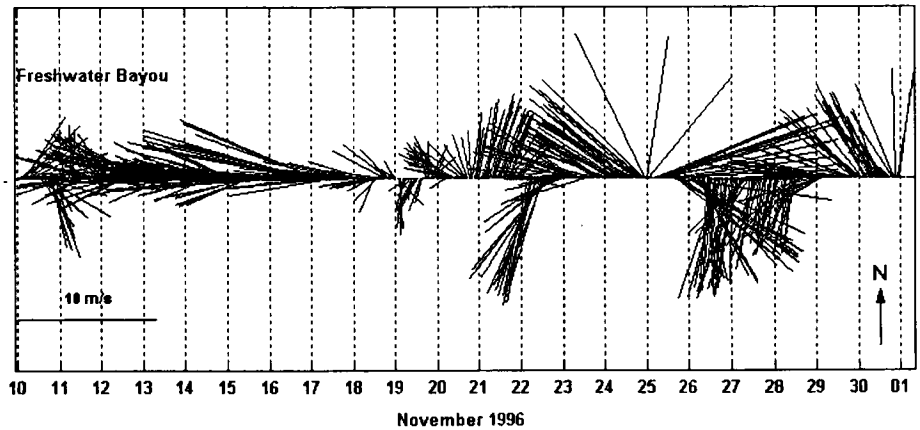

Figure II-7. Example of hourly wind vectors from Freshwater Bayou for the winter period November 10-30, 1996.

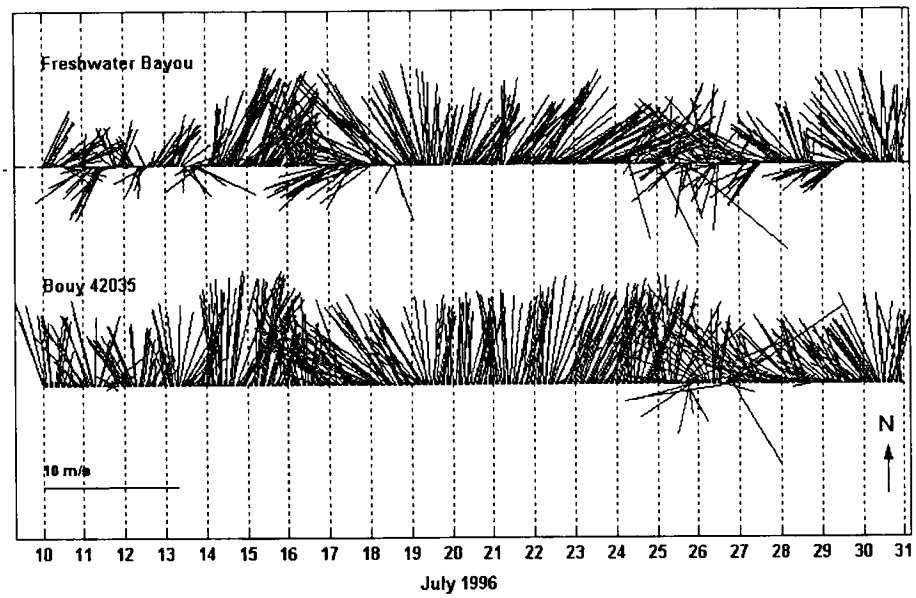

Figure II-8. Example of wind data from Freshwater Bayou and B42035 for the summer period July 10-30, 1996.

During July 1996, winds are 5-7 m/s and blow quite steadily onshore along the Louisiana coastline as expected. However, there is surprisingly little visual coherence between the highly variable currents at mooring C (Figure II-8) and the winds (Figure II-8).

Spectral analysis (Mooers, 1973) of the observed winds at Freshwater Bayou and Buoy 42035 shows (Figure II-9a and Figure II-10a) that in the winter season, a major part of their energy is associated with the low frequencies (<0.6 cpd) for both clockwise and anticlockwise components. Both components are characterized by a small peak present in the frequency band between 0.1 and 0.5 cpd. The winds in both stations are in phase and are highly coherent with the coherence squared (not shown) varying from 0.6 to 0.9 and from 0.7 to 0.95 for the anticlockwise and clockwise spectral components, respectively. In summer, the low frequency part of the spectrum is rather 'red' but again contains majority of the wind energy (Figure II-9b and Figure II-10b). The coherence (not shown) between the winds at Galveston Buoy and Freshwater Bayou is smaller than that observed in the winter season, and becomes even statistically not different from zero for the anticlockwise component at frequencies higher than 0.4 cpd. Similar to the winter period, the summer phase between the winds at these two stations is almost zero, except for frequencies higher than 0.4 cpd.

In addition to the wind driving, we may expect influence of the Atchafalaya River discharge on the low frequency currents of the LTCC. Figure II-11 shows the Atchafalaya River discharge at Simmsport 1995-1997. Note that the time periods

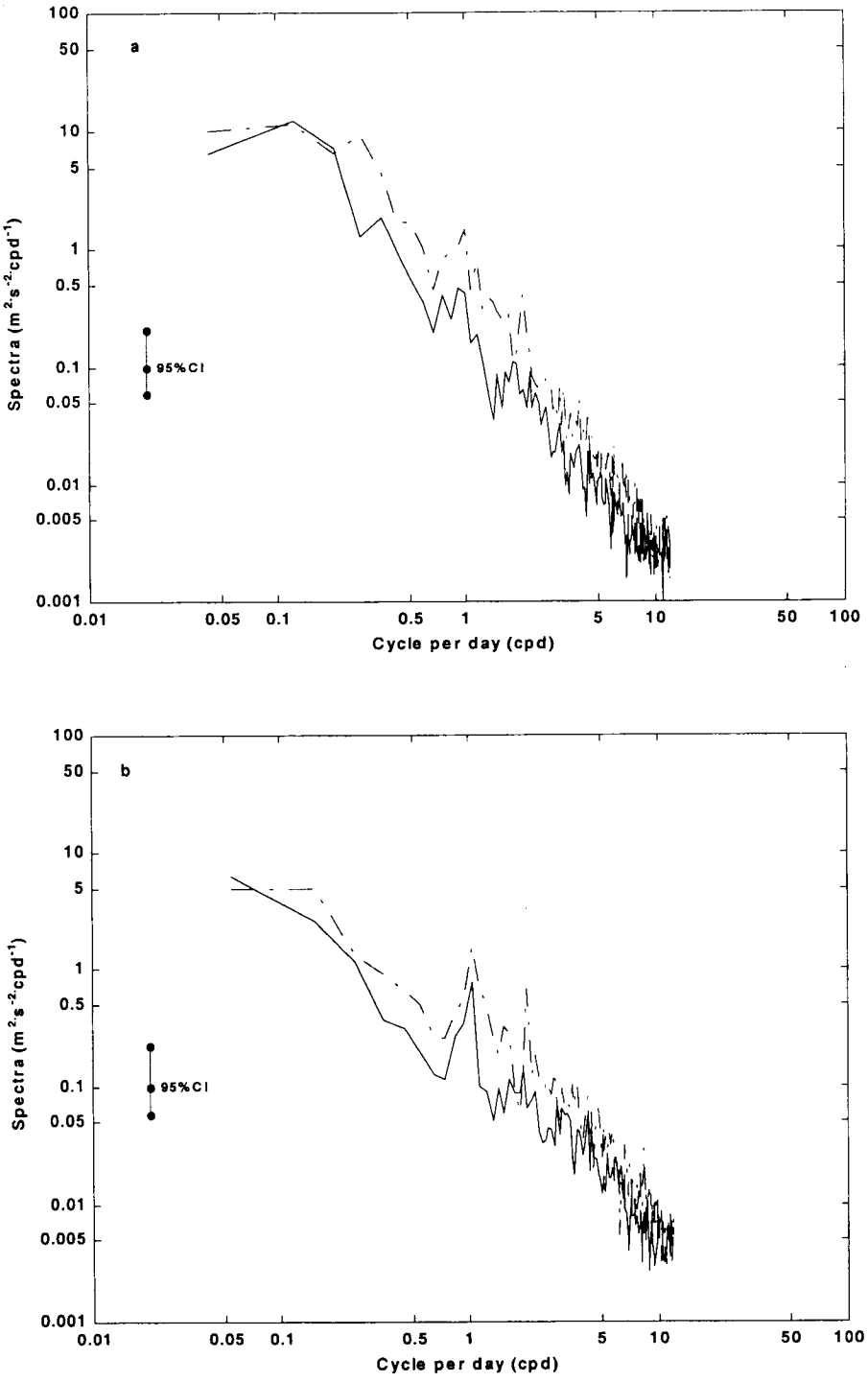

Figure II-9. Energy spectra (counterclockwise – solid line, clockwise – dash-dot line) of the winds observed at Freshwater Bayou (a) in the winter season and (b) in the summer season.

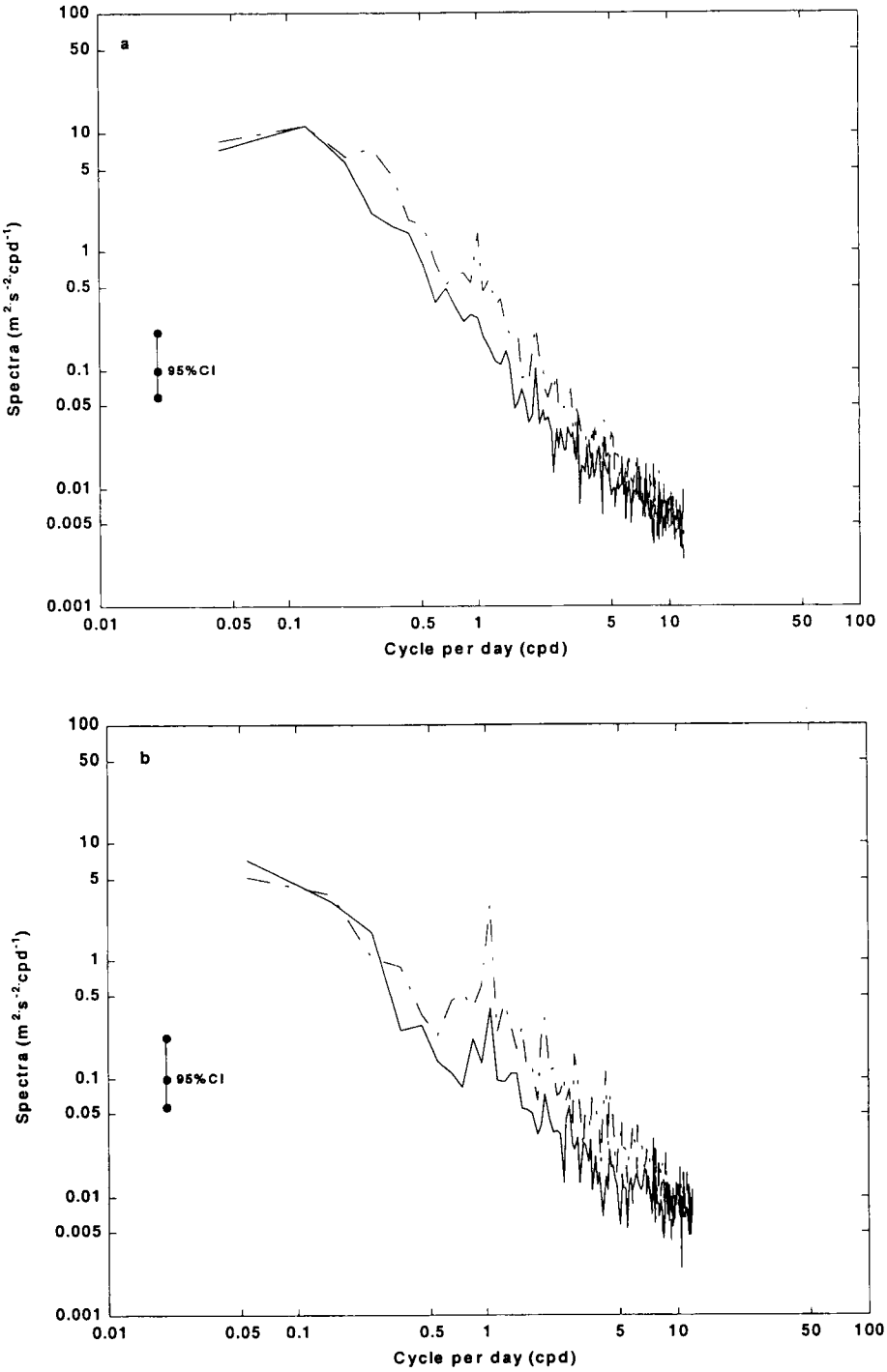

Figure II-10. Energy spectra (counterclockwise – solid line, clockwise – dash-dot line) of the winds observed at B42035 (a) in the winter season and (b) in the summer season.

selected for detailed analysis are (a) the summer upcoast regime of June 1 through August 30, 1996, which begins just before the spring 1996 Atchafalaya discharge maximum of 12,000 m^3/s and continues through the rapid drop to the minimum discharge of 3,000 m^3/s; and (b) the winter downcoast regime of September 20, 1996 through January 17, 1997, which occurs over a modest rise from 3,000m^3/s to 8,000 m^3/s. Maximum freshwater conditions on the shelf are probably sampled by the summer observations, while the winter observations are samples from a low freshwater storage situation on the shelf.

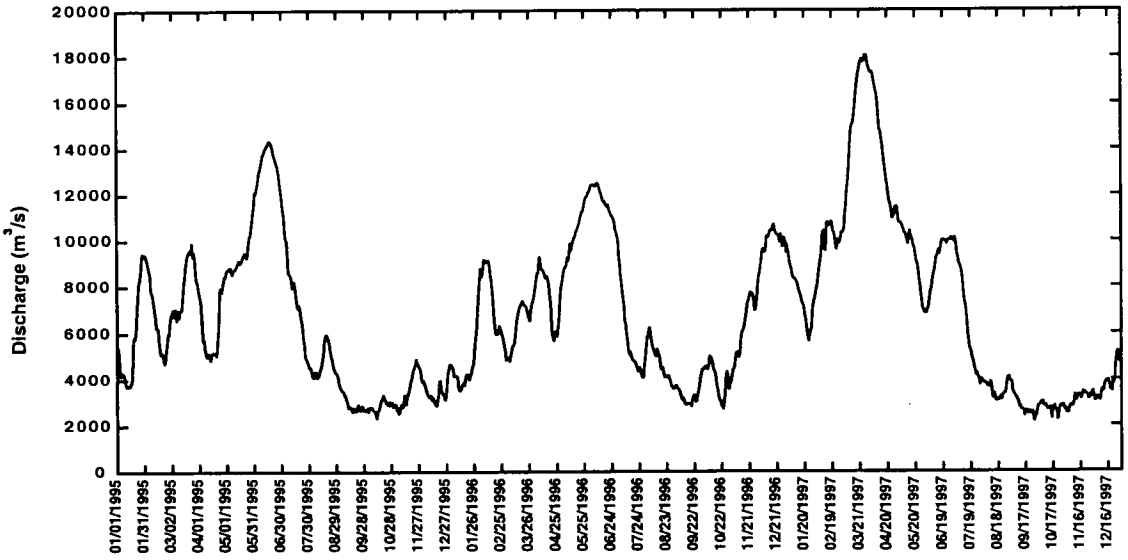

Figure II-11. The Atchafalaya River discharge at Simmsport 1995-97 illustrates the seasonal cycle of buoyant fresh water into MACP.

Subsequent data analysis also involves use of pressure gauge data (to calculate alongshore pressure gradients as a sea level slope). Examples of data for the winter observation period from the two stations, Freeport, Texas, and Oyster Bayou, Louisiana, which bracket the transport monitoring, are shown in Figure II-12. Clearly, there is a high degree of visual coherence between the two sites at both tidal and sub-tidal frequencies. Note that the water level set-ups and set-downs (Figure II-12) reach 40 to 50 cm on November 17 and 26, respectively, at both sites and that these two events seem to be related to the observed winds (Figure II-7). In summer (Figure II-13) these low frequency water elevation changes are only 10 to 20 cm in amplitude reflecting reduced wind energy levels.

It is, of course, the water level difference between sites representing the barotropic pressure gradient along the coast that would be a potential driving force for the coastal current. In Figure II-14a, b the demeaned 40-hour low passed water level difference between sites (Oyster Bayou minus Freeport) is shown for the same two periods illustrated previously. Both July (Figure II-14b) and November (Figure II-14a) differences show some fluctuations of different amplitudes. However, in July, there seems to be present a small but positive trend of the water level difference of the order of

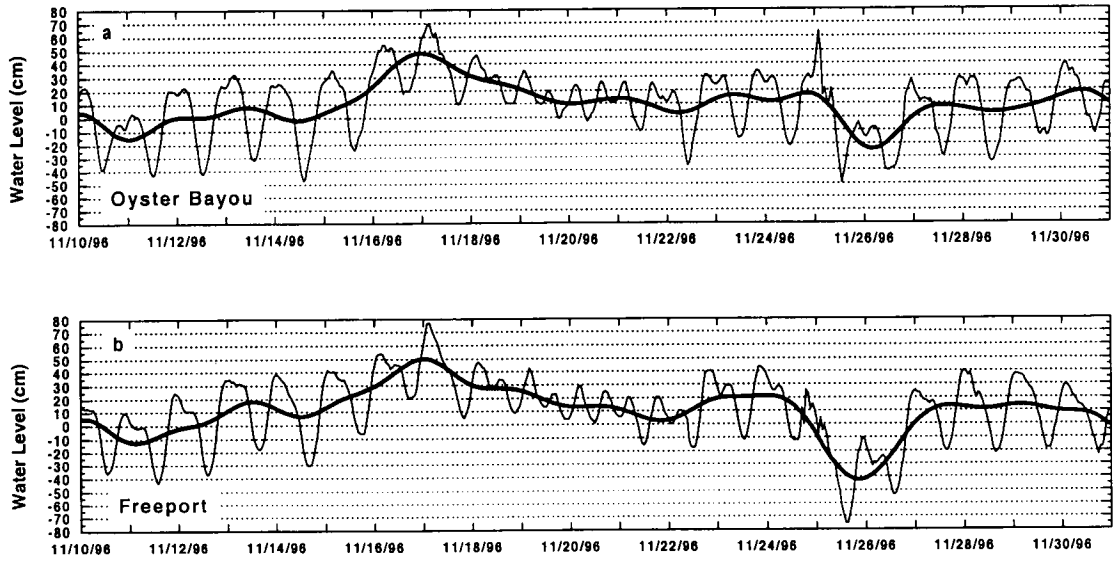

Figure II-12. Example of pressure gauge data converted to water level from (a) the Oyster Bayou site and (b) Freeport site November 10-30, 1996. Note the hourly traces showing tidal activity are over-plotted with the 40-hour low passed data.

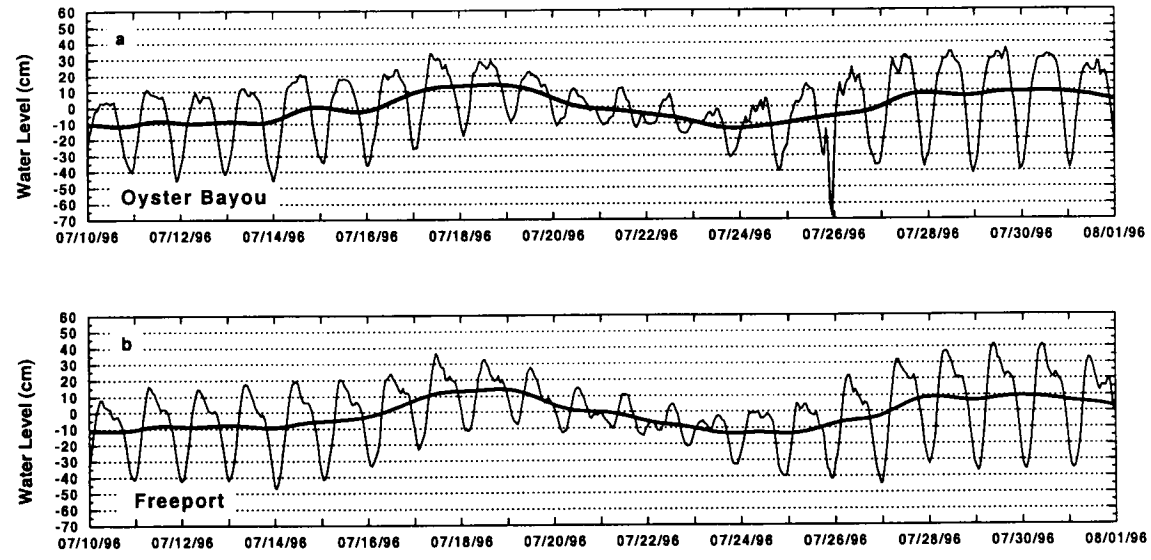

Figure II-13. Example of pressure gauge data converted to water level from (a) the Oyster Bayou site and (b) Freeport site July 10-30, 1996. Note the hourly traces showing tidal activity are over-plotted with the 40-hour low passed data.

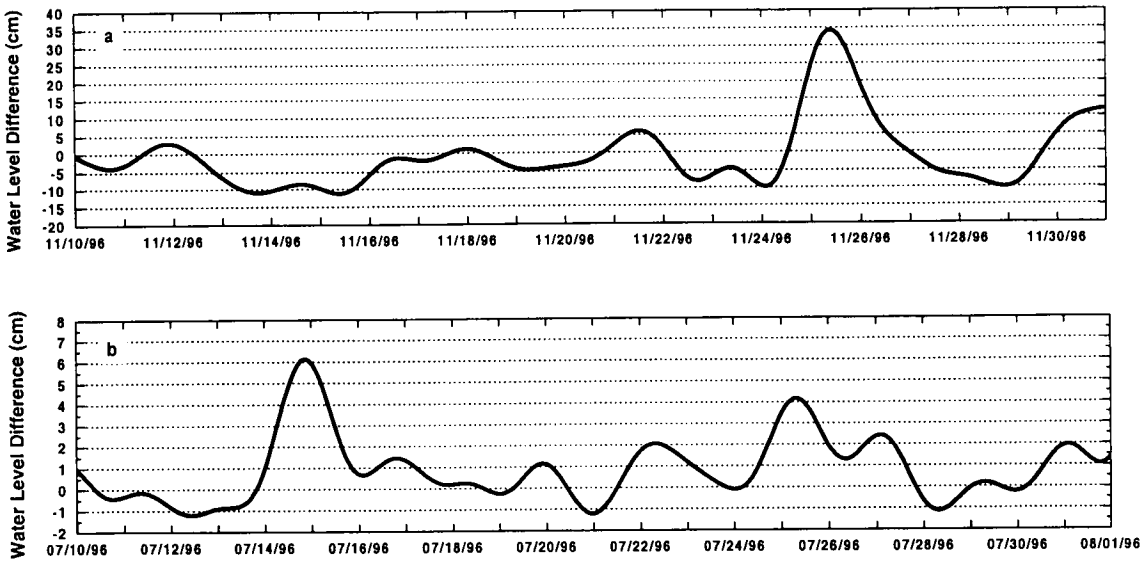

Figure II-14. A difference between demeaned water levels at Oyster Bayou and Freeport (OB-FP) for (a) November 10-30,1996 and (b) July 10-30, 1996. Note the difference in scale of the vertical axes.

1-2 cm. The major fluctuation (~ 6 cm) occurred on July 15 and it appears to be wind related. Note an increase in wind strength at both wind stations (Figure II-8). In November, however, this water level difference is negative for the major part of the record with values reaching up to -11 cm. Distinct positive anomalies are present on November 25 and 30. Inspection of the wind record (Figure II-7) shows that they both are associated with the wind field created by the atmospheric front passages. Note also that for both July and November, persistent trends of the water level difference oppose currents observed in the study area at the same time.

C. Results of Data Analyses

1. Structure of Currents

Before presenting the transport computations, it is instructive to examine spectral details of the currents at the central mooring C. In Figure II-15, the energy spectra (Bendat and Piersol, 1986) of the north-south (cross-shore) and east-west (alongshore) components of the current at the top instrument on mooring C for a seven month period (downcoast regime, 09/19/96-04/16/97) show strong peaks at both the diurnal and semi-diurnal frequencies. The semi-diurnal peak represents the important tidal constituent M_2. The diurnal peak, however, contains both the major diurnal tidal constituents, K_1 and 0_1, and the inertial energy, as the diurnal tidal and inertial periods at this latitude are only separated by about 30 minutes. Both spectra for the very low frequencies (<0.1 cpd) are almost constant and in a case of the alongshore component this part contains majority of energy. The frequency band 0.1 to 0.5 cpd (2-to 10-day periods) includes small peak in the energy spectra for both current components. This band is the so-called weather band,

which results from wind driving in the migrating atmospheric pressure systems that are common features in the northern Gulf of Mexico most of the year. Note, especially, that at the diurnal and semi-diurnal frequencies, the cross-shore (N-S) energy peaks are higher than the alongshore (E-W) peaks, but the energy in the weather band (2 to 10 days) is highly polarized in the alongshore direction.

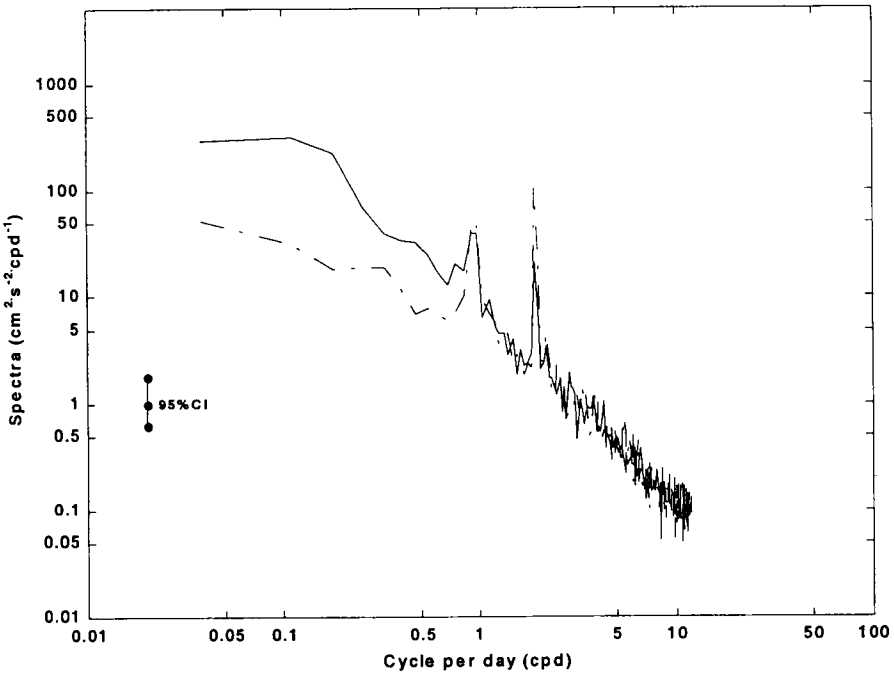

Figure II-15. Energy spectra for the EW (solid line) and NS (dash-dot line) current components of the top meter at mooring C (September 19, 1996-April 16,1997).

The current spectra of the middle instrument (not shown) are generally similar to those obtained for the top instrument at mooring C in the winter period. The spectra of the currents recorded by the bottom meter, however, differs from these described above and the major differences are as followed: (1) energy level at the inertial-diurnal frequency band drops off drastically for both current components; (2) such a extreme drop of energy is also present at the semidiurnal frequency for the alongshore component; (3) energy associated with subtidal motion is about two times smaller than that observed at the top and middle instruments. The bottom instrument was placed just about 3m above the bottom, therefore, this decrease of the energy level at different frequencies is probably associated with bottom friction.

During the downcoast flow regime, coherency of alongshore currents between the three depth levels on mooring C is strong. Figure II-16 shows a broad band of significant coherence from 0.1 to 0.5 cpd (2 to 10 days) between the upper and mid-depth meters. The coherence decreases in strength from 10-to 2-day periods, but the phase lag (not

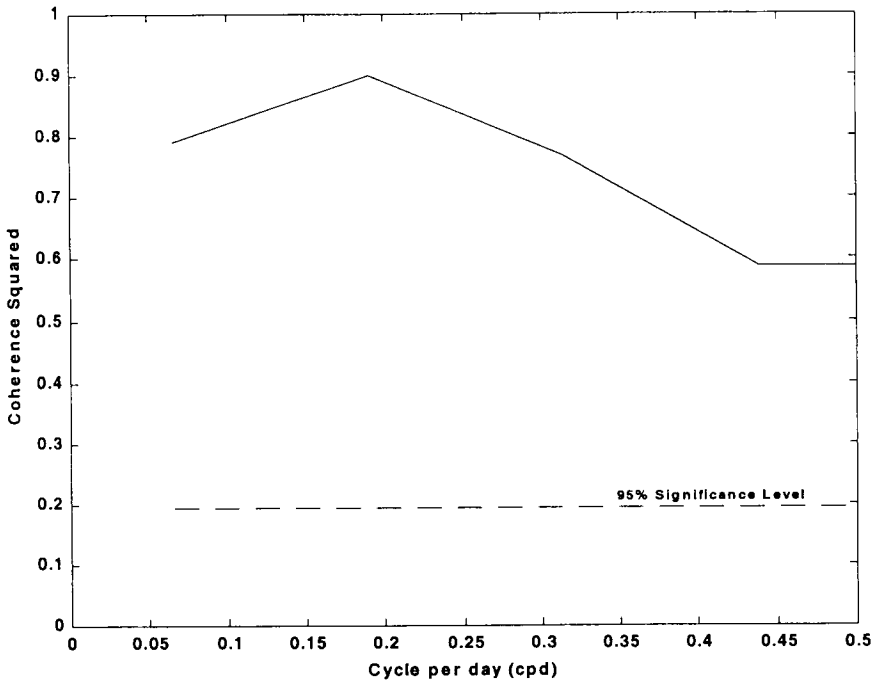

Figure II-16. Coherence squared for the alongshore current component between the upper and mid-depth meters at mooring C for four months of winter 1996-1997.

shown) is uniform and is not statistically different from zero across the band. The coherence between the middle and bottom meters at mooring C, shown in Figure II-17, is even stronger across the entire subtidal band between 0.1 and 0.2 cpd, again, with about a zero phase lag.

These diagrams show that for periods of 2.5 to 10 days, the alongshore currents in the water column respond barotropically between the top and bottom current meters. The lower water column, however, responds barotropically all the way down to periods of one-day duration, apparently reflecting the more transient influence of wind forcing on the upper water column.

The spectra of the subsurface currents observed at mooring C in the summer (Figure II-18) have the same major peaks associated with semidiurnal and diurnal tidal, and inertial motions. The low frequency part of these spectra ($\leq$ 0.5cpd) is characterized by almost linear increase of energy with decreasing frequencies for both alongshore and cross-shore components. Resembling the winter season, the subtidal energy is polarized in the alongshore direction, however, this polarization only appears for motion with periods larger than 4 days. The pattern is closely replicated at the middle instrument level (data not shown). Similar to the downcoast regime, energy level of the currents recorded by the bottom instrument, which was deployed ~3 m above the bottom, is smaller for the same frequency bands than those observed for the currents of the subsurface and middle instruments. This energy drop off is probably again associated with the bottom friction.

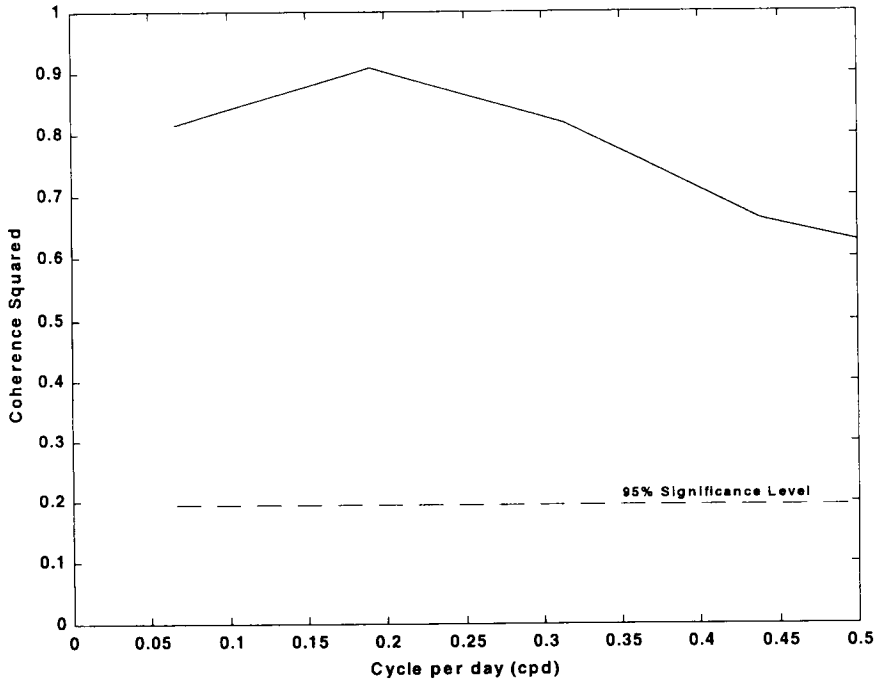

Figure II-17. Coherence squared for the alongshore current component between the mid-depth and lower meters at mooring C for four months of winter 1996-1997.

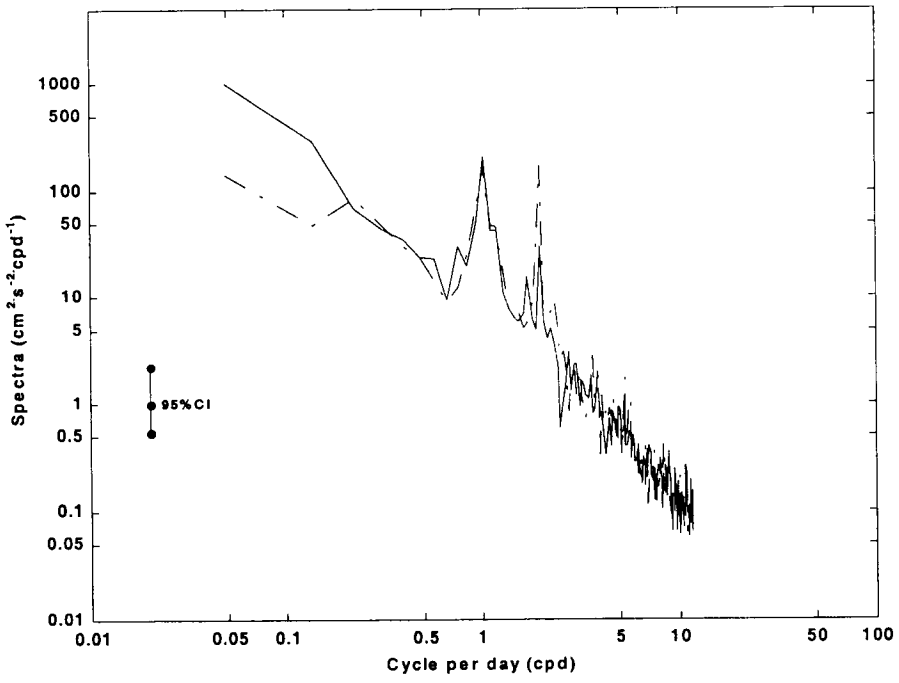

Figure II-18. Energy spectra for the EW (solid line) and NS (dash-dot line) current components of the top meter at mooring C from June 1, 1996 through August 31,1996.

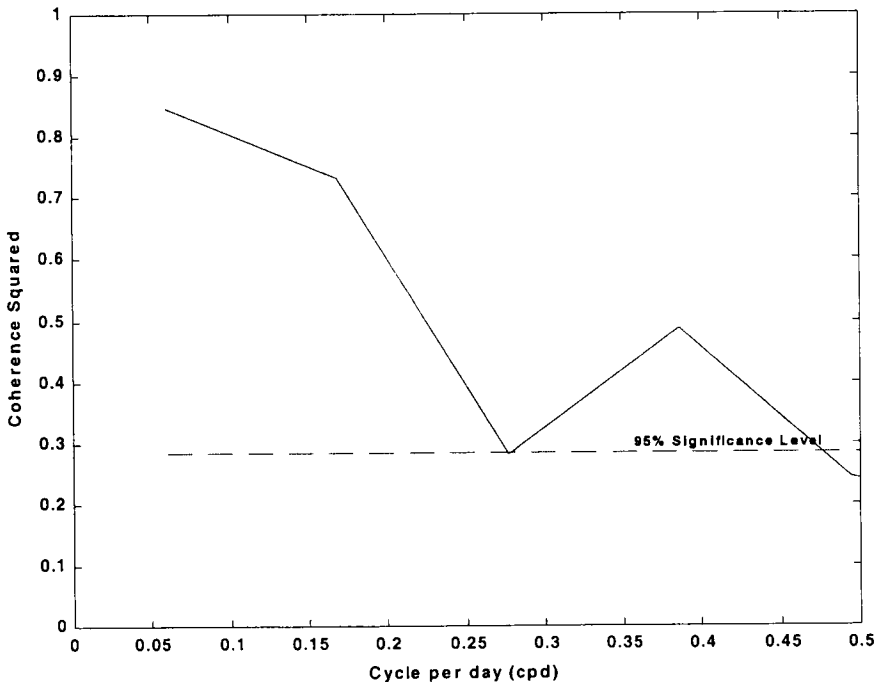

Figure II-19. Coherence squared for the alongshore current component between the upper and mid-depth meters at mooring C for three months of summer 1996.

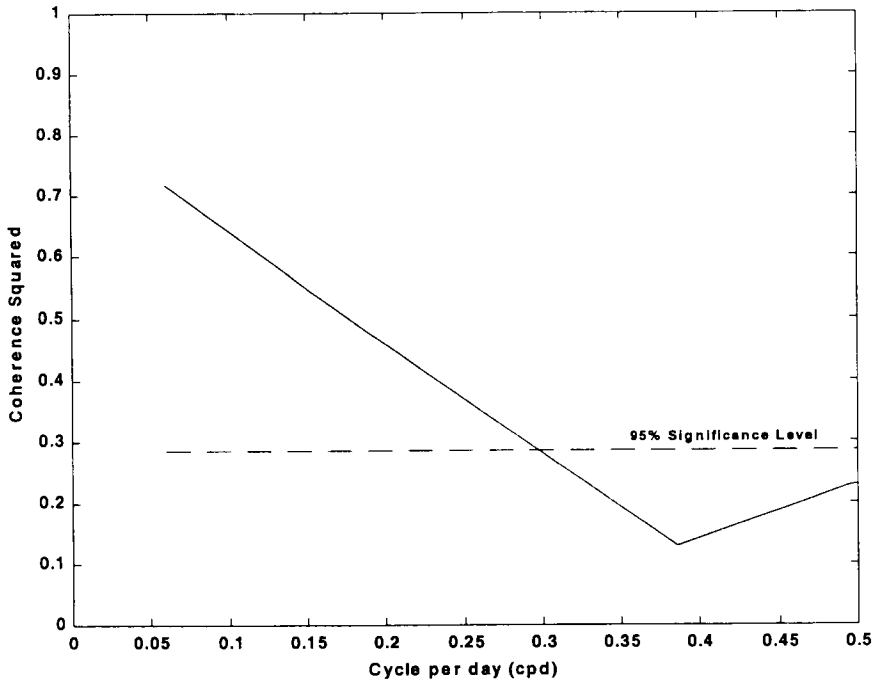

Figure II-20. Coherence squared for the alongshore current component between the mid-depth and lower meters at mooring C for three months of summer 1996.

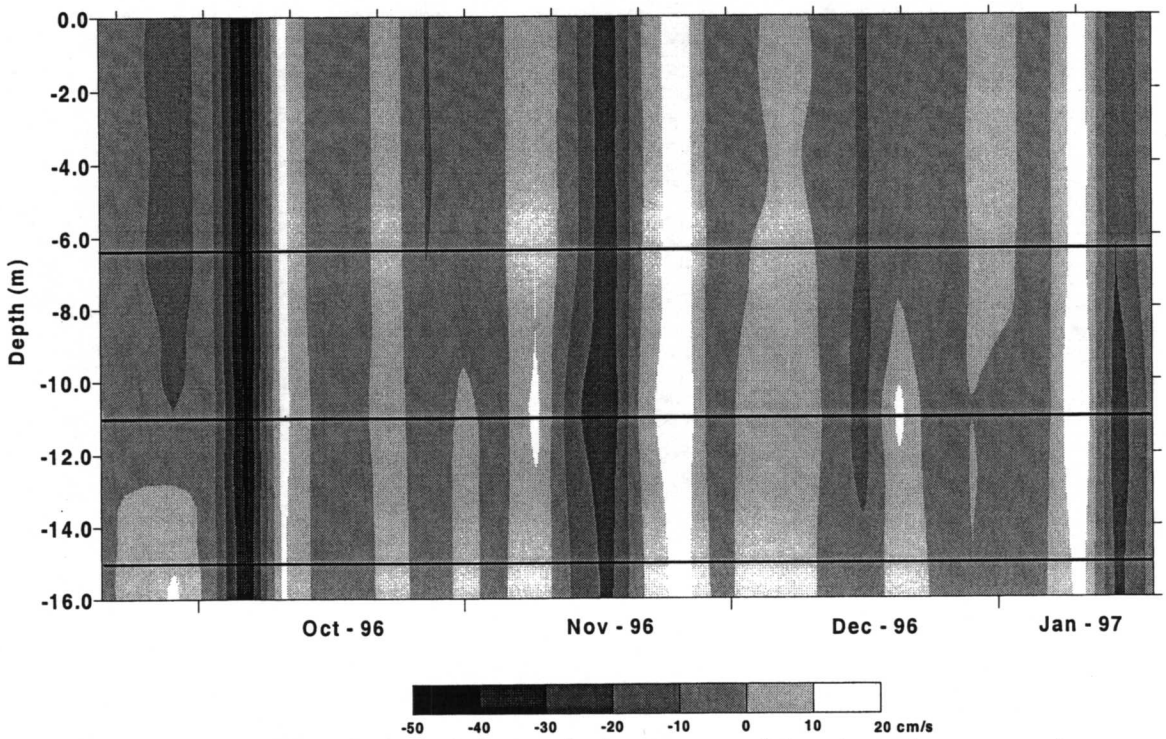

Figure II-21. Temporal evolution of the vertical structure of the alongshore current component at mooring C (horizontal lines indicate depths of the instruments), September 1996 through January 1997. Note the characteristic vertically coherent upcoast and downcoast pulsations; speeds are in cm/s.

Coherency of the alongshore currents between the three depth levels on mooring C in summer is not as strong as it is for the winter period. Significant coherence in the subtital frequency band is only observed between the upper and mid-depth meters for frequencies less than 0.3 cpd and centered on 0.38 cpd (Figure II-19). The phase lag (not shown) is uniform and is not statistically different from zero across the subtidal band. The coherence between the mid-depth and bottom meters is statistically significant only for subtidal motion with frequencies less than 0.3 cpd (Figure II-20) with the zero phase lag.

2. Cross-Sectional Transport

In order to calculate the transport in the LTCC through the section off Cameron, we first produce a time series of the 40-hour low passed current component at each current meter. A gridded data set is then constructed at the cross-section at each hour using 1-m depth by 2-km cross-shore mesh. To rigorously define the offshore extent of the coastal current is obviously difficult because of its inherent temporal variability as illustrated in Figures II-5 and II-6.

Figure II-21 shows that the subtidal behavior of the water column at mooring C near the middle of the section is largely characterized by vertically coherent upcoast and downcoast fluctuations lasting several days to a week. Alongshore upcoast (downcoast)

speeds are positive (negative). Accordingly averaged over a month of positive and negative pulses, mean speeds are low but consistent with the expected seasonal cycle. Figure II-22, for example, shows the average speeds across the section for October 1996, well into the downcoast flow season. Mean speeds are 5 to 10 cm/s and all downcoast, as expected for this time of the year.

The mean alongshore speed distribution for July 1996 (Figure II-23) is not only less energetic, (3 to 5 cm/s) with the exception at the seaward edge, but directed upcoast (positive) as expected for the summer flow season. The limited salinity data recovered from the moorings suggest the presence of coastal plume water across the section even as far out as mooring A, except for late August 1996. Thus, we make an operational definition of the coastal current transport by integrating across the section between moorings A and G and recognizing that this is an estimate of the lower band. It does, however, have the advantage of being consistent with the ship-mounted ADCP estimates of Murray et al. (1997).

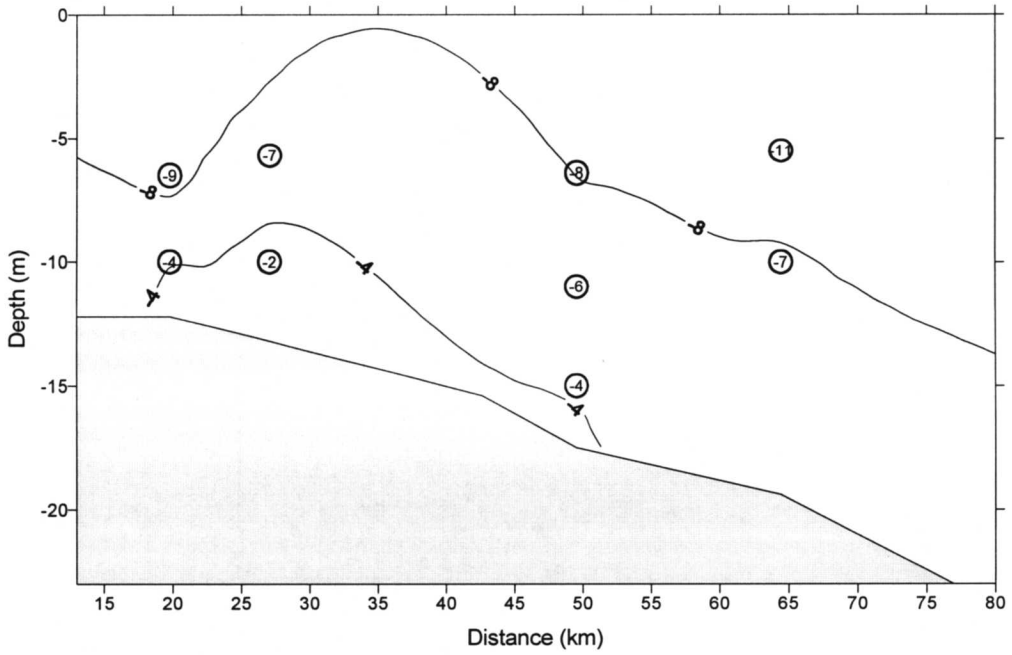

Figure II-22. Cross-sectional distribution of subtidal alongshore currents (monthly means in cm/s), October 1996. Small open circles indicate the current meter location; negative values indicate the downcoast flow (the flow to the west in this location).

The alongshore transport through the section during the winter downcoast regime of 1996-97 is shown in Figure II-24. Note the persistent downcoast transport of 100 to 150 x 10^3 m^3/s with a record length mean of – 60,774.2 m^3/s (with a mean squared error of 18,553 m^3/s). Significant bursts of elevated downcoast transport occur on October 6, November 17, and January 8 and 13. We will examine the spatial characteristics of several of these bursts subsequently.

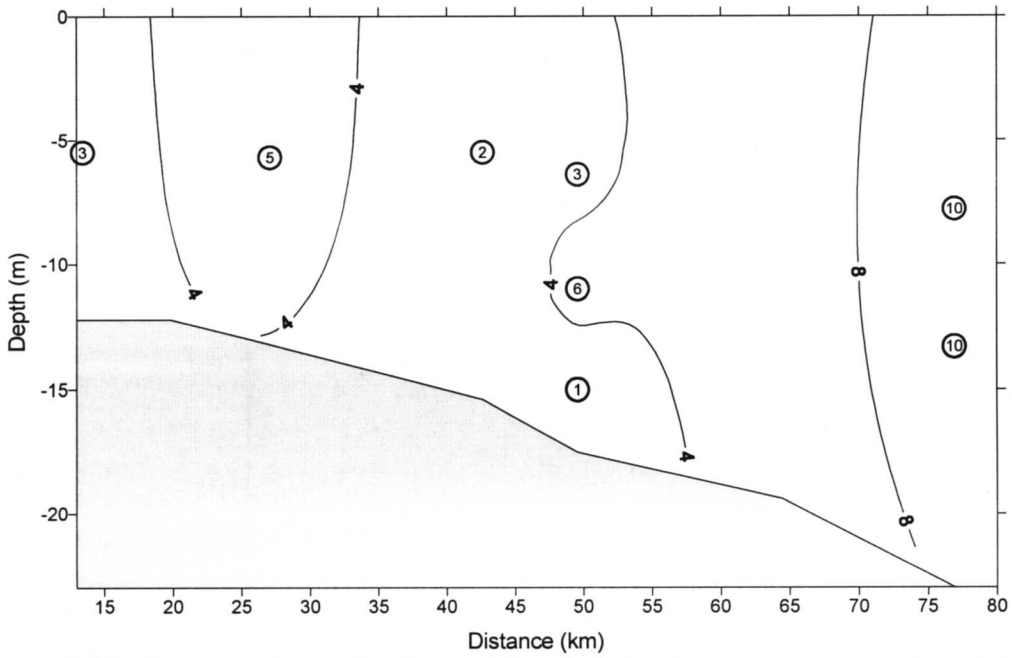

Figure II-23. Cross-sectional distribution of subtidal alongshore currents (monthly means in cm/s), July 1996. Small open circles indicate the current meter location; positive values indicate the upcoast flow (the flow to the east in this location).

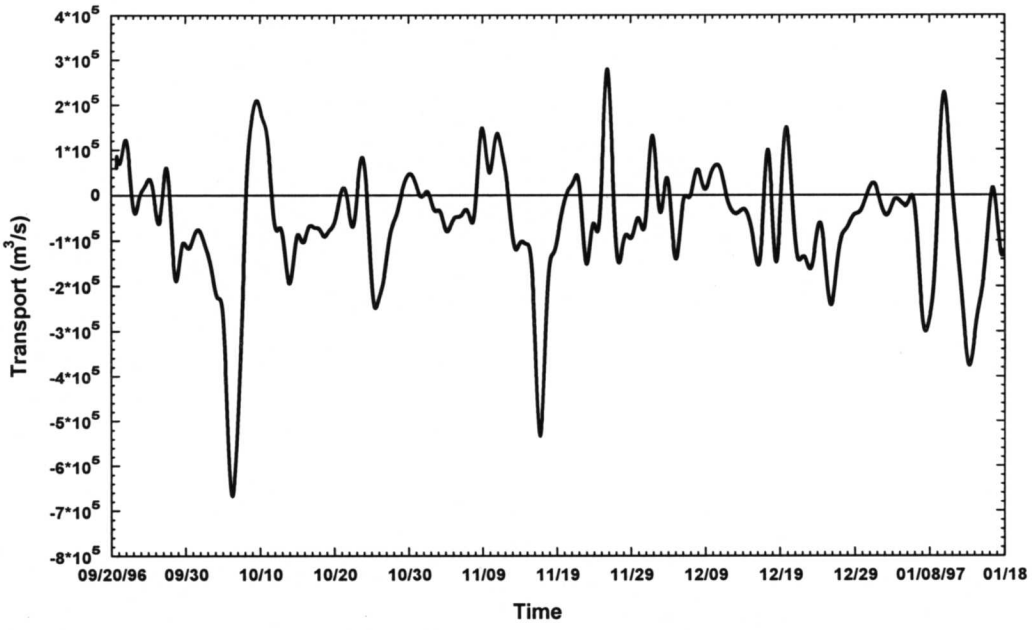

Figure II-24. Transport in the LTCC during the winter downcoast regime, September 1996 through January 1997. Note the average downcoast transport of -60,774.2 m^3/s and the extreme temporal variability (positive values indicate the upcoast transport, negative values indicate the downcoast transport).

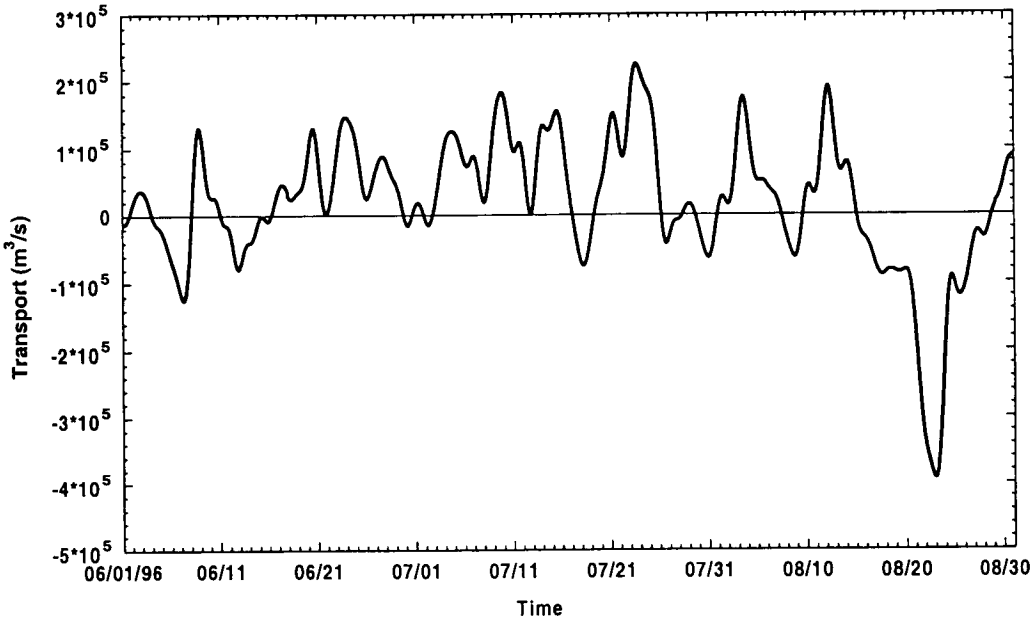

Figure II-25. Transport in the LTCC during the summer upcoast regime of 1996. The average transport for this time period is 19,798.9 m^3/s (positive values indicate the upcoast transport, negative values indicate the downcoast transport).

The corresponding transport during the preceding summer upcoast regime is shown in Figure II-25. As expected, regional forcing conditions in the summer of 1996 are such that the coastal current reverses direction and decidedly shifts upcoast by June 9 and remains upcoast for most of the summer. Note, however, the extreme temporal variability in the flow. Fluctuations in transport, which range from slightly below 0 (downcoast flow) to maximums of 150 to 200 x 10^3 m^3/s (upcoast flow), occur on roughly a 5-day time scale. A record length mean for this period is 19,799 m^3/s with a mean squared error of 41,296 m^3/s .

The most energetic of these oscillations during the winter period appears to be closely related to direct wind driving. The event between October 2 and 11 is a prime example to investigate. Ten days of northeasterly winds exert alongcoast and downcoast wind stresses to produce the cross-sectional speed distribution shown in Figure II-26. Speeds are in excess of 30 cm/s across the entire section with two zones of intensification. A high-speed jet in excess of 60 cm/s occupies the outer edge of the section. Its seaward extent, unfortunately, is unresolved by the mooring array. A second jet, nearly as strong, occupies the inshore end of the section. Previous sections taken during LATEX B cruises suggest that intense vertical mixing, combined with zones of intensified horizontal density gradients (fronts), are associated with these jets in the coastal current. The cessation of the southwestward wind stresses driving the October 6 intensification of the downcoast flow event is followed by an upcoast flow event, probably driven by the pressure gradient setup to balance and oppose the wind stress.

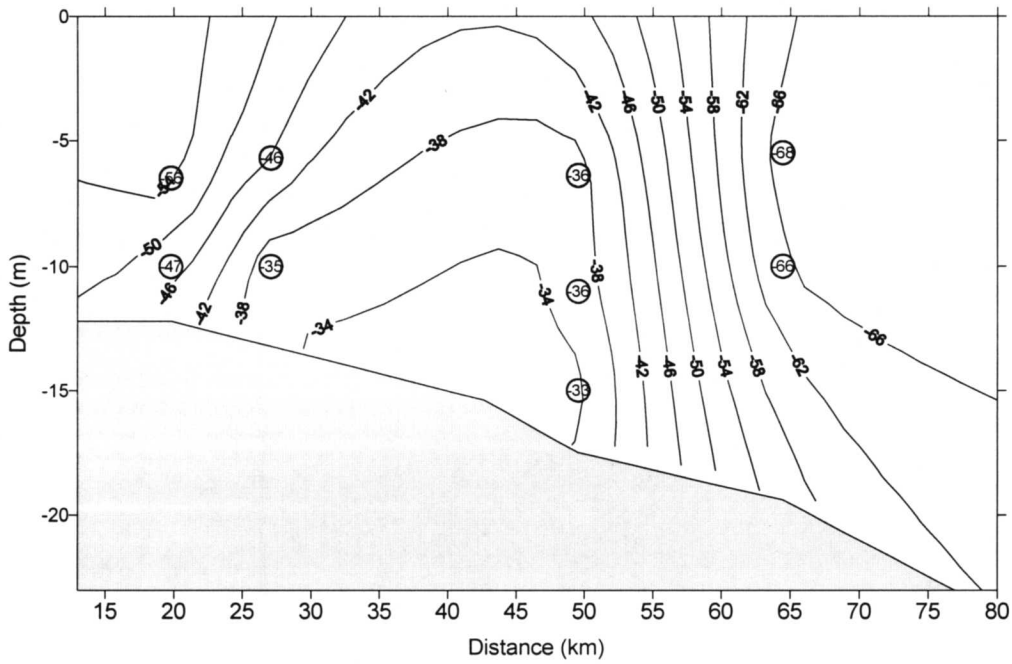

Figure II-26. Cross-sectional distribution of alongcoast speeds on October 6, 1996, illustrating a downcoast intensification during the winter regime. Note highly energetic jets in excess of 50 cm/s at the inshore and offshore ends of the section (positive values indicate the upcoast flow, negative values indicate the downcoast flow).

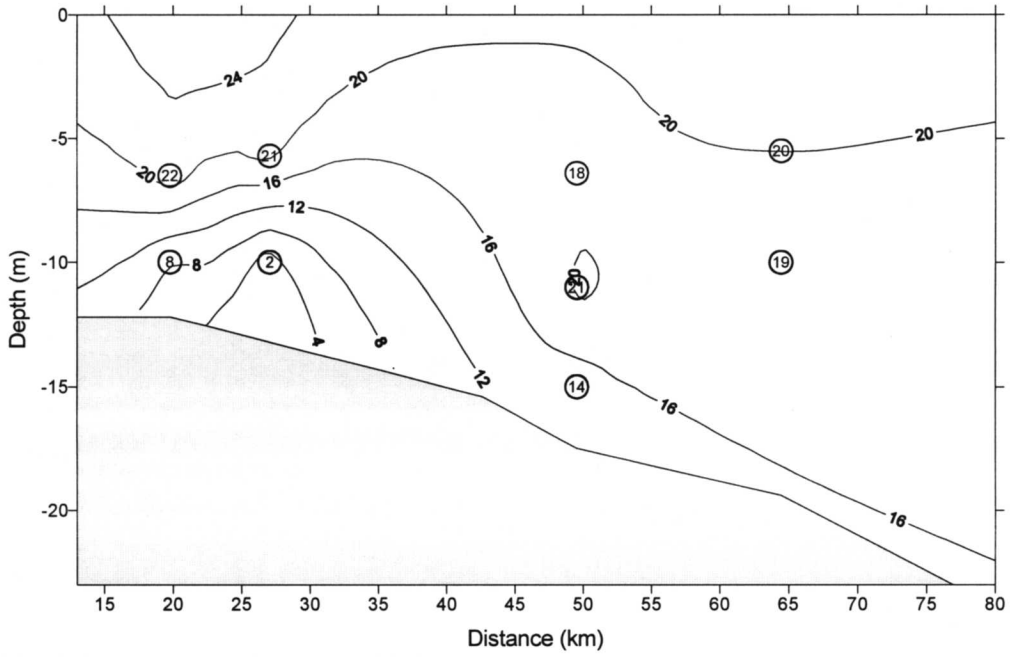

Figure II-27. Cross-sectional distribution of alongcoast speed on November 26, 1996. An example of an intensified upcoast reversal during the winter downcoast regime (positive values indicate the upcoast flow, negative values indicate the downcoast flow).

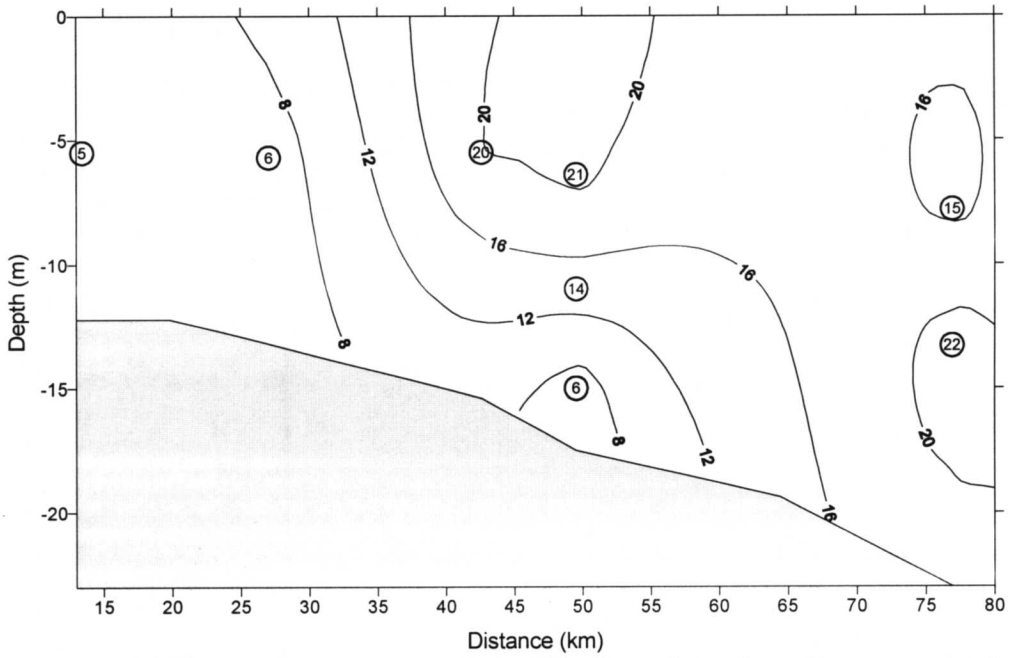

Figure II-28.The strongest upcoast intensification of the alongshore current field occurring on July 23, 1996 is notable for its moderate speeds barely in excess of 20 cm/s (positive values indicate the upcoast flow, negative values indicate the downcoast flow).

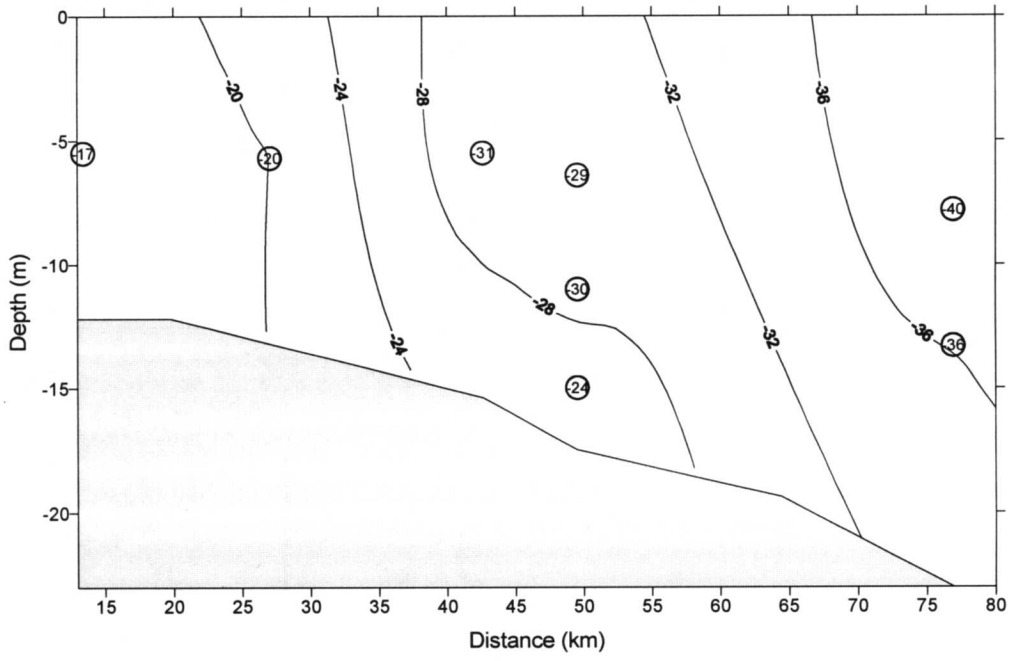

Figure II-29. A strong downcoast anomaly driven by persistent easterly winds lasted for over 10 days with peak on August 23, 1996. Speeds across the section were 20-40 cm/s (positive values indicate the upcoast flow, negative values indicate the downcoast flow).

Intense upcoast events occur intermittently during the winter downcoast regime. Figure II-27 shows an example of the upcoast flow with speeds of 10-20 cm/s across the section that occurred on November 26, 1996. A zone of low speeds near the bottom 15 to 30 km offshore perhaps suggests baroclinic effects (a lens of higher density water).

The time series of transport during the summer upcoast regime (Figure II-25) is similarly characterized by intense fluctuations of several days to week time scales. The strongest upcoast intensification—centered on July 23 (Figure II-28)—is notable for its rather modest current speeds of 20 cm/s. Wind driven upcoast currents are upwelling favorable, leading to offshore transport in the surface layer and consequent (a) suppression of cross-shore density gradients and (b) reduction of baroclinic alongshore velocities.

A period of anomalously strong easterly winds in late August flipped the upcoast regime (Figure II-29) into a downcoast state for over 10 days. Speeds of 20 to 40 cm/s extend across the section. This downwelling favorable flow typically intensifies density gradients (Murray and Young, 1985) driving a strong baroclinic current component, which concentrates and intensifies the coastal current.

3. Decorrelation Time Scales across the Array

We begin this investigation into temporal and spatial coherence characteristics by interpreting the autocorrelation function (Bendat and Piersol, 1986) of the 40-hour low passed data from the upper level instruments at an inshore mooring F and at an offshore mooring B (Figure II-30). The area under the autocorrelation curve integrated out to the first zero crossing is referred to as an integral time scale and is often used as an estimate of the decorrelation time scale. Alternatively, the first zero crossing or its interpolation if noise prevents a zero crossing, is also often used as an estimate for the decorrelation time. The decorrelation times for all instruments are listed in Table II-2.

It is immediately clear that the cross-shore (v) components at both moorings have a short decorrelation time close to 35 hours. In contrast, the alongshore (u) component at the offshore mooring B, 65 km from the shoreline, has a decorrelation time of 75 hours while the decorrelation time of the same component at the inner mooring F, which is only 20 km from the coast, is reduced to 60 hours. Thus, we see very little coherence in the cross-shore motion at subtidal frequencies but longer decorrelation times of 2.5-3 days in the alongshore components may suggest that this flow is better organized. Larger eddy length scales are, of course, expected farther offshore and this is consistent with the observed alongshore decorrelation time scales. The other upper level instruments at moorings E and C, which operated during the winter interval showed similar behavior in their autocorrelation function, i.e. minimal decorrelation times in the cross-shore components and 2-3 days in the alongshore components.

The decorrelation time scales for the four upper level instruments that operated during the winter period are plotted as a function of a distance offshore for each mooring

Table II- 2

Decorrelation time of alongshore and cross-shore current components for the summer (Summer_u and Summer_v) and winter (Winter_u and Winter_v) flow regimes. Decorrelation time is given in hours: values without brackets – first zero crossing, values in brackets – autocorrelation function reaches its standard error value that is 0.021 for both components.

Mooring/Instrument	Summer_u	Summer_v	Winter_u	Winter_v	Distance Offshore (km)
MA_top	402(286)	494(489)			76.92
MA_mid	397(288)	308(304)			76.92
MB_top			76(74)	134(32)	64.45
MB_bot			71(68)	63(61)	64.45
MC_top	163(158)	125(82)	66(64)	34(24)	49.54
MC_mid	221(208)	60(58)	60(39)	49(47)	49.54
MC_bot	182(175)	64(50)	61(59)	54(53)	49.54
MD_top	86(81)	112(91)			42.61
ME_top	92(90)	88(85)	55(53)	32(30)	27.06
MF_top			60(58)	30(23)	19.78
MF_bot			46(44)	63(61)	19.78
MG_top	86(84)	68(64)			13.42

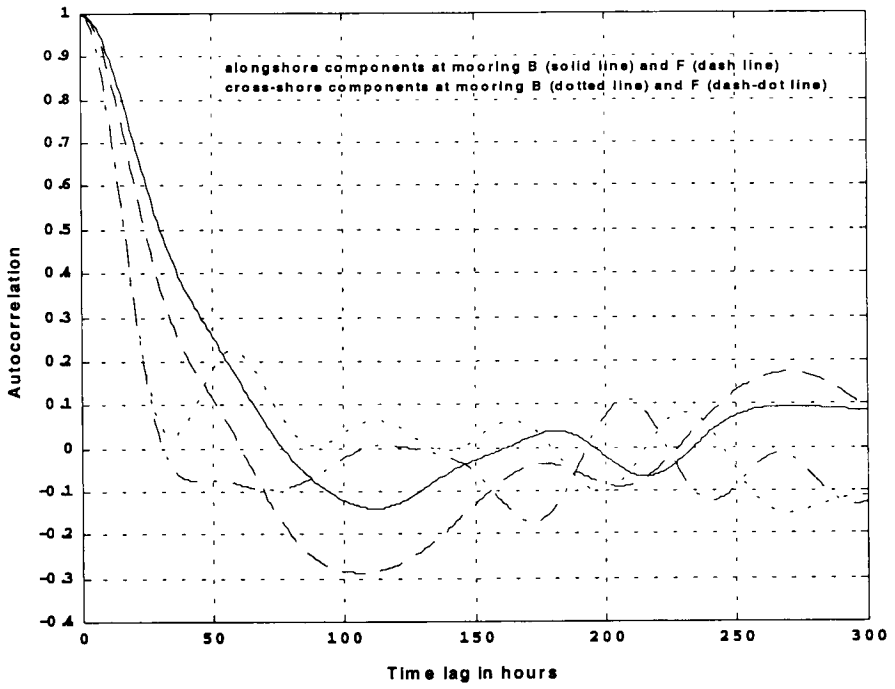

Figure II-30. Autocorrelation diagrams of 40 hour low passed data from the upper level instruments at moorings B and F for the winter observation interval.

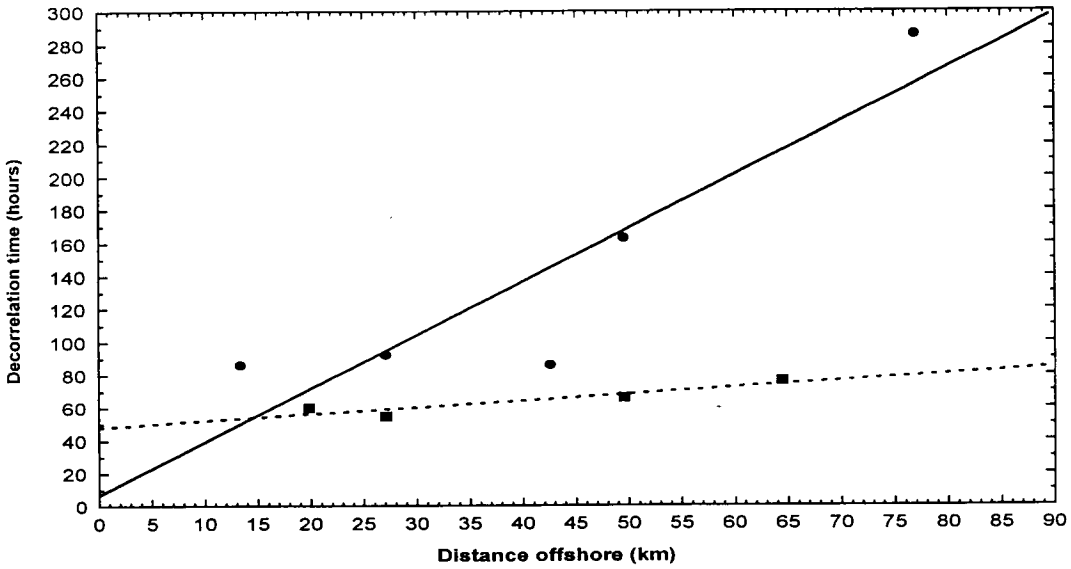

Figure II-31. Decorrelation time scales t* for the alongshore components of the upper level current meters for both the winter (squares and dash line) and summer observation (circles and solid line) intervals plotted as a function of distance offshore. Note greatly increased values of t* during the summer regime.

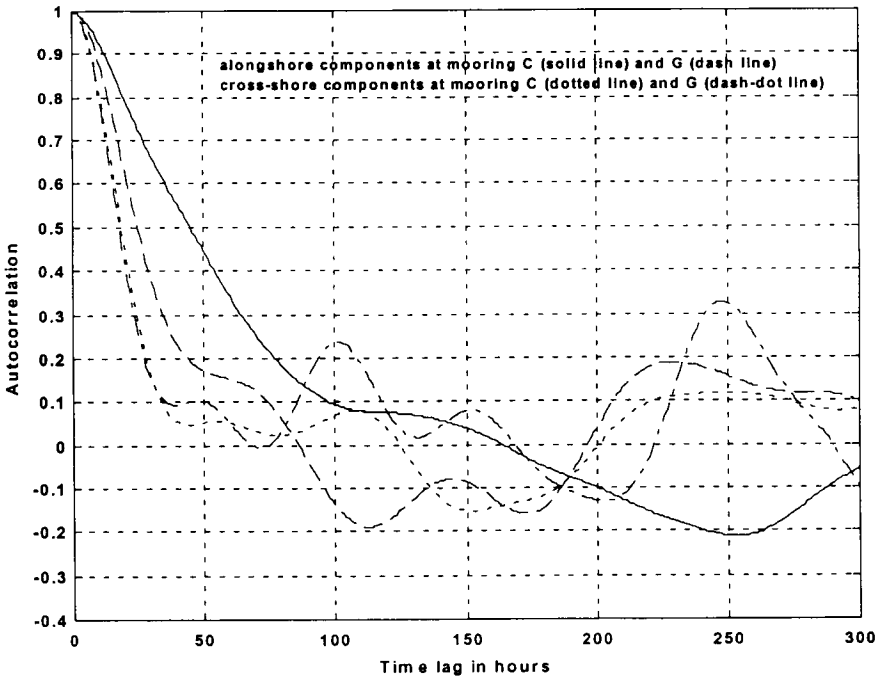

Figure II-32. Autocorrelation diagrams of 40 hour low passed data from the upper level instruments at moorings C and G for the summer observation interval. Cross-shore decorrelation time scales are negligible while alongshore decorrelation time scales are several days.

in Figure II-31. While ranging between 55-75 hours the limited data are consistent with an increase of the decorrelation time with distance offshore.

The rate of increase with distance offshore of the decorrelation time scales is notably different during the summer regime, however. Figure II-31 shows that the field of points associated with the summer regime does not only overlap with the winter points but that the decorrelation time scales increase four times faster in summer than in winter.

Autocorrelation diagrams for the summer regime show distinctly larger time scales than that of the winter for the subtidal fluctuations in the alongshore (u) component. Figure II-32 shows that at the C mooring (50 km offshore) the u decorrelation time is 100-120 hours, while at the G mooring (14 km offshore) it is about a half of that value. Similar to the downcoast flow, the cross-shore (v) components at both moorings show much shorter decorelation times than those of the alongshore components.

Mooring A is 27 km further offshore than mooring C and shows significantly different characteristics as illustrated in Table 2. Decorrelation times appear to be over 300 hours in the u component and over 400 hours in the cross-shore (v) component. Mooring A in summer appears to be largely decoupled from the damping influence of the coast. Physically, this observation is consistent with our understanding of the summer reversal consisting of the relict plume waters spreading out offshore under the influence of Coriolis forcing as it works its way upcoast. The much greater offshore extent of the surface layer (dominated by plume waters) presumably allows for greater length and, hence, greater time scales of the subtidal fluctuations.

4. Spatial Correlation

The cross-correlations between the upper meters at moorings B and F (a separation distance of 45 km) for both the alongshore and cross-shore current components for the winter observation period are shown in Figure II-33. Maximum correlation at essentially zero time lag is 0.83 for the alongshore component and reduces to 0.3 for the cross-shore component. 95% significance levels (Sciremammano, 1979) of 0 lag correlation coefficients of the alongshore and cross-shore components for the winter season are 0.31 and 0.21, respectively. Results are basically similar for all other available mooring pairs except for those immediately adjacent to each other. For these contiguous pairs the cross-shore components also become significantly correlated.

The results of the cross-correlation analysis are summarized on correlation-separation distance diagrams (Figures II-34 and Figure II-35). Figure II-34 shows that for all six mooring pairs the correlation coefficient is in the 0.8-0.9 range for the alongshore flow component in the downcoast regime. Such high correlation coefficients suggest that the cross-shore spatial length scales for the alongshore velocities is very much greater than 50 km. As expected the cross-shore spatial length scales of the cross-shore speeds are quite different. Figure II-30 shows a rapid decrease of the correlation coefficients with an increasing mooring separation implying that the spatial length scale of this

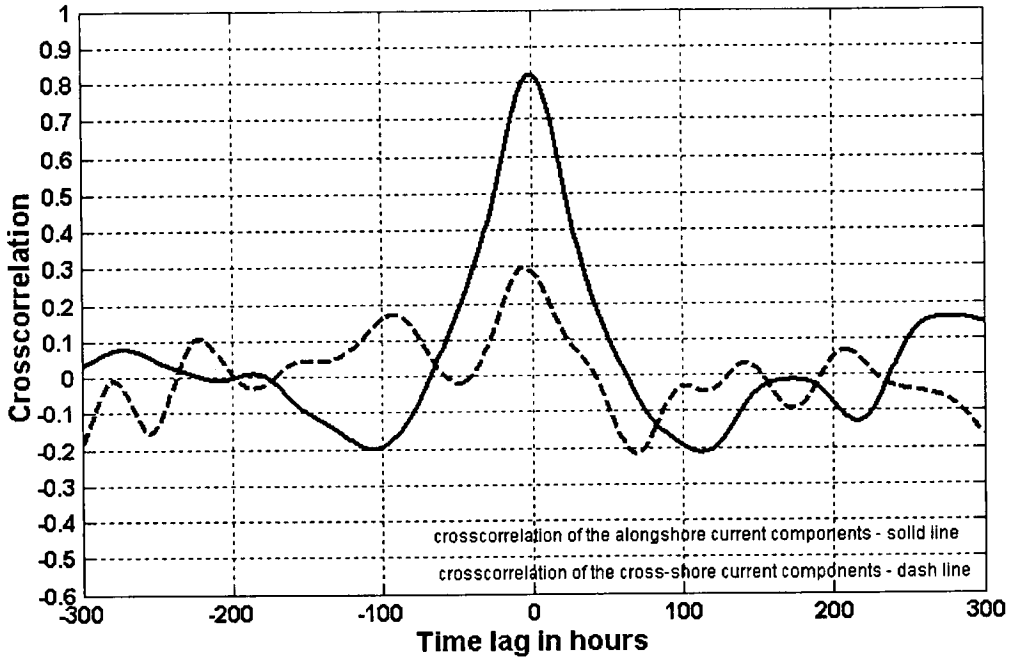

Figure II-33. Cross-correlation functions of the alongshore (solid line) and cross-shore (dash line) components of currents measured at the upper meters of moorings B and F for the downcoast flow regime.

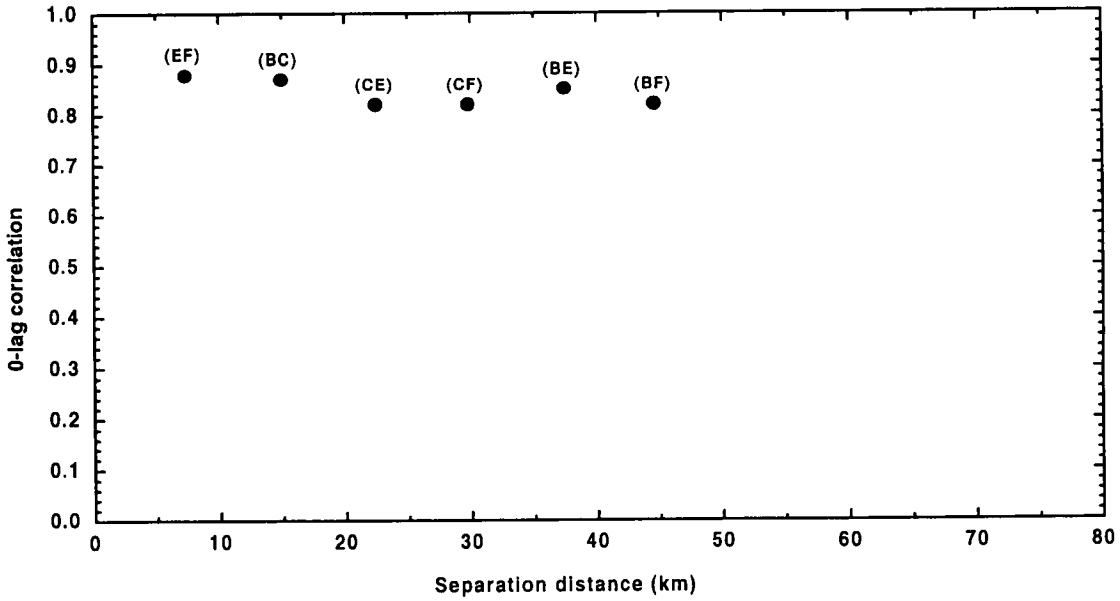

Figure II-34. Cross-correlation separation distance diagram of the alongshore current components for the downcoast flow regime (letters in brackets indicate mooring pairs).

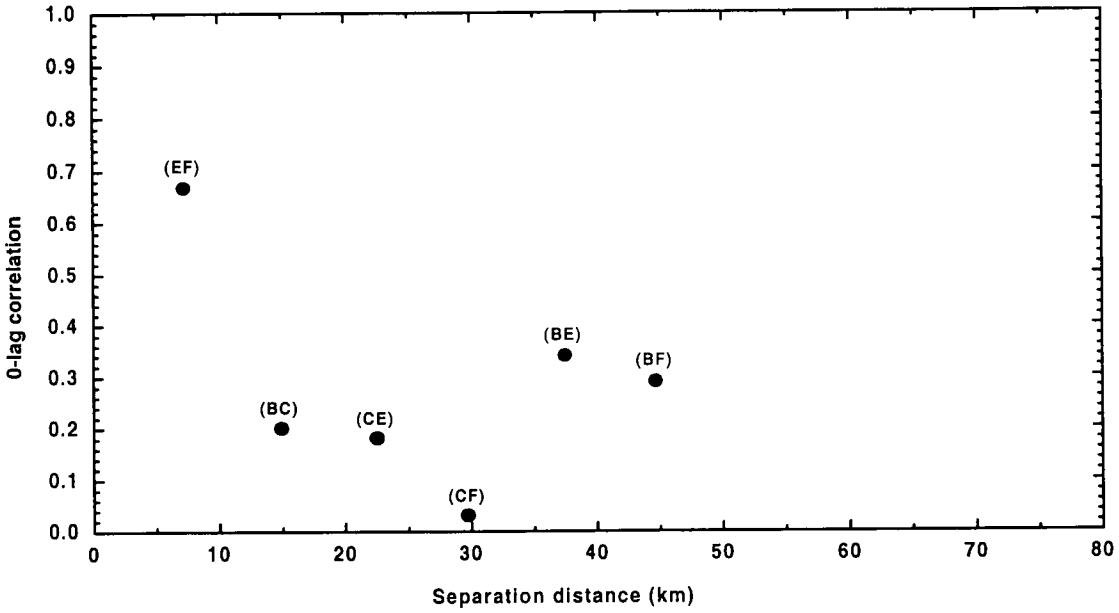

Figure II-35. Cross-correlation separation distance diagram of the cross-shore current components for the downcoast flow regime (letters in brackets indicate mooring pairs).

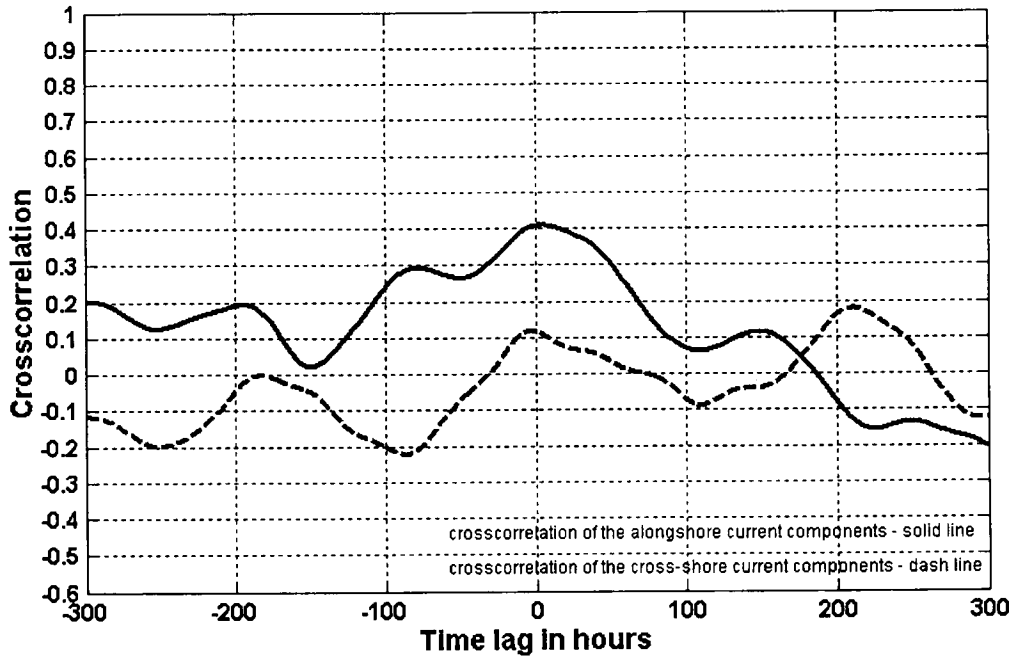

Figure II-36. Cross-correlation functions of the alongshore (solid line) and cross-shore (dash line) components of currents measured at the upper meters of moorings A and E for the upcoast flow regime.

component is of about 25 km. Higher values of 0.3-0.35 at a separation distance of 35-45 km are considered spurious at this point.

In the summer observation interval, the behavior of the cross-correlation coefficients of the alongshore currents is strikingly different with the cross-shore correlation of the alongshore flow much reduced. Figure II-36 illustrates this point by showing that the maximum correlation coefficient between the alongshore components at mooring A and E separated by 50 km reaches only 0.4 while in the winter interval it approached 0.8. The cross-shore speeds between these two sites in summer (Figure II-36) are hardly correlated with the very small cross-correlation coefficient of 0.12 (95% significance levels of 0 lag correlation coefficients of the alongshore and cross-shore components for the summer season are 0.33 and 0.26, respectively).

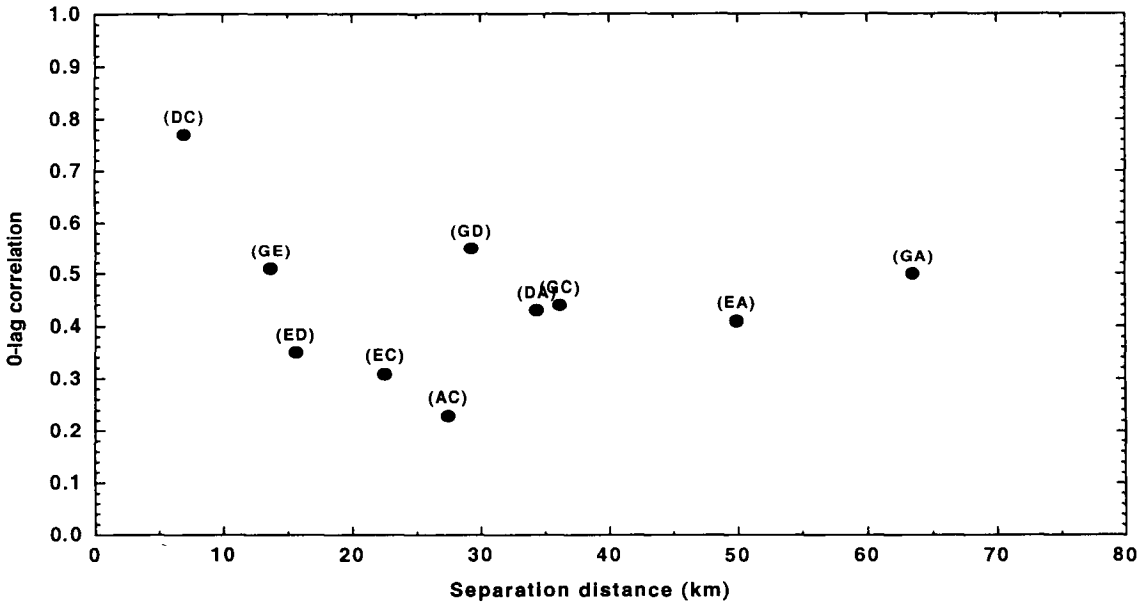

Figure II-37. Cross-correlation separation distance diagram of the alongshore current components for the upcoast flow regime (letters in brackets indicate mooring pairs).

The summer regime cross-correlation can also be summed up on a correlation-separation distance diagram as in Figure II-37. In contrast to an almost constant value of 0.8 overall separation distances seen during the downcoast regime (Figure II-34) the summer alongshore flow shows a steep decrease down to the correlation coefficient of about 0.3 with only a 20–30 km separation distance. Over the 30 km to 65 km separation distances the correlation coefficient jumps back to a fairly steady values of 0.4-0.5. Such behavior of the correlation coefficients suggests that they may be divided into two clusters. The first cluster of points (those with 0 to 30km separation distance) has the expected decay curve, but the second contains points (separation distance over 30km) that are statistically different from zero and may represent another process that we fail to understand at this point.

In Figure II-38 we present the correlation-separation distance diagram for the cross-shore summer regime flow for all mooring pairs. This figure with the large population of moorings points indicates a well-behaved trend for the upcoast regime cross-shore flow with a spatial length scale of about 35 km. It is difficult to contrast this summer spatial correlation with that of the winter regime (Figure II-35) due to the small number of the winter points (only six mooring pairs) but no significant difference is readily apparent except for the two high correlation points (~0.3) at 35 km and 45 km separation present in the winter but not in the summer.

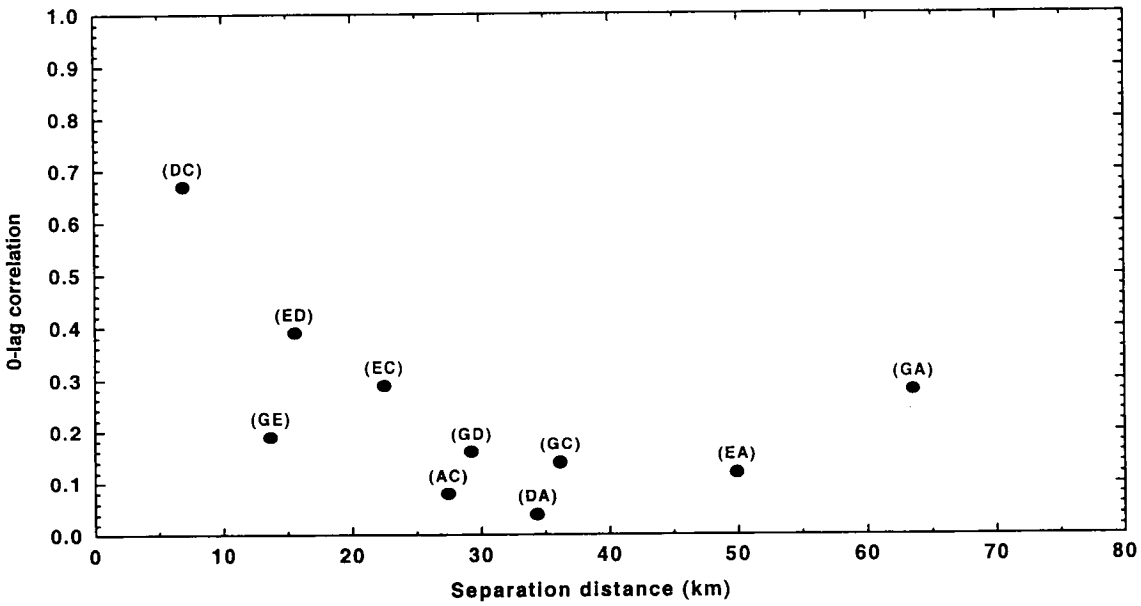

Figure II-38. Cross-correlation separation distance diagram of the cross-shore current components for the upcoast flow regime (letters in brackets indicate mooring pairs).

The question arises then why the spatial length scales of the alongshore flow for the upcoast (summer) and downcoast (winter) regimes are so distinctly different. One possible explanation is that the large spatial length scale of the downcoast regime flow could be the result of the coherence imposed on the surface layer by the larger scale energetic wind forcing of the winter regime as opposed to the less organized summer regime. These tendencies are also clearly evidenced in SCULP drifter tracks presented in Murray et al (1997).

5. Multiple Coherence Analysis from Current Meter Data

To seek further insight into dynamical relationships controlling the transport observed along the transect, we studied multiple and partial coherence (Bendat and Piersol, 1986) between the transport and four forcing functions: (a) alongshore wind stress; (b) cross-shore wind stress; (c) alongshore pressure gradient (a sea level slope); and (d) buoyancy forcing proxied by river discharge as in Münchow and Garvine (1993). Wind stress was computed from the Galveston Buoy 42035 for the upcoast flow regime

and from the anemometer at Fresh Water Bayou for the downcoast regime. The sea level slope was calculated from subsurface pressure gauges located at Oyster Bayou and Freeport for both seasons, and buoyancy forcing is represented by Atchafalaya River discharge.

Figures II-39 and II-40 show multiple and partial coherence over 0.05 to 0.5 cpd frequency band (2- to 20-day period band) between the transport and possible driving mechanisms. For the winter observation period (Figure II-39), 60 to 95% of the total transport fluctuations (shown by the multiple coherence curve) are explained by the four forcing variables considered. Looking at individual partial coherences, the alongshore wind stress clearly accounts for majority of variance of the transport through the cross-section. It explains at least about 50% of its variance throughout the 0.05 to 0.5 cpd frequency band. There is also an indication that the cross-shore wind stress might be considered as a significant forcing for the transport fluctuations with periods between 3 and 5 days. Partial coherence of the alongshore sea level slope and river discharge with the winter transport is rarely statistically significant, and, therefore, their importance as possible sources of subtidal winter transport fluctuations is extremely small, if any.

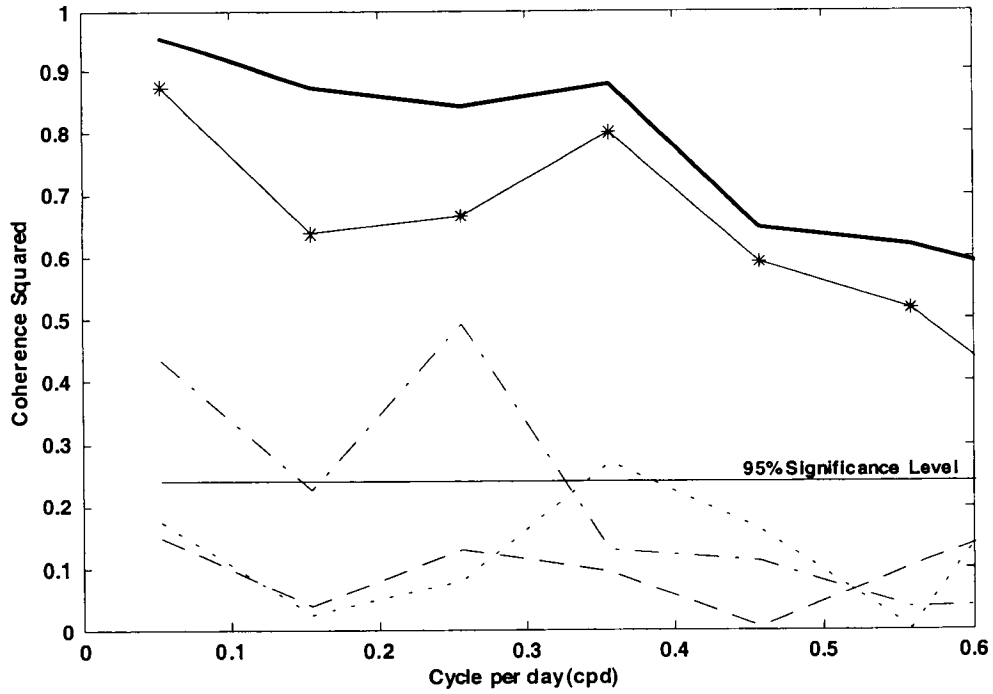

Figure II-39. Multiple (thick line) and partial coherence (symbol lines) between the transport observed during the downcoast flow regime and (a) alongshore wind stress (solid line with asterisks); (b) cross-shore wind stress (dash-dot line); (c) alongshore sea level slope (dashed line); (d) Atchafalaya River discharge (dotted line); the lower straight solid line is the 95% significance level.

In the summer flow regime, 45 to 90% of the transport fluctuations (Figure II-40) is accounted for by four possible driving forces over the entire frequency band examined. During this regime, the transport fluctuations are not only well coherent with the alongshore wind stress but also with the alongshore surface slope at various frequencies, except for a narrow band centered around 0.28 cpd where they both become statistically insignificant. In addition, the cross-shore wind stress might be considered as an important forcing particularly for the transport fluctuations with periods between 5 and 10 days but its importance is rather secondary in comparison to the alongshore wind stress and sea level slope. Partial coherence between the transport and buoyancy forcing represented by the Atchafalaya discharge only appears statistically significant for the frequencies lower than 0.18 cpd and the percentage of variance explained by this possible driving force reaches about 45% at 0.1 cpd.

Additionally, for the summer period the multiple and partial coherence analyses (not shown) were performed with the wind stress computed from the wind data collected by the anemometer at Fresh Water Bayou. The multiple coherence results are similar to those obtained when the wind stress is computed from the wind data form Galveston Buoy. However, the partial coherence results are quite different, particularly those for the

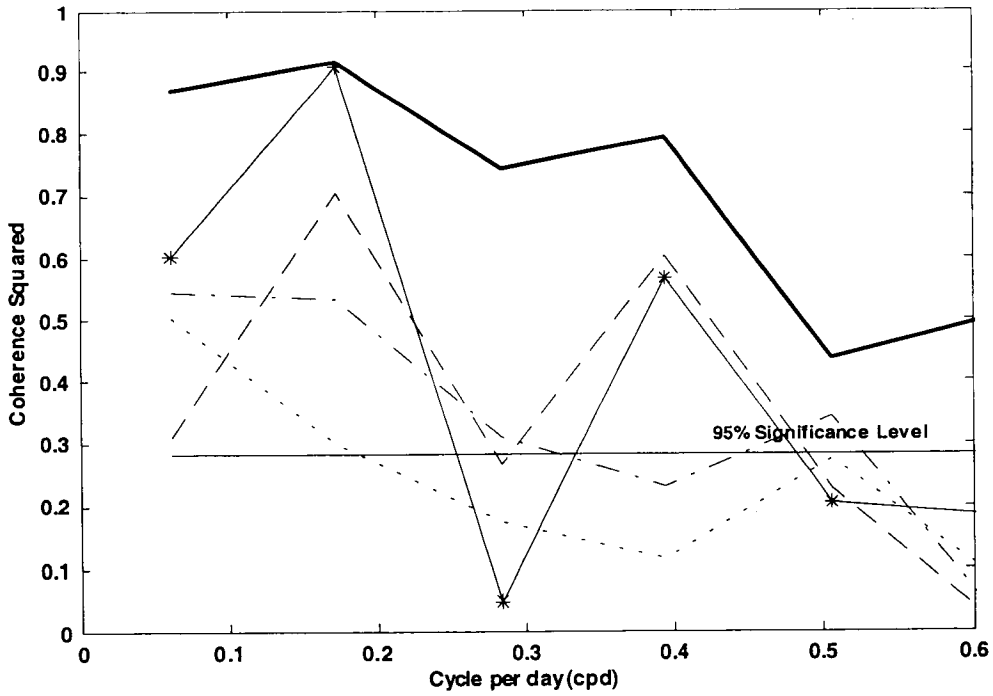

Figure II-40. Multiple (thick line) and partial coherence (symbol lines) between the transport observed during the upcoast flow regime and (a) alongshore wind stress (solid line with asterisks); (b) cross-shore wind stress (dash-dot line); (c) alongshore sea level slope (dashed line); (d) Atchafalaya River discharge (dotted line); the lower straight solid line is the 95% significance level.

sea level slope (smaller percentage of the transport variance is accounted for by this variable). At this point, we do not understand why these results are so different.

In summary, partial coherence analysis shows that the alongshore wind stress and sea level slope appear to be the dominant driving mechanisms of the upcoast flow regime transport fluctuations and these two variables explain alone most of the transport variance for the frequencies between 0.1 and 0.5 cpd except for the band centered at 0.28 cpd. In the downcoast flow regime, the alongshore wind stress, which alone explains at least 50% of the transport variance, seems to be a dominant forcing of the transport fluctuations in the frequency band between 0.1 and 0.5 cpd.

6. Transport and Wind Stress

Murray et al. (1997) showed that the alongshore momentum balance might be reduced to the simple linear relationship between the transport and alongshore wind stress assuming that other momentum balance terms are negligible. This relationship was described by the following equation:

$$\frac{T}{A} = \frac{1}{\rho \cdot r}\tau_{sx} \qquad (II-1)$$

where T is the transport, A is the cross-sectional area, ρ is the water density, r is the linear friction coefficient, and τ_{xs} is the average alongshore wind stress.

Our partial coherence analysis shows that the alongshore wind stress, especially in the downcoast flow regime, is a dominant driving force of the LTCC transport, therefore, (1) was applied to the data to learn whether there is a simple linear relationship between the observed transport and wind stress.

In Figure II-41 and II-42, the transport/area is plotted against the alongshore component of the wind stress for the winter and summer periods, respectively. The alongshore wind stress component was computed from the wind data measured at Freshwater Bayou using approach proposed by Large and Pond (1981).

For both flow regimes, the relation of the alongshore wind stress to transport is reasonably linear (correlation coefficient is 0.74 and 0.69 for the winter and summer periods, respectively), which supports the linear frictional balance expressed by (1). The summer and winter slopes of the best fit line indicates a linear friction coefficient of 0.05 cm/s that is in a range (0.1 to 0.01 cm/s) of that deduced from water level studies by Chuang and Wiseman (1983).

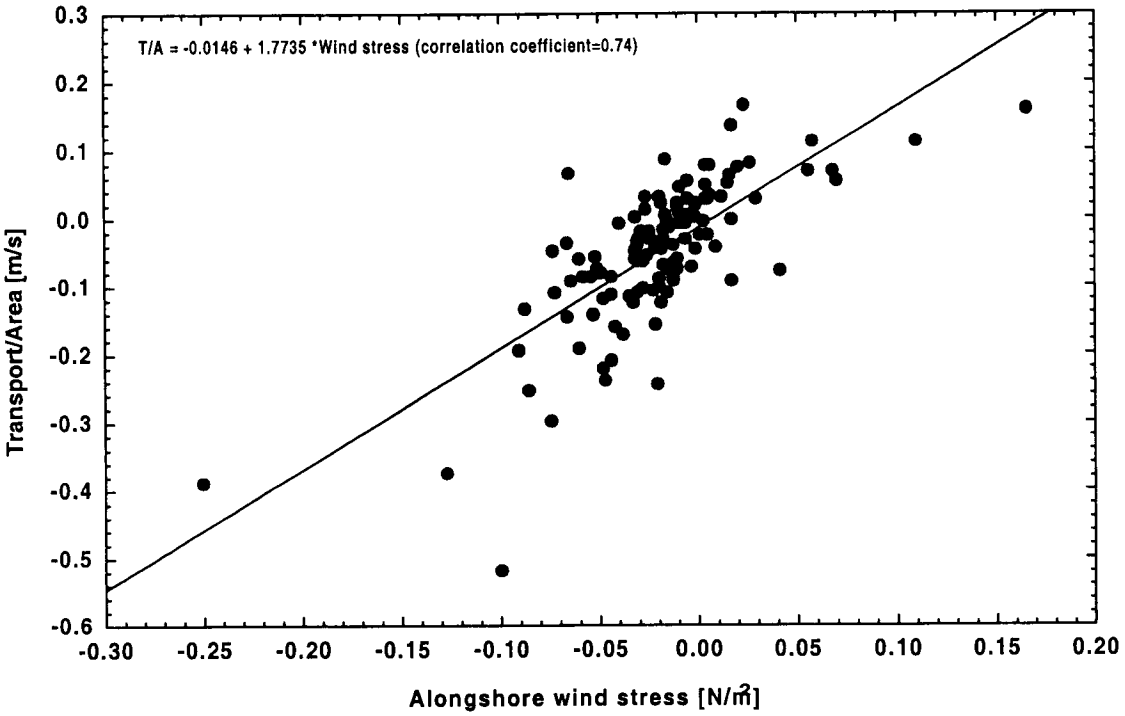

Figure II-41. The alongshore wind stress plotted against the transport (T) normalized by the cross-sectional area (A) for the downcoast flow regime.

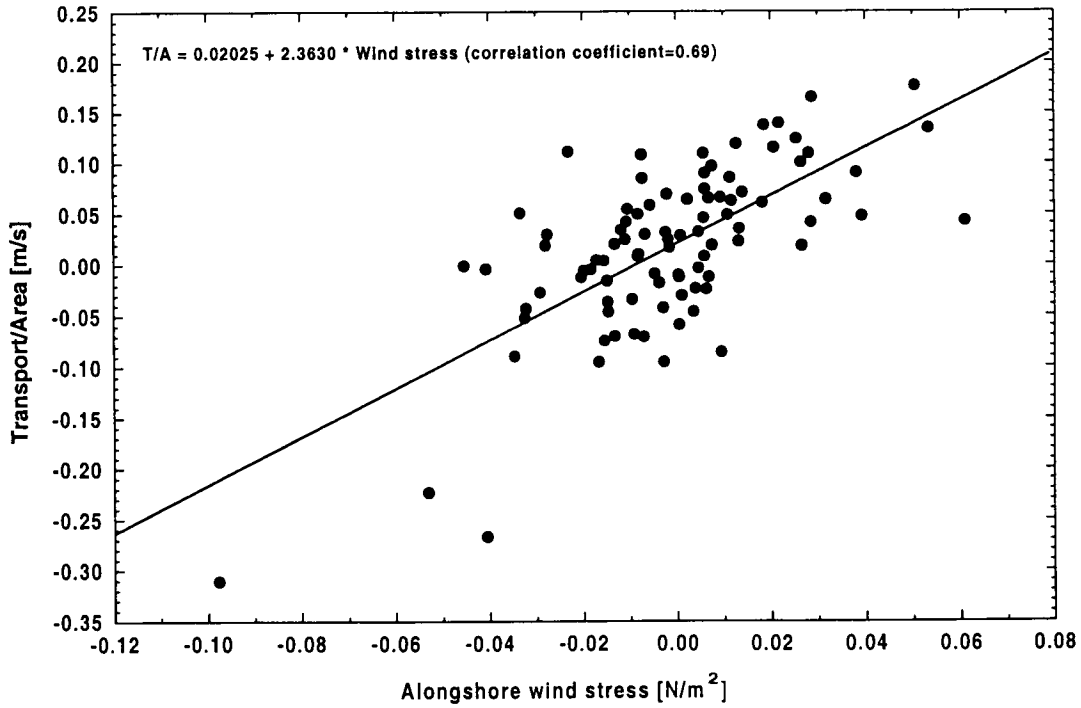

Figure II-42. The alongshore wind stress plotted against the transport (T) normalized by the cross-sectional area (A) for the upcoast flow regime.

A regression intercept value for the downcoast flow regime is negative and equal to 0.0146, which, although potentially related to other driving forces such as buoyancy or/and alongshore sea level slopes, is not significantly different from zero (p-value =0.05). This may be interpreted that other forces are relatively unimportant compared to the wind stress in the alongshore momentum balance for the winter period. The summer intercept (0.02025, p-value =0.001), however, can not be statistically considered as equal to zero. Therefore, the sectional transport observed during the upcoast flow regime may be driven not only by the alongshore component of the local wind but also by buoyancy or/and alongshore barotropic gradient.

7. A Wind-Driven Model

To continue in more detail examinations of the importance of the local wind stress as a major controlling forcing mechanism of the current variability within the LTCC, a wind-driven model, which was used to study variability of the currents within the Amazon River plume (Lentz, 1995), was employed. The model assumes that the input of energy from the wind into the surface layer plume is balanced by linearly approximated bottom friction and the temporal acceleration of the alongshore flow. This alongshore momentum balance is expressed as followed:

$$\frac{\partial u}{\partial t} + \frac{r \cdot u}{h} = \frac{\tau_{sx}}{\rho \cdot h} \qquad (II-2)$$

where u is the alongshore wind driven current, ρ is the reference water density, r is the linear friction coefficient, h is a plum thickness and τ_{xs} is the alongshore wind stress. Integrating (2) in time and solving for u yields

$$u(t) = \int_0^t \frac{\tau_{sx}}{\rho \cdot h} \exp(-r \cdot (t-t')/h)dt' + u(t=0) \cdot \exp(-r \cdot t/h). \qquad (II-3)$$

The alongshore wind stress component is computed from the wind data measured at Freshwater Bayou using approach proposed by Large and Pond (1981). The linear friction coefficient is chosen to yield the best agreement with the observations.

Taking the averaged plume thickness (h) equal to 12 m and density of 1021 kg/m^3, the alongshore current component was calculated from equation 3 for the downcoast flow regime period and then compared with the observed subsurface currents at three different mooring locations (B, C and F). Figure II-43 shows the model estimates and observations (40-hour low passed data) from a subsurface instrument at mooring F. Comparison of the wind-driven alongshore velocities based on (3) and observed 6.5m velocities at mooring F shows quite reasonable agreement. Maximum zero lag correlation between the observations and estimates based on equation II-3 with r=0.0003 m/s is 0.81 and it is significant at the 95% confidence level. Variability of the estimated wind-driven

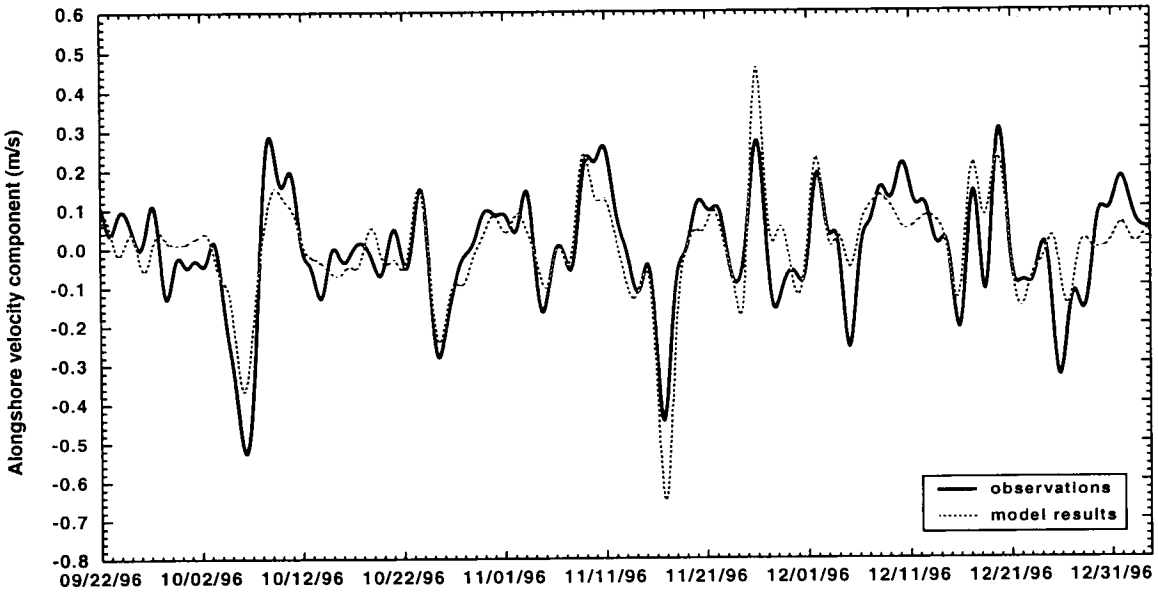

Figure II-43. The alongshore 6.5m current observed at mooring F during the downcoast flow regime compared to the prediction obtained from equation II-3.

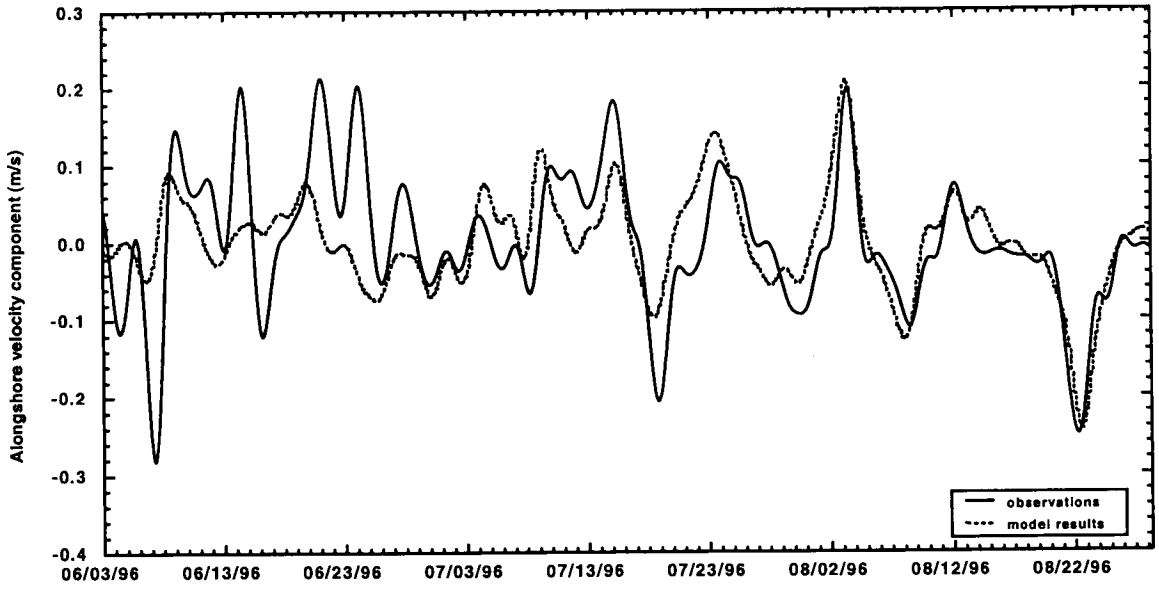

Figure II-44. The alongshore 5.5m current observed at mooring G during the upcoast flow regime compared to the prediction obtained from equation II-3.

alongshore current is very similar to that observed at F, for instance, events observed between October 3 and 11, 1996 or October 22 and November 4, 1996 or November 7 and 19, 1996. However, estimated amplitudes are either too large or small but differences between these amplitudes and those observed are never larger than 20 cm/s. Analogous conclusions are obtained for the other two moorings (mooring C: correlation coefficient=0.76 with r=0.0004 m/s; mooring B: correlation coefficient=0.76 with r=0.0003 m/s). These results reinforce an earlier conclusion that the alongshore wind stress, which explains alone at least 58% of the current variance, is a dominant driving force of the currents observed within the LTCC in the downcoast flow regime.

When the wind stress observed in the summer regime is applied to equation II-3 variability and amplitudes of the calculated wind-driven alongshore velocities are badly modeled for almost entire June but they are quite well reproduced for July and August 1996. The model estimates are again compared with subsurface current observations at three different locations (mooring A, C, and G). The best agreement is found at mooring G (Figure II-44). Maximum zero lag correlation between the observed alongshore velocities and estimates with r=0.00035 m/s, h=10 m, and density of 1010 kg/m^3 is 0.61 and it is significant at the 95% confidence level. It is obvious that major fluctuations in July and, particularly, in August such as events observed between August 1 and 6 or August 20 and 26 are wind driven. However, the June variability of the estimates is different from that of the observations with the amplitude differences reaching even 30 cm/s, which is quite large because of lower speeds usually measured within the LTCC in summer. Similar conclusions are found when the estimates are compared with the subsurface currents at mooring C and A (correlation coefficients with r=0.0002 m/s are 0.58 and 0.57, respectively). These results suggest that the alongshore wind stress, which explains alone 37% or less of current variance, is an important driving force of the coastal current, however, other driving mechanisms such as barotropic and baroclinic pressure gradients should be also considered not neglected as possible driving forces of the LTCC in the summer flow regime.

8. Salinity Characteristics

Results from the SeaCats intended to monitor the cross-shore and vertical salinity gradients were quite disappointing, such that only minimal useful analyses could be conducted. In Figure II-45 the sub-tidally filtered salinity data at outer mooring A and mid-section mooring D are showed. Outer mooring salinity is persistently higher and stable probably because the instrument was located in a small salinity gradient zone. Fluctuations at the interior mooring D are larger and more energetic which may suggest that this instrument was situated in waters with strong salinity gradient. Note also a large decrease of salinity to 15 psu between August 23 and 28 that probably resulted from an interplay of strong easterly winds and higher Atchafalaya River discharge observed at that time. Additionally, note the general increase of salinity at both locations from mid-June to late August as the freshwater content of the inner shelf decreases with decreased influx of Mississippi-Atchafalaya River water.

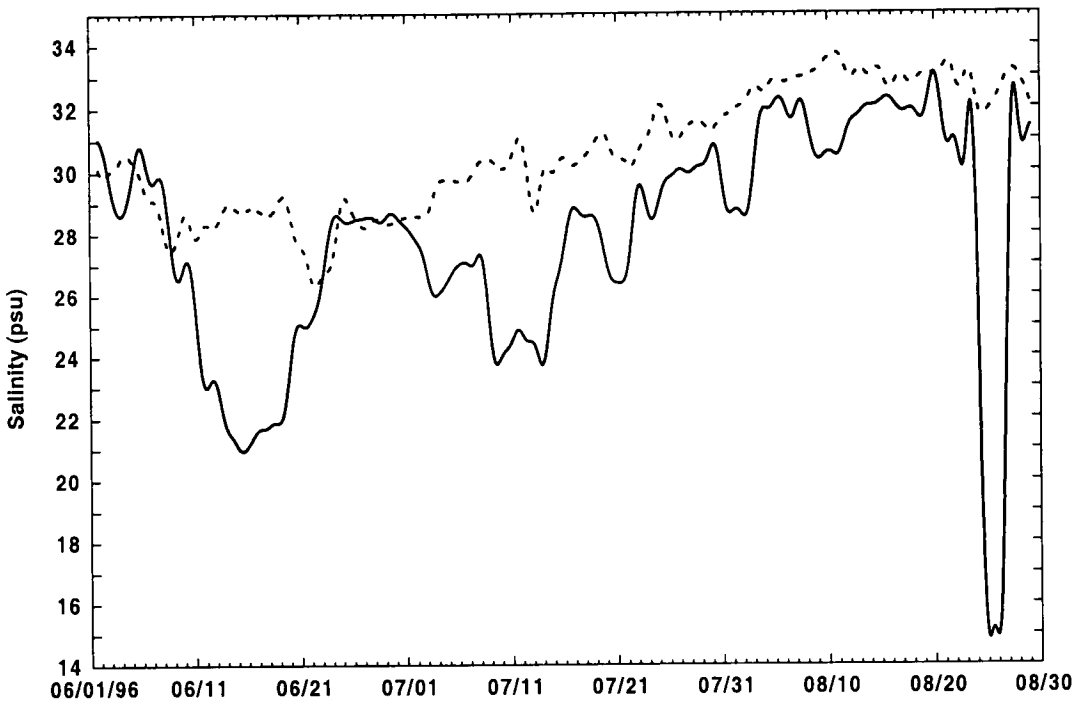

Figure II-45. A comparison of salinity from the outer edge (mooring A: dash line) and mid-region (mooring D: solid line) of the coastal current.

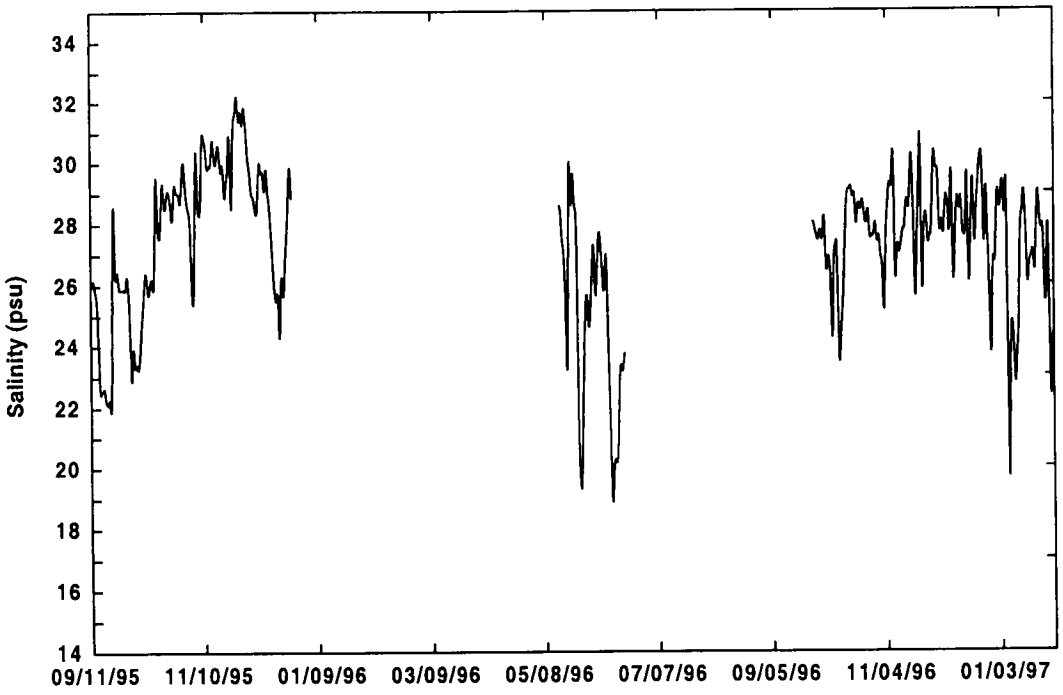

Figure II-46. A composite of the segments of salinity recorded from mooring F over a two-year period.

Figure II-46 shows the longest available salinity record of this project measured at mooring F. This plot displays again only sub-tidally filtered data. Time series of salinity, which varies between 18 and 32 psu, from this instrument suggests that mooring F was constantly in plume waters regardless of a month. Salinity there fluctuates quite rapidly in both summer and winter seasons. However, the short summer record suggests that these fluctuations are larger in summer (amplitudes of the order of 10 psu) than those measured in winter (amplitudes of the order of 5 psu). Additionally, average salinity seems to be smaller in summer than that observed in winter.

D. Conclusions

In order to determine the transport of the LTCC and its temporal and cross-shore variability a mooring line extending 80km offshore was deployed on the cross-shore transect near Cameron, LA. In addition to the current meter data, pressure, salinity, wind, and Atchafalaya River discharge were also analyzed to better understand the variability of the LTCC transport. Based on availability and quality of the data, two periods (one during the summer upcoast flow regime and one during the downcoast winter regime) were selected for further detailed studies.

Energy spectra of the near surface currents show expected semidiurnal and diurnal peaks associated with the tidal and inertial motions for both summer and winter flow regimes. Broad range of energetic motion is also observed in subtidal/weather frequency band (periods of 2-10 days) during the winter regime. Summer spectra of the near surface currents in the subtidal band may be described as 'red', i.e. the energy increases with decreasing frequencies. For both analyzed regimes, the energy in this frequency band is also clearly polarized in the alongshore direction. In winter, cross-spectra show high coherence of the currents through the water column that do suggest their barotropic response to the driving forcing. In summer, such high coherence of currents in vertical is not observed.

Transport computations show that in the winter season, the mean transport of LTCC is of – 60,774.2 m^3/s and 19,799 m^3/s in summer. In both seasons the transport is characterized by high synoptic scale variability (standard deviations are 131,445 m^3/s and 99,002 m^3/s for winter and summer seasons, respectively).

The data indicate that the decorrelation time scale of the alongshore current component in the downcoast flow regime show values of 40-80 hours. In the summer observation period, this decorrelation time is much larger and varies from 80 to about 290 hours. There is also some indication that in summer there is a sharp increase of the decorrelation time in the offshore direction. For both observation periods, the decorrelation times of the cross-shore component of the LTCC are shorter than those of the alongshore except for currents observed at mooring A. These times vary between 20 to 60 and 50 to 90 hours for the winter and summer regimes, respectively.

In the winter regime, regardless of the separation distance, crosscorrelation coefficients determined from meter pairs vary between 0.8 and 0.9 for the alongshore component; therefore, the spatial decorrelation length scale is much larger than offshore

extend of the mooring array (>50km). In summer, the crosscorrelation coefficients of the alongshore current component present a confusing picture. There appears to be two clusters of points: one resembling the behavior of the cross-shore component, and the other cluster showing a constant value about 0.5 for large separation distances. During the downcoast flow regime, the spatial decorrelation length scale of the cross-shore current component appears to be about 40km. In summer, this spatial length scale for the same current component is similar to that of the downcoast regime showing a value of 35-40km.

Multiple coherence analysis of the transport for the winter regime shows that 60 to 95% of its variability is explained by four inputs (alongshore pseudo wind stress, cross-shore pseudo wind stress, water level difference, and Atchafalaya River discharge). Partial coherence clearly shows that the alongshore wind stress is a dominant driving mechanisms. In the summer regime, four input variables account for 45 to 90% of variability of the transport. In this case, in addition to the alongshore wind stress, the alongshore sea level slope seems to be also important driving forcing.

Our data support the simple frictional balance model and show that a relation between the summer and winter transport fluctuations and the alongshore wind stress is reasonably linear. However, for the summer observation period, the fluctuations are not terminated when the wind stress is zero. Such behavior suggests that the remaining fluctuations are caused by other forcing mechanisms, for instance, barotropic and/or baroclinic pressure gradients.

Results from the model, which assumes that currents are wind driven, confirms that the alongshore wind stress is a dominant driving force of the LTCC in the downcoast flow regime. In the upcoast flow regime, this wind stress is also an important driving force; however, other forcing mechanisms such as barotropic and/or baroclinic pressure gradients should not be neglected either.

Finally, the limited data from the salinity sensors deployed on the current meter moorings suggest that the cross-shore array remained in the coastal plume throughout both the summer and winter observational intervals.

REFERENCES

Bloomfield, P., 1976. Fourier Analysis of Time Series. John Wiley and Sons, 258 pp.

Bendat, J.S., and A.G. Piersol, 1986. Random Data: Analysis and Measurement Procedures. Second edition, John Wiley and Sons, 566 pp.

Chao, S.Y., 1988. River-forced estuarine plumes. J. Phys. Oceanogr. 18, 72-88.

Chen, Ch., R.O. Reid, and W.R. Nowlin, Jr., 1996. Near inertial oscillations over the Texas-Louisiana shelf. J. Geophys. Res. 101(C2), 3509-3524.

Chuang, W.S., W.J. Wiseman, Jr., 1983. Coastal sea level response to frontal passages on the Louisiana-Texas shelf. J. Geophys. Res. 88(C4), 2615-2620.

Cochrane, J.D., and F.J. Kelly, 1986. Low-frequency circulation on the Texas-Louisiana shelf. J. Geophys. Res. 91(C9), 10,645-10,659.

Crout, R.L., W.J. Wiseman, Jr., and W.S. Chuang, 1984. Variability of wind driven currents, west Louisiana inner continental shelf: 1978-1979. Contrib. Mar. Sci. 27, 1-11.

Csanady, G.T., 1982. Circulation in the Coastal Ocean. D. Reidel Publishing Company, 279 pp.

Daddio, E., W.J. Wiseman, Jr., and S.P. Murray, 1978. Inertial currents over the inner shelf near 30N. J. Phys. Oceanogr. 8, 728-733.

DiMago, G.J., L.F. Bosart, and G.W. Endersen, 1976. An examination of the frequency and mean conditions surrounding frontal incursions into the Gulf of Mexico and Caribbean. Mon. Weather Rev. 104, 709-718.

DiMarco, S.F., R.O. Reid, 1998. Characterization of the principal tidal current constituents on the Texas-Louisiana shelf. J. Geophys. Res. 103(C2), 3093-3109.

Dinnel, S.P., and W.J. Wiseman, Jr., 1986. Fresh water on the Louisiana and Texas shelf. Cont. Shelf Res. 6, 765-784.

Dronkers, J.J., 1964. Tidal Computations in River and Coastal Waters. North-Holland Pub. Co.; New York, Interscience Publishers, 518 pp.

Godin, G., 1972. The Analysis of Tides. University of Toronto Press, 264 pp.

Gutierrez de Velasco, G., and C.D. Winant, 1996. Seasonal patterns of wind stress and wind stress curl over the Gulf of Mexico. J. Geophys. Res. 101(C8), 18,127-18,140.

Hsu, S.A., 1988. Coastal Meteorology. Academic Press, Inc., 260 pp.

Kundu, P.H., and J.S. Allen, 1976. Some three-dimensional characteristics of low-frequency current fluctuations near Oregon coast. J. Phys. Oceanogr. 6, 181-199.

Kundu, P.H., 1976a. A note on the Ekman veering observed near the ocean bottom. J. Phys. Oceanogr. 6, 238-242.

Kundu, P.H., 1976b. An analysis of inertial oscillations observed near Oregon coast. J. Phys. Oceanogr. 6, 879-893.

Large, W.G. and S. Pond. 1981. Open ocean momentum flux measurements in moderate and strong winds. J. Phys. Oceanogr.. 11, 324-336.

LATEX A program scientists and staff, 1997. Inertial and superinertial motion. In: Texas-Louisiana shelf circulation and transport processes study – draft synthesis report. OCS Study MMS 97-xx. U.S. Dept. of the Interior, Mineral Management Service, Gulf of Mexico OCS Region, New Orleans, LA.

Lentz, S. J., 1995. The Amazone River plume during AMASSEDS: Subtidal current variability and the importance of wind forcing. J. Geophys. Res., 100(C2), 2377-2390.

Li, Y., W.D. Nowlin, Jr., and R.O. Reid, 1997. Mean hydrographic fields and their interannual variability over the Texas-Louisiana continental shelf in spring, summer, and fall. J. Geophys. Res. 102(C1), 1027-1049.

Millot, C., and M. Crepon, 1981. Inertial oscillations on the continental shelf of the Gulf of Lions – observations and theory. J. Phys. Oceanogr. 11, 639-657.

Mooers, C.N.K., 1973. A technique for the cross spectrum analysis of pairs of complex-valued time series, with emphasis on properties of polarized components and rotational invariants. Deep-Sea Res. 20, 1129-1141.

Murray, S.P., E. Jarosz, and E.T. Weeks, 1997. Physical oceanographic observations of the coastal plume. In: Murray, S.P. (editor), Final report : an observational study of the Mississippi-Atchafalaya coastal plume. OCS Study MMS 97-xx. U.S. Dept. of the Interior, Mineral Management Service, Gulf of Mexico OCS Region, New Orleans, LA.

Murray, S.P. and M. Young. 1985. The nearshore current along a high-rainfall, trade-wind coast - Nicaragua. Estuar. Coast. Shelf Sci., vol.21, no.5, 687-699.

Münchow, A. and R.W. Garvine, 1993. Buoyancy and wind forcing of a coastal current. J. Mar. Res. 51, 293-322.

Pollard, R.T., and R.C. Millard, Jr., 1970. Comparison between observed and simulated wind-generated inertial oscillations. Deep-Sea Res. 17, 813-821.

Pugh, D.T., 1987. Tides, Surges and Mean Sea-Level. A Handbook for Engineers and Scientists. John Wiley and Sons, 472 pp.

Sciremammano, F., Jr., 1979. A suggestion for the presentation of correlations and their significance levels. J. Phys. Oceanogr. 9, 1273-1276.

Smith, N.P., 1975. Seasonal variations in nearshore circulation in the northwestern Gulf of Mexico. Cont. Mar. Sci. 19, 49-65.

Smith, N.P., 1978. Low-frequency reversals of nearshore currents in the northwestern Gulf of Mexico. Cont. Mar. Sci. 21, 103-115.

Smith, R.L., 1968. Upwelling. Oceanogr. Mar. Biol. Ann. Rev. 6, 11-46.

Vastano, A.C., C.N. Barron, Jr., and E.W. Shaar Jr., 1995. Satellite observations of the Texas current. Cont. Shelf Res. 15(6), 729-754.

Wiseman, W.J. Jr., and F.J. Kelly, 1994. Salinity variability within the Louisiana coastal current during the 1982 flood season. Estuaries, 17(4), 732-739.

Wiseman, W.J., Jr., N.N. Rabalais, R.E. Turner, S.P. Dinnel, and A. MacNaughton, 1997. Seasonal and interannual variability within the Louisiana coastal current: stratification and hypoxia. J. Mar. Sys., 12, 237-248.

Yoshida, K., 1967. Circulation in the eastern tropical oceans with special reference to upwelling and undercurre nts. Jap. J. Geophys., 4, 1-75.

The Department of the Interior Mission

As the Nation's principal conservation agency, the Department of the Interior has responsibility for most of our nationally owned public lands and natural resources. This includes fostering sound use of our land and water resources; protecting our fish, wildlife, and biological diversity; preserving the environmental and cultural values of our national parks and historical places; and providing for the enjoyment of life through outdoor recreation. The Department assesses our energy and mineral resources and works to ensure that their development is in the best interests of all our people by encouraging stewardship and citizen participation in their care. The Department also has a major responsibility for American Indian reservation communities and for people who live in island territories under U.S. administration.

The Minerals Management Service Mission

As a bureau of the Department of the Interior, the Minerals Management Service's (MMS) primary responsibilities are to manage the mineral resources located on the Nation's Outer Continental Shelf (OCS), collect revenue from the Federal OCS and onshore Federal and Indian lands, and distribute those revenues.

Moreover, in working to meet its responsibilities, the **Offshore Minerals Management Program** administers the OCS competitive leasing program and oversees the safe and environmentally sound exploration and production of our Nation's offshore natural gas, oil and other mineral resources. The MMS **Minerals Revenue Management** meets its responsibilities by ensuring the efficient, timely and accurate collection and disbursement of revenue from mineral leasing and production due to Indian tribes and allottees, States and the U.S. Treasury.

The MMS strives to fulfill its responsibilities through the general guiding principles of: (1) being responsive to the public's concerns and interests by maintaining a dialogue with all potentially affected parties and (2) carrying out its programs with an emphasis on working to enhance the quality of life for all Americans by lending MMS assistance and expertise to economic development and environmental protection.